MECHANISTIC STUDY OF AUTOPHAGY-TARGETING MODULATORS AS POTENT ANTIPROLIFERATION STRATEGY FOR ACUTE MYELOID LEUKAEMIA

WANG LEI

PhD

The Hong Kong Polytechnic University

2025

The Hong Kong Polytechnic University

Department of Applied Biology and Chemical Technology

Mechanistic Study of Autophagy-targeting Modulators as Potent Antiproliferation Strategy for Acute Myeloid Leukaemia

Wang Lei

A thesis submitted in partial fulfilment of the requirements for the degree of Doctor of Philosophy

April 2025

CERTIFICATE OF ORIGINALITY

I hereby declare that this thesis is my own work and that, to the best of my knowledge and belief, it reproduces no material previously published or written, nor material that has been accepted for the award of any other degree or diploma, except where due acknowledgement has been made in the text.

_____(Signed)

_____Wang Lei_____(Name of student)

Abstract

Acute myeloid leukemia (AML) is the most aggressive form of leukemia, with a five-year relative survival rate of only 31.9%. Despite significant advancements in therapeutics over the past two decades, the prognosis for AML patients remains poor. This is mainly due to high relapse rates and limited treatment options for older adults, who constitute the majority of AML cases and are often unable to tolerate intensive chemotherapy. Current first-line treatments primarily rely on traditional chemotherapy, administered either as monotherapy or in combination with autologous transplantation. However, both are associated with substantial toxicity and have stringent physiological requirements, which further restricts their applicability to elderly patients. Thus, there is a persistent and urgent need for novel, less toxic therapies to improve outcomes for AML patients.

In this study, we identified Beclin-1-targeting stapled peptides (Tat-SPs) as potent inducers of autophagy-related autotic cell death in AML cell lines. Tat-SPs exhibited robust antiproliferative activity against AML cells as single agents and exhibited synergistic effects when combined with standard chemotherapies such as Cytarabine or Venetoclax *in vitro*. Tat-SPs also triggered notable mitochondrial dysfunction, including loss of mitochondrial membrane potential, elevated reactive oxygen species (ROS) levels, suppression of basal and maximal oxidative phosphorylation (OXPHOS) and activation of the mitochondrial permeability transition pore (MPTP).

We carried out mechanistic studies to investigate the cell death processes induced in AML cells after treatment by Tat-SPs. Our results show that Tat-SPs only induced autosis, a form of autophagy-dependent cell death while other known programmed cell death processes such as apoptosis, ferroptosis, necroptosis, and pyroptosis were not involved. We also identified intracellular Ca^{2+} calcium as a key mediator of cell death induced by Tat-SPs. Supplementing Ca^{2+} to culture medium or co-treatment with calcium regulators alleviated Tat-SP-induced cytotoxicity.

Furthermore, we also investigated the impact of Tat-SPs on immune cells as autophagy is known to be involved in both innate and adaptive immunity. Our data showed that Tat-SPs may activate T cells by promoting IL2 production and facilitating the nuclear translocation of NFAT1. Tat-SP4 also enhanced phagocytosis in macrophage cells.

Lastly, we carried out animal studies to assess the anti-AML activity of Tat-SPs *in vivo*. In AML-bearing mice, lead Tat-SPs significantly reduced leukemia burden and improved overall survival. Our pharmacokinetic studies showed that the lead candidate Tat-SP4 was rapidly absorbed at systemic level and reached maximum serum concentration of ~3.9 μM 5 minutes after injection at 40 mg/kg dosage and with detectable levels of ~2 μM persisting at 2 hours post-administration.

Overall, our study highlights autophagy-targeting Tat-SPs as promising

therapeutic candidates for AML. By triggering autotic cell death in AML cells and modulating both innate and adaptive immune response, Tat-SPs may offer a novel strategy to target both AML and the tumor microenvironment.

Dual-acting strategy of Tat-SPs in combating AML: An abstract view

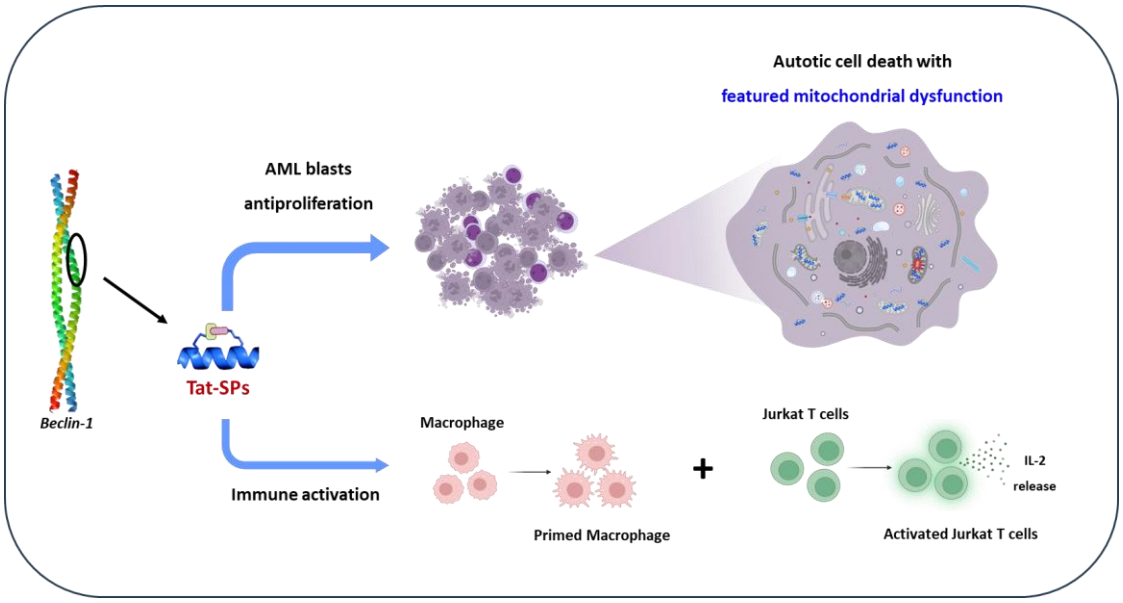

Acknowledgement

I would like to express my deepest gratitude to my supervisor, Prof. Yanxiang Zhao, for her invaluable guidance, mentorship, and unwavering support throughout this research project. Her expertise and encouragement have been crucial to the successful completion of this thesis.

I also extend my thanks to the team members, for their insightful discussions about our research results and engaging conversations during our journal club sessions, that greatly enriched this project. Special thanks to Dr. Li Na, for whose technical guidance and supporting works in animal experiments.

On a personal note, I am immensely grateful to my family and friends for their unconditional support during this challenging yet rewarding journey.

Finally, I would like to thank everyone who contributed to this thesis, whether directly or indirectly, for their kindness and assistance.

Contents

List of figures and tables

Figures

*Note: Figures 1.6, 4.14, 5.10, 5.11, 6.4 (A), 6.5 and Figure of "Dual-acting strategy of Tat-SPs in combating AML: An abstract view" were created using BioRender (BioRender.com).

Tables

Abbreviations

ACD	Autophagic cell death
ADCs	Antibody-drug conjugates
ADME	Absorption, distribution, metabolism, and elimination profile
ALL	Acute lymphoid leukemia
alloHSCT	autologous hematopoietic stem cell transplantation
AML	Acute myeloid leukemia
AMPK	AMP-activated protein kinase
ANT	Adenine nucleotide translocase
AP-1	Activator protein 1
APCs	Antigen-presenting cells
AraC	Cytarabine
ASMR	Age-standardized mortality rate
ASIR	Age-standardized incidence rate
ASXL1	ASXL transcriptional regulator 1
ATG3	Autophagy-related protein 3
ATG4C	Autophagy related 4C cysteine peptidase
ATG5	Autophagy-related protein 5
ATG6	Autophagy-related protein 6
ATG7	Autophagy-related protein 7
ATG12	Autophagy-related protein 12
ATG13	Autophagy-related protein 13
Atg14L	Autophagy-related protein 14-like
ATG16L1	Autophagy-related protein 16 like 1
ATG101	Autophagy-related protein 101
AUC	Average area under the concentration-time curve
AUCINF_obs	The observed AUC extended to infinity
α-KG	α-ketoglutarate
BAK	Bcl-2 antagonist
BAX	Bcl-2 associated X protein
BCL-2	B-cell leukemia/lymphoma-2
BFA	Bafilomycin A1
BH3	Bcl-2 homology domain 3PTEN
BIM	Bcl-2 interacting mediator of cell death
B-NDG	NOD-SCID with Il2rg gene deletion

CAR	Chimeric antigen receptor
CBFB	Core-binding factor subunit beta
CCD	Coiled-coil domain
CEBPA	CCAAT enhancer binding protein alpha
CLL	Chronic lymphoid leukemia
CML	Chronic myeloid leukemia
Cmax	Maximum plasma concentration
CPPs	Cell-penetrating peptides
CQ	Chloroquine
CRT	Calreticulin
CTLs	Cytotoxic T lymphocytes
Cyc-D	Cyclophilin-D
DAMPs	Damage-associated molecular patterns
DCs	Dendritic cells
DNMT3A	DNA methyltransferase 3 alpha
DRAM1	DNA damage regulated autophagy modulator 1
EGFR	Epidermal growth factor receptor
ER	Endoplasmic reticulum
ETC	Electron transport chain
FAB	French-American-British clasiffiation
FGFR-1	Fibroblast growth factor receptor 1
FIP200	FAK family kinase-interacting protein of 200 kDa
FKBP12	FK506-binding protein 12
FLT3	Fms related receptor tyrosine kinase 3
Gal-9	Galectin-9
GAPR-1	Golgi-associated plant pathogenesis-related protein 1
GASDMs	Gasdermin proteins
GO	Gemtuzumab ozogamicin
HCQ	Hydroxychloroquine
Hh	Hedgehog
HiDAC	High-dose Cytarabine
HK2	Hexokinase 2
HMAs	Hypomethylating agents
HMGB1	High mobility group box 1 protein
HOPS	Homotypic fusion and protein sorting
HSCs	Hematopoietic stem cells
IARC	International agency for research on cancer
IC50	Half maximal inhibitory concentration

ICD	Immunogenic cell death
IDH	Isocitrate Dehydrogenase
IL-2	Interleukin-2
IL-4	Interleukin-4
IMM	Inner mitochondrial membrane
IP3Rs	Inositol 1,4,5-trisphosphate receptors
ITD	Internal tandem duplication
JAK	Janus kinase
KRAS	Kirsten rat sarcoma virus
LAP	LC3-associated phagocytosis
LC3	Microtubule-associated protein 1 Light Chain 3
LPS	Lipopolysaccharide
MAMs	Mitochondria-associated membranes
Mcl-1	Myeloid leukemia 1
MCU	Mitochondrial calcium uniporter
MDM2	Murine double minute 2
MEF2	Myocyte enhancer factor 2
MHC	Major histocompatibility complex
mHtt	mutated Huntingtin
MOMP	Mitochondrial outer membrane permeabilization
MPTP	Mitochondrial permeability transition pore
mTOR	Mammalian target of rapamycin
MYH11	Myosin heavy chain 11
NAFLD	Non-alcoholic fatty liver disease
NCA	Noncompartmental analysis
NCX	Na^{+}/Ca^{2+} exchanger
NFAT1	Nuclear factor of activated T-cells cytoplasmic 2
NHL	Non-Hodgkin lymphoma
NKG2DL	Natural killer group 2D receptor ligand
NOD-SCID	Non-obese diabetic severe combined immunodeficiency
NPM1	Nucleophosmin 1
NRBF2	Nuclear receptor binding factor 2
OCR	Oxygen consumption rates
OMM	Outer mitochondrial membrane
OXPHOS	Oxidative phosphorylation
PARP	Poly (ADP-ribose) polymerase
PBMCs	Peripheral blood mononuclear cells
PCD	Programmed cell death

PDA	Pancreatic ductal adenocarcinoma
PD-1	Programmed cell death protein 1
PD-L1	Programmed death-ligand 1
PE	Phosphatidylethanolamine
PI3KC3	Class III phosphatidylinositol 3-kinase complex
PI3P	Phosphatidylinositol 3-phosphate
PKC	Protein kinase C
PKM2	Pyruvate kinase M2
PMA	Phorbol 12-myristate 13-acetate
PML	Promyelocytic leukemia
PPIs	Protein-protein interactions
PS	Phosphatidylserine
PTEN	Phosphatase and tensin homolog
p62/SQSTM1	Sequestosome-1
Rab7	Ras-related protein Rab-7
RARA	Retinoic acid receptor alpha
RIP1	Receptor-interacting serine/threonine-protein kinase 1
RIP3	Receptor-interacting serine/threonine-protein kinase 3
ROS	Reactive oxygen species
RUNX1	RUNX family transcription factor 1
RUNX1T1	RUNX1 partner transcriptional co-repressor 1
SEER	Surveillance, epidemiology, and end results program
SERCAs	Sarcoplasmic/endoplasmic reticulum calcium ATPase
SESN1	Sestrin 1
SESN2	Sestrin 2
SMO	Sonic Hedgehog receptor Smoothened
SNARE	Soluble N ethylmaleimide sensitive factor attachment
TCA	Tricarboxylic acid cycle
TCR	T cell receptor
TET2	Tet methylcytosine dioxygenase 2
TFEB	Transcription factor EB
TKD	Tyrosine kinase domain
TLR4	Toll-like receptor 4
Tmax	Time to reach maximum plasma concentration
TMRM	Tetramethylrhodamine methylester
TP53	Tumor Protein P53
$T_{1/2}$	Time required for the plasma concentration to decrease by half
ULK1	Unc-51 like autophagy activating kinase 1

UVRAG	UV radiation resistance-associated gene protein
VDAC	Voltage-dependent anion channel
VPS15	Vacuolar protein sorting 15
VPS34	Vacuolar Protein Sorting 34
Vz	Observed volume of distribution
WT1	Wilms tumor protein
3-MA	3-methyladenine

Chapter 1 Introduction

1.1 Acute myeloid leukemia: The most challenging leukemia

1.1.1 Clinical significances of AML

Hematologic malignancies are broadly classified as leukemia, lymphoma, or myeloma, based on their cellular lineage and anatomical origin. These diseases disrupt the normal hematological system, as malignant cells lack the functional characteristics of healthy blood cells. Malignant cells aggressively occupy nutritional resources and enter different tissues and organs through blood circulation, causing organ failure and functional diseases.

Leukemia occurs when myeloid or lymphoid progenitor cells undergo unexpected differentiation failure in the bone marrow, that these cells can no longer evolve into functional blood cells like myeloblast cells or lymphocytes, but display aggressive proliferating ability. Lymphoma arises when pathological disruptions affect natural killer cells, T cells, or B cells, blocking their normal lymphocyte functions. Myeloma, or multiple myeloma, is a cancer type that raised from plasma cells, that abnormal plasma cells proliferate uncontrollably and can produce damaging antibodies when facilitate with disruptive oncogenic drivers. The overview of these major cancer types can be seen in Figure 1.1. (Rad & Häggström, 2009).

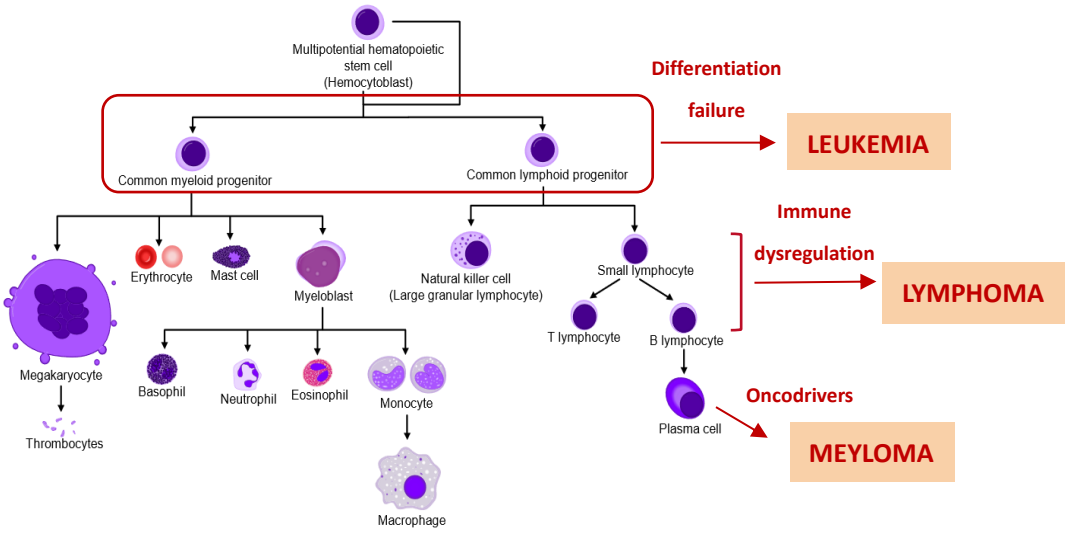

Figure 1.1 Occurrence site of major hematological cancers (Rad & Häggström, 2009, download from Wikipedia).

By 2022, global age-standardized incidence rates for hematological malignancies indicated that non-Hodgkin lymphoma had the highest incidence, followed closely by leukemia, with lower rates observed for multiple myeloma and Hodgkin lymphoma. Despite a similar incidence to non-Hodgkin lymphoma, leukemia demonstrated the highest age-standardized mortality rate among hematological cancers. As the most aggressive hematological malignancy, leukemia ranked thirteenth in global cancer incidence and tenth in cancer-related mortality, with 487,294 new cases and 305,405 deaths reported worldwide in 2022 according to IARC.

Based on the progression stage and the specific type of neoplastic cells involved, leukemia can be further classified into four main subtypes: acute myeloid leukemia (AML), acute lymphoid leukemia (ALL), chronic myeloid leukemia (CML), and

chronic lymphoid leukemia (CLL). According to case statistics from the United States as of 2020, most patients with leukemia carcinoma achieve a favorable prognosis with over 70% of the 5-year relative survival rate found in ALL, CML, and CLL. However, less than 32% of AML patients can reach this milestone, as shown in Figure 1.2 (National Cancer Institute, 2022). Despite the advancements in leukemia cancer treatment, the therapeutic outcomes for AML remain disappointing.

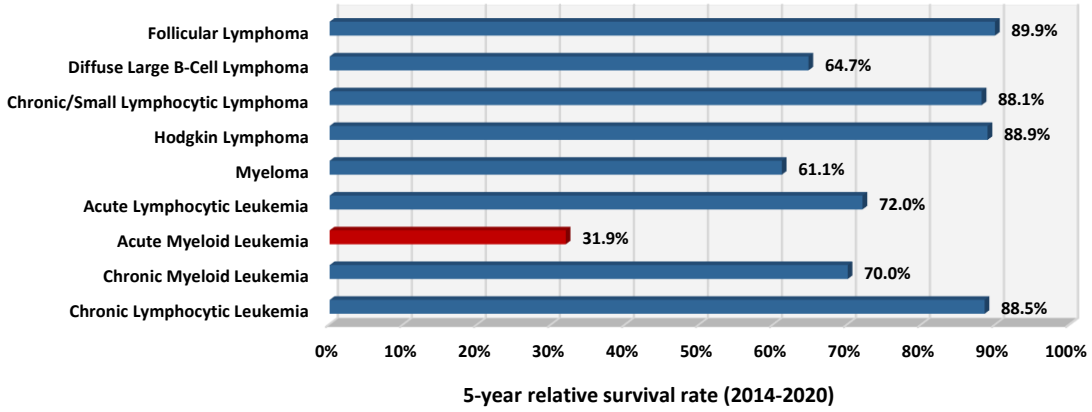

Figure 1.2 5-year relative survival rate of leukemia (SEER, 2024).

As the subtype with the lowest 5-year relative survival rate among all leukemia subtypes, AML is characterized by aggressive proliferation and rapid dissemination of malignant myeloid cells. The disease progresses quickly, with AML cells overcrowding normal myeloid cells in the bone marrow and spreading into the bloodstream. The displacement of normal blood-forming cells results in a severe deficiency of functional white blood cells, red blood cells, and platelets. Consequently, AML patients experience symptoms such as fatigue, weakness, shortness of breath, fever, frequent infections, severe anemia, and excessive bleeding. In worse cases, AML cells may infiltrate the

central nervous system, including the brain and spinal cord, leading to more severe disruptions such as paralysis.

According to the data from SEER 2022, older adults are especially vulnerable to AML, with a median age of diagnosis at 69. And the majority of cases occur in individuals aged 65 to 74. Although modest survival benefits had been achieved over the past decade, that the 5-year relative survival rate increasing from 29.5% for the 2011-2017 period to 31.9% for 2014-2020, only about one-third of patients survive beyond five years after an AML diagnosis. The poor survival outcomes are primarily due to high relapse rates, even in patients who initially achieve remission, limited treatment options for older adults who cannot tolerate intensive chemotherapy, and a lack of novel therapies (Bispo et al., 2020). Current first-line treatments still rely on traditional chemotherapy drugs, either alone or combined with autologous transplantation, both of which are often associated with toxic side effects or demanding physiological requirements.

1.1.2 Genetic drivers for AML

Clinical diagnosis of AML typically is based on the cellular assessment of bone marrow, such as the immunotyping and cytogenetic analysis. AML cells display cancerous morphology differed from normal cells. Normal marrow contains cells at various developmental stages and with distinct cell types. While, AML cells demonstrating arrested status at an early stage of development, exhibit a uniform

appearance, as illustrated in Figure 1.3 (LLS, 2023). The French-American-British (FAB) classification of AML is one of the standard systems used in AML diagnosis established since 1976 (Wakui et al, 2008). It is a system that based on cell morphology and phenotypes to divide AML from M0 to M7, and until today, this classification helps for AML patients who carrying no significant pathological mutations.

A B

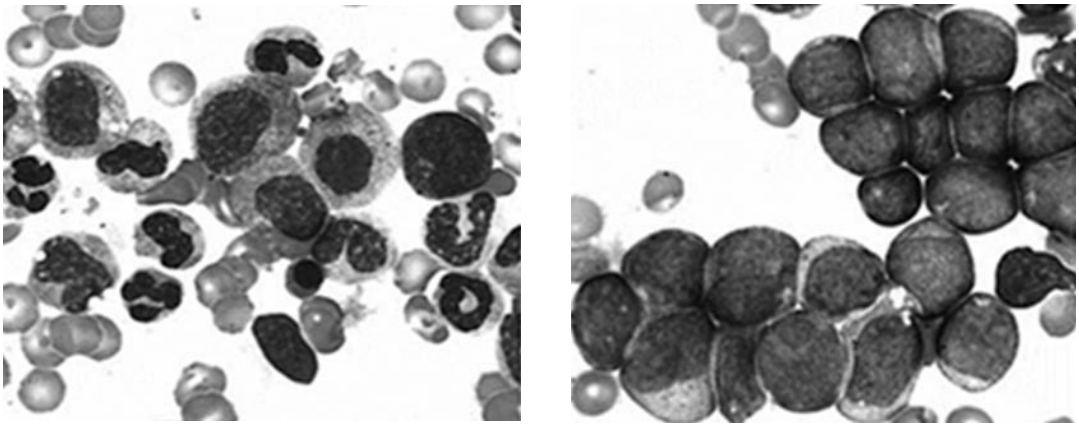

Figure 1.3 Morphology of marrow cells under microscope (LLS, 2023). (A) Normal heathy marrow cells; (B) AML blast cells.

However, advances in technology have enabled comprehensive characterization of the genetic landscape in AML, revealing that over 97% of patients harbor genetic alterations. (Papaemmanuil et al., 2016). This has allowed specialists to effectively utilize genetic mutations for accurate pathological classification and improved treatment strategies in AML.

The diagnostic guidelines from the World Health Organization (WHO) and the

International Consensus Classification (ICC) focus on mutation-based AML phenotyping. They highlight several disease-driving mutations, such as *RUNX1::RUNX1T1*, *CBFB::MYH11*, and *PML::RARA* fusions. The complete list can be found in Table 1.1(Khoury et al, 2022). However, not all frequent mutations are included in these guidelines, such as the cooperative mutations like *FLT3, DNMT3A*, and *IDH*, which occur in 10%–30% of AML patients.

Table 1.1 Major classification of Acute Myeloid Leukemia by WHO, 2022

Cytogenetic alterations /Mutations of AML	*RUNX1::RUNX1T1 fusion*
	CBFB::MYH11 fusion
	RBM15::MRTFA fusion
	NUP98 rearrangement
	PML::RARA fusion (Acute promyelocytic leukemia)
	CEBPA mutation
	KMT2A/MLL rearrangement
	DEK::NUP214 fusion
	MECOM rearrangement
	*BCR::ABL1 fusion**
	NPM1 mutation
Note: * 20% blasts cells requested	

NPM1 mutations are among the most common genetic alterations in adult AML, present in 30%–35% of cases (Ranieri et al., 2022). Classified as a driver mutation by the WHO guidelines, *NPM1* encodes nucleophosmin 1, a protein that shuttles between the nucleus and cytoplasm. Nucleophosmin 1 normally localized in the nucleus and regulates ribosome biogenesis and transport. Mutated *NPM1* contributes to leukemogenesis by disrupting homeobox genes, arresting AML cells in an immature state, and inducing cytoplasmic dislocation of the protein. It also plays a role in AML recurrence and relapse ((Falini et al., 2020; Ranieri et al., 2022). Although targeted therapies for *NPM1* mutations are under development, none have received FDA approval to date.

FLT3 mutations, demonstrated in approximately one-third of AML patients, encode FMS-like tyrosine kinase 3. Although not included in the foundational WHO classifications, *FLT3* mutations are considered in the risk stratification guidelines of the European LeukemiaNet (ELN). The most common alteration is an internal tandem duplication (*FLT3-ITD*), while other types such as point mutations like tyrosine kinase domain (TKD), rearrangements, deletions, and amplifications also occur. These mutations result in continuous activation of the tyrosine kinase, promoting anti-apoptotic effects in malignant AML cells (Daver et al., 2019; Kayser & Levis, 2023). Despite the commercial availability of FLT3 inhibitors, drug resistance remains therapeutic issues of poor prognosis and limited efficacy in relapsed cases.

DNMT3A mutations, present in around 20% of AML patients, affect the gene encoding DNA methyltransferase 3A, a crucial enzyme for DNA methylation (Shah & Licht, 2011; Lauber et al., 2020). High levels of DNMT3A are found in embryonic stem cells, and its deletion disrupts cell self-renewal and differentiation. While *DNMT3A* mutations alone can impair DNA methylation, they worsen AML prognosis when combined with other common mutations like *FLT3* and *NPM1* (Lauber et al., 2020).

IDH genes encode isocitrate dehydrogenase enzymes, with occurrence in approximately 20% of AML patients (Issa & Dinardo, 2021). Mutations in *IDH1* and *IDH2* are most common, with *IDH2* mutations slightly more frequent (12%) than *IDH1* mutations (8%). These mutations produce the oncometabolite 2-hydroxyglutarate (2-HG), which inhibits normal myeloid differentiation and promotes leukemogenesis. FDA-approved IDH inhibitors were available since 2017, and combined therapies involving IDH inhibitors and chemotherapy are under investigation for better outcomes (Issa & Dinardo, 2021; Dinardo et al., 2015).

RUNX1 mutations, present in about 10% of AML patients, is the gene of Runt-related transcription factor 1, an essential protein for hematopoiesis (Mill et al., 2022). These mutations lead to enhanced sensitivity to ribosomal stress and impaired protein translation, resulting in poor prognosis. About 30% of *RUNX1*-mutated cases involve germline mutations, with 44% of carriers developing myelodysplastic syndromes later in life (Simon et al., 2020).

CEBPA mutations, found in 10% of AML cases, define the CCAAT enhancer-binding protein α. These mutations can be monoallelic (*CEBPA*^{sm}) or biallelic (*CEBPA*^{bm}) (Fasan et al., 2014; Konstandin et al., 2018). Frameshift mutations in the N-terminal or bZIP domain of the C-terminus are common, with the latter one being more strongly associated with clinical prognosis (Taube et al., 2022).

TP53 mutations, although not included in the WHO framework, are part of the ICC guidelines for AML phenotyping. Present in around 10% of AML cases, these mutations disrupt the tumor-suppressor protein p53, which regulates the cell cycle and chromosomal stability (Grob et al., 2022; Yu et al, 2020). Mutated p53 promotes genomic instability and leukemogenesis and is associated with poor therapeutic outcomes.

Other cytogenetic aberrations, such as *TET2*, *ASXL1*, *N/KRAS*, and *WT1*, also contribute to AML pathogenesis. Co-mutations and interactions between multiple genetic alterations are common, underscoring the complexity and heterogeneity of AML, which complicates effective treatment strategies.

1.1.3 Therapeutic strategy for AML

Classical therapeutic strategies for acute myeloid leukemia comprise three phases: induction, consolidation, and post-remission follow-up. Since the introduction of the "7+3" regimen in 1973, which combines continuous infusion of Cytarabine for seven

days (100 mg/m²) with daunorubicin administered intravenously for three days (45 mg/m²) (Rowe, 2022), complete remission has been achieved in a subset of patients. Subsequent modifications, including the use of alternative anthracyclines such as idarubicin and dose adjustments, have aimed to reduce toxicity and improve outcomes. Nevertheless, the 7+3 regimen remains the standard induction therapy for most AML patients, with the primary goal of eradicating malignant myeloid cells. The consolidation phase, typically employing high-dose Cytarabine (HiDAC), targets residual leukemic cells, with treatment tailored to individual patient characteristics. For eligible patients, allogeneic or autologous hematopoietic stem cell transplantation (alloHSCT) is considered. Advances in transplantation and supportive care have reduced non-relapse mortality and improved survival in selected patients (Bakhtiar et al., 2019; Ochs et al., 2022).

In the past decade, advances in cytogenetics, immunophenotyping, and the identification of actionable molecular targets have facilitated the development of targeted therapies, offering more effective and less toxic alternatives to conventional treatments. As of 2024, 18 drugs have received FDA approval for AML, with 11 approved since 2017, reflecting significant progress in the field, as presented in Figure 1.4 (Ochs et al., 2022). Notably, novel agents include FLT3 inhibitors, IDH inhibitors, BCL-2 inhibitors, and a CD33-targeted antibody-drug conjugate.

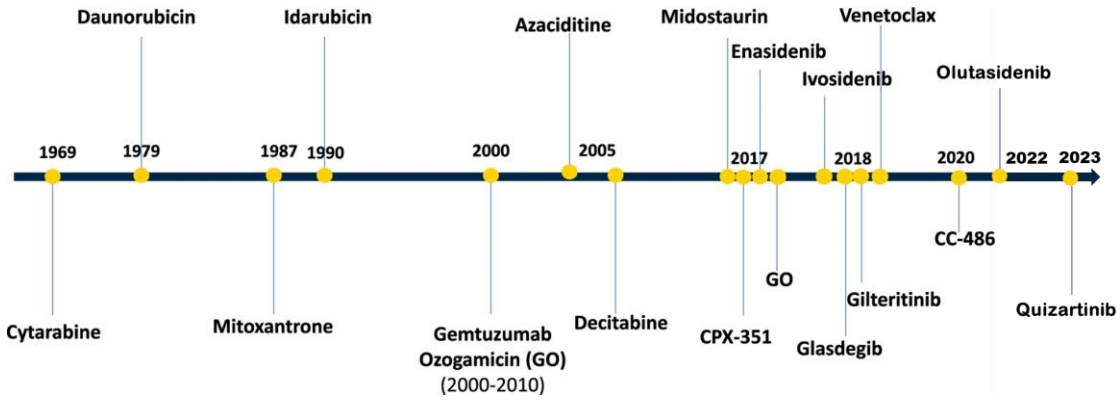

Figure 1.4 History of FDA approvals for AML (Ochs et al., 2022).

- **FLT3 inhibitors**

The introduction of FLT3 inhibitors has significantly advanced the treatment landscape for FLT3-mutated AML. Midostaurin was approved in 2017 for newly diagnosed patients with FLT3 mutations in combination with chemotherapy, followed by Gilteritinib in 2018 for relapsed or refractory cases, and Quizartinib in 2023 as maintenance monotherapy for newly diagnosed patients with *FLT3-ITD* mutations. FLT3 inhibitors are categorized into two types: type 1 inhibitors, such as Midostaurin and Gilteritinib, which bind to both the active and inactive conformations of FLT3 and are effective against both *FLT3-ITD* and *FLT3-TKD* mutations; and type 2 inhibitors, such as Quizartinib, which specifically bind to the inactive conformation and are selective for *FLT3-ITD* mutations. Despite these therapeutic advances, resistance to FLT3 inhibitors remains a significant clinical challenge. Resistance mechanisms include intrinsic genetic variability, secondary mutations in the ATP-binding site, and activation of alternative signaling pathways such as RAS. To address these challenges, combination strategies are being explored, including the use of histone deacetylase

inhibitors and agents targeting downstream pathways such as Pim kinases, mTOR, or Akt (Daver et al., 2019; Antar et al., 2020).

- **IDH inhibitors**

Three IDH inhibitors have been approved by the FDA: Ivosidenib and Olutasidenib, which target IDH1 mutations, and Enasidenib, which targets IDH2 mutations, all indicated for relapsed or refractory AML. Although these agents have improved survival in patients with IDH-mutated AML, resistance remains a significant challenge, particularly in cases with co-occurring mutations such as those affecting the RAS pathway, which are associated with poor therapeutic response (Mcmurry et al., 2021; Issa & Dinardo, 2021). Ongoing clinical trials are evaluating combination therapies, including regimens that incorporate FLT3 inhibitors or the BCL2 inhibitor Venetoclax, to enhance treatment efficacy in this genetically heterogeneous disease (Issa & Dinardo, 2021; Fruchtman et al., 2024).

- **BCL2 inhibitor**

The BCL2 family regulates apoptosis by balancing pro- and anti-apoptotic proteins at the mitochondrial outer membrane, with BH3-only proteins triggering cell death through mitochondrial permeabilization and caspase activation (Nwosu et al., 2024). In AML, overexpression of anti-apoptotic BCL2 sequesters BH3-only proteins, thereby blocking apoptosis. BH3-mimetic drugs, such as Venetoclax, disrupt this interaction by binding to BCL2 with high affinity, releasing pro-apoptotic proteins and

restoring apoptosis (Konopleva et al., 2016). Venetoclax, approved by the FDA in 2018 for use in combination with hypomethylating agents, has since been evaluated in various combination regimens, including with FLT3 inhibitors and chemotherapy, to improve survival outcomes. However, resistance to Venetoclax remains a significant challenge, driven by compensatory upregulation of Mcl-1, activation of alternative metabolic pathways, and mutations in Bax, highlighting the need for further research to overcome these limitations (Nwosu et al., 2024; Konopleva & Letai, 2018).

- **CD33 targeting therapy**

CD33, a hematopoietic surface antigen expressed in approximately 85–90% of both adult and pediatric AML cases, is associated with poor prognosis and serves as a strategic target for antibody-drug conjugate (ADC) therapy (Molica et al., 2021; Liu et al., 2022). Gemtuzumab ozogamicin (GO), a monoclonal anti-CD33 ADC, was initially approved by the FDA in 2000, withdrawn in 2010 due to hepatotoxicity concerns, and subsequently re-approved in 2017. GO is currently indicated in combination with Cytarabine and daunorubicin for newly diagnosed CD33-positive AML in adults, and as intermittent therapy for relapsed or refractory CD33-positive AML in both adults and pediatric patients. Its mechanism involves targeted delivery of the cytotoxic agent calicheamicin, which, upon internalization via CD33 binding, induces double-strand DNA breaks and cell death (Molica et al., 2021). However, the clinical efficacy of GO is limited by interpatient variability in CD33 expression, resistance mechanisms such as single nucleotide polymorphisms, and off-target toxicity affecting normal CD33-

expressing cells (Swaminathan & Cortes, 2023).

Among other novel agents, hedgehog pathway inhibitors have emerged as promising therapeutics, with aberrant activation of the Sonic Hedgehog receptor Smoothened (SMO) representing a key pathological feature in AML. The SMO inhibitor Glasdegib was approved by the FDA in 2018 for use in combination with low-dose Cytarabine in patients over 75 years of age (Jamieson et al., 2020). Despite advances in targeted therapies, immunotherapy in AML remains challenging due to the disease's complex immune evasion strategies, including the expression of inhibitory T cell ligands such as PD-L1, Gal-9, CD155, and NKG2DL, which promote T-cell exhaustion and expansion of immunosuppressive populations like myeloid-derived suppressor cells and tumor-associated macrophages (Tettamanti et al., 2022).

Despite substantial advances in AML therapy, improving long-term survival remains a major challenge. Ongoing efforts focus on optimizing combination regimens, developing novel agents with enhanced efficacy and reduced toxicity, and advancing personalized and immunotherapeutic approaches, which collectively hold promise for significantly improving AML outcomes in the coming decade.

1.2 Autophagy and its role in AML

Autophagy is a cellular process in which cells degrade and recycle their own components through a lysosome-dependent mechanism. This "self-digests" action allows the cell to manage impaired organelles or excess nutrient particles, ensuring their repurposing for cellular needs. Autophagy is typically triggered under stress conditions such as environmental challenges like starvation, high temperature, low oxygen levels, hormonal signals, or intracellular stresses including the accumulation of mutated proteins or damaged organelles (Levine, 2007). This process plays a critical role in maintaining cellular homeostasis, influencing cell survival, and regulating cell fate.

1.2.1 Autophagy is essential for cellular homeostasis

Autophagy can be categorized into different types based on the mediating factors and cargo involved. These types include chaperone-mediated autophagy, microautophagy, and macroautophagy. Among these, macroautophagy is the most commonly studied process. In this thesis, we discuss autophagy in the context of macroautophagy.

As illustrated in Figure 1.5, the autophagic process involves several stages. It begins with the initiation phase, during which cellular membrane sources give rise to vesicle nucleation and extension, forming the isolated membrane known as the

phagophore. This is followed by an elongation phase, during which the phagophore matures into an autophagosome, a double-membrane structure that sequesters cytoplasmic components destined for degradation. Subsequently, the autophagosome fuses with lysosome, resulting in the formation of an autolysosome. This fusion delivers lysosomal digestive enzymes, which degrade the sequestered proteins and other macromolecules within the autolysosome (Levine & Kroemer, 2008).

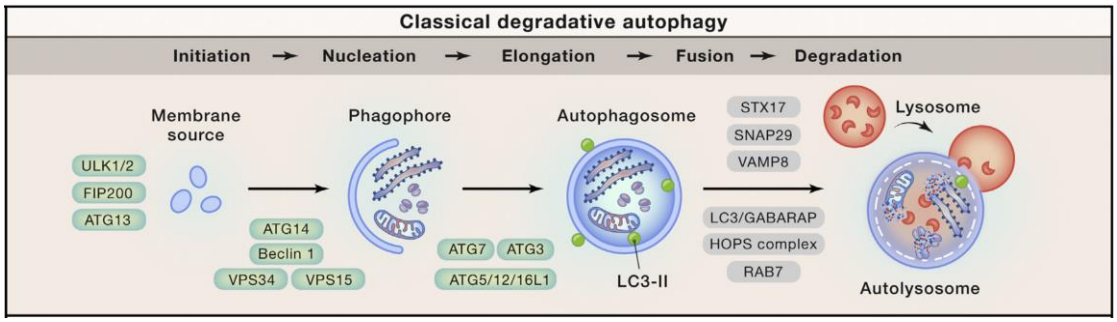

Figure 1.5 Classical autophagy process (Levine & Kroemer, 2008).

Various regulatory members participate in the autophagic process. Upon autophagic stimulation, the ULK1 complex, which consists of the ULK1 protein kinase, FIP200 scaffold protein, ATG13, and ATG101, integrates nutrient and energy sensing signaling to initiate autophagy. The class III phosphatidylinositol 3-kinase complex (PI3KC3) plays a dual role in the downstream: it either produces phosphatidylinositol 3-phosphate (PI3P) to promote autophagosome nucleation, mediated by members such as Beclin-1, VPS34, VPS15, and ATG14, or facilitates the maturation of endolysosomes and autolysosomes via pathways involving Beclin-1, VPS34, VPS15, and UVRAG.

The elongation and completion of the autophagosome rely on conjugation systems of ubiquitin-like proteins. These systems include ATG12 binding to ATG5 and ATG16L1, as well as LC3 and the conjugation with phosphatidylethanolamine (PE). However, studies have shown that this conjugation system is not essential in mammals. The fusion of the autophagosome with the lysosome to form the autolysosome requires complex regulation. This includes pH sensing in the lysosome, interactions with phospholipids, and the involvement of various proteins such as cytoskeletal motor proteins (e.g., dynein), SNARE proteins, the HOPS complex, LC3 family proteins, and Rab7. Together, these components coordinate the fusion process to ensure effective autophagic degradation (Levine & Kroemer, 2019).

Dysfunctional autophagy contributes to a range of pathological conditions, acting as a double-edged sword with both cytoprotective and cytotoxic effects. Loss-of-function studies, such as *Atg5* or *Atg7* knockout models, underscore the critical pro-survival role of autophagy, as evidenced by the rapid postnatal death of affected mice (Kuma et al., 2004; Levine & Kroemer, 2019). Impaired autophagy leads to the accumulation of aberrant proteins, resulting in neurodegenerative diseases like Alzheimer's, Parkinson's, and Huntington's disease (Park et al., 2020), as well as non-alcoholic fatty liver disease and various cardiac pathologies, where restoration of autophagic activity has demonstrated therapeutic potential (Qian et al., 2021; Wu et al., 2021).

1.2.2 Autophagy plays a role in leukemogenesis

Among the pathological dysfunctions associated with autophagy, tumorigenesis is one of the most severe outcomes of disrupted autophagy. Studies have shown that the relationship between tumorigenesis and autophagy is complex and often contradictory, as autophagy can either suppress or promote cancer cell growth, as described in Figure 1.6.

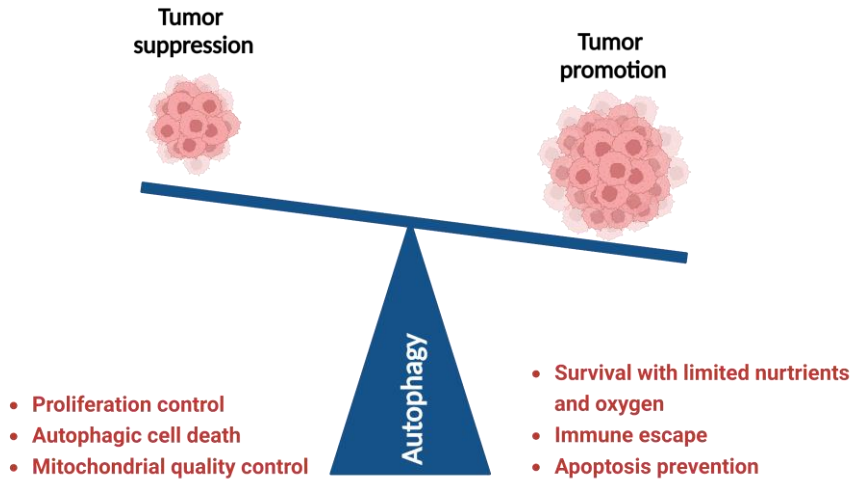

Figure 1.6 Conflicting regulation of autophagy in tumorigenesis

Autophagy plays a critical housekeeping role in early tumorigenesis by removing abnormal organelles and degrading proliferative proteins, thereby regulating cell proliferation. Disruption of autophagy, often due to aberrations in key regulators such as Beclin-1/ATG6, which is frequently monoallelically deleted in breast, ovarian, and prostate cancers, has been implicated in various malignancies, including lymphomas, liver, and lung cancers (Choi, 2012). Oncogenic pathways involving PI3K and AKT

suppress autophagy (Levine, 2007), whereas autophagy-promoting factors such as ATG4C, BH3-only proteins, UVRAG, PTEN, and AMPK exhibit tumor-suppressive effects (Choi, 2012).

The tumor-suppressive function of autophagy is closely linked to its interplay with autophagic cell death (ACD), classified as type II programmed cell death, differs mechanistically from apoptosis (type I programmed cell death) but can facilitate apoptotic pathways, particularly through the degradation of stressed organelles and subsequent activation of mitochondrial apoptosis. Evidence for this cross-talk includes the inability of the apoptosis inhibitor Z-VAD to induce cell death in *ATG7*- or *Beclin-1*-deficient cells (Jung et al., 2020), and the role of ATG12 in promoting mitochondrial apoptosis by inactivating pro-survival BCL-2 family proteins (Noguchi et al., 2020). In contrast to ACD, autosis represents a distinct, autophagy-dependent, non-apoptotic cell death pathway regulated by Na^+/K^+-ATPase, as characterized by Levine and colleagues (Liu et al., 2013; Liu & Levine, 2015). Potent autophagy inducers such as Tat-Beclin-1 peptide and ginger extract have been shown to trigger autosis in cancer cells, marked by increased LC3-II and decreased p62 without caspase activation (Liu et al., 2013; Akimoto et al., 2015).

Under conditions of low oxygen and limited nutrient availability, which are common in the tumor microenvironment, autophagic activity helps tumor cells survive these environmental challenges. For instance, active autophagy has been shown to delay

and mitigate apoptosis induced by sulindac sulfide by blocking mitochondrial death signaling (Kondo et al., 2005). Autophagy also aids cancer cells in immune evasion by modulating MHC class I presentation. In pancreatic ductal adenocarcinoma (PDA) models, downregulation of MHC-I has been linked to autophagy-mediated pathways. Notably, blocking autophagy or lysosomal function was found sufficient to restore MHC-I levels (Hernandez & Perera, 2022).

Hematopoietic stem cells (HSCs) and myeloid progenitor cells exhibit high autophagic flux to support their differentiation and proliferation, whereas AML cells typically display reduced autophagic activity, potentially due to copy-number loss (Lalaoui et al., 2016). Mouse models deficient in *ATG5* or *ATG7* demonstrate increased susceptibility to leukemogenesis, with impaired cellular differentiation possibly linked to aberrant Notch signaling (Lalaoui et al., 2016; Chen et al., 2024). Autophagy is essential for nutrient regulation and metabolic adaptation in AML, facilitating malignant cell survival and chemoresistance; for instance, *ATG5* heterozygosity alters glycolytic flux and promotes leukemogenesis, while *ATG3* deletion sensitizes AML cells to oxidative phosphorylation inhibition, highlighting the metabolic reliance of AML on autophagy. Additionally, ATG7 suppresses PKM2 phosphorylation, thereby inhibiting its interaction with FGFR1 and attenuating glycolysis (Chen et al., 2024). The functional role of autophagy in AML is further complicated by cytogenetic heterogeneity: autophagy induction during Cytarabine and daunorubicin treatment promotes chemoresistance, which can be reversed by autophagy inhibitors, and AML

cells with FLT3 mutations exhibit increased autophagic flux, with combined inhibition of autophagy and FLT3 yielding potent anticancer effects in vitro (Du et al., 2021). Conversely, activation of tumor-suppressive TP53 under cellular stress induces autophagy-mediated cell death via genes such as *DRAM1*, *SESN1*, and *SESN2*, and restoration of TP53 activity with MDM2 inhibitors enhances autophagy through AMPK activation, resulting in cytotoxicity in AML cells (Du et al., 2021; Seo et al., 2022).

Given the dual and context-dependent roles of autophagy in regulating cell survival and death, a comprehensive understanding of its mechanisms is essential for effective therapeutic exploitation, particularly in cancer. Although numerous autophagy-targeting agents are under investigation, few have achieved FDA approval. In AML and other malignancies, the bidirectional effects of autophagy underscore both the promise and complexity of developing targeted therapies, highlighting the necessity for further research to optimize clinical strategies.

1.2.3 Autophagy play a pivotal role in cancer immunotherapy

Beyond its role in suppressing cancer cell proliferation, autophagy contributes to tumor inhibition by orchestrating both innate and adaptive immune responses. Acting as a homeostatic surveillance mechanism, it autonomously degrades invading antigens, microorganisms, and damaged cellular components, setting the stage for immune activation.

In the context of tumorigenesis, innate immunity acts as the first line of defense. Tumor cells emit “eat me” signals, such as phosphatidylserine (PS), calreticulin (CRT), and oxidized phospholipids, which are recognized by receptors on antigen-presenting cells (APCs) like dendritic cells (DCs) and macrophages. This recognition triggers phagocytosis, engulfing cancer cells and degrading them into fragments, including neoantigen peptides. These peptides are then presented via MHC molecules, activating downstream cytotoxic T lymphocytes (CTLs) to initiate tumor cell clearance. During phagocytosis, significant crosstalk occurs between autophagy and LC3-associated phagocytosis (LAP). Shared regulatory factors, such as Beclin-1, the VPS complex, ATG7, ATG3, and LC3, facilitate the fusion of autophagosomes and LC3-associated phagosomes with lysosomes, as illustrated in Figure 1. 7 (Magné & Green, 2022). This interplay amplifies the immune response by enhancing antigen processing and presentation.

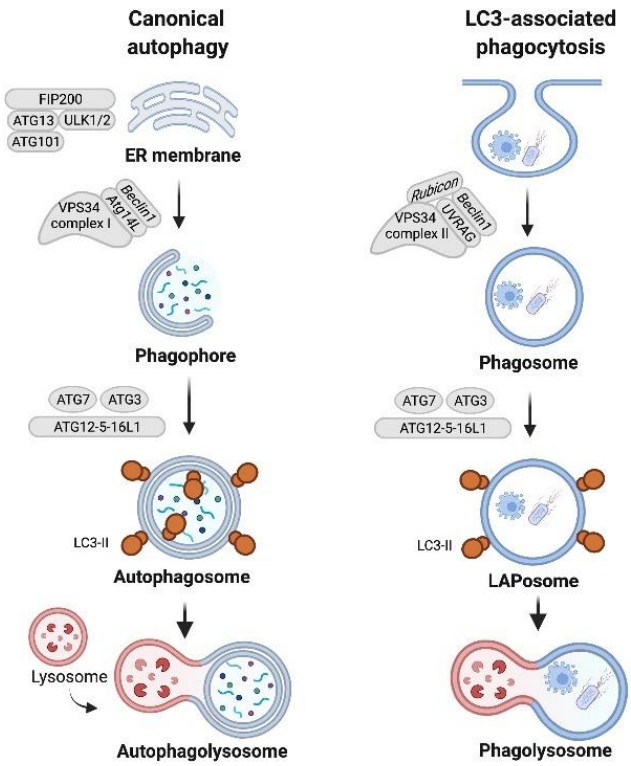

Figure 1.7 Autophagy and LC3-associsated phagocytosis (Magné & Green, 2022).

Autophagy also plays an indispensable role in adaptive immunity. In cytotoxic T cells, T cell receptor (TCR) stimulation triggers autophagy through rapid increases in intracellular calcium and subsequent activation of AMPK. AMPK phosphorylates the ULK1 complex, promoting autophagic activity that supports effector T cell differentiation and function. Deficient autophagy impairs T cell proliferation, suspending differentiation into S phase following TCR engagement (Jiang et al., 2019). Similarly, in B cells, interleukin-4 (IL-4) induces autophagy via JAK signaling and a PI3K-dependent pathway, enhancing antigen presentation to support adaptive immunity (Xia et al., 2018). Evidence showed that inducing autophagy in melanoma models via rapamycin, a known mTOR inhibitor, significantly increased $CD8^+$ T cell infiltration and tumor regression, highlighting autophagy's role in amplifying T cell-

mediated immunity (Botbol et al, 2016).

Moreover, autophagy contributes to the immunogenic properties of tumor cells, a key factor in driving robust immune activation. During chemotherapy, autophagy facilitates the efficient release of immunogenic molecules, such as extracellular ATP and HMGB1, from dying tumor cells. These damage-associated molecular patterns (DAMPs) enhance DCs maturation and activation, amplifying $CD8^+$ T cell responses against tumors (Michaud et al., 2011). Hydroxychloroquine combined with caloric restriction mimetics, enhanced autophagy-dependent ATP release, leading to superior tumor growth inhibition and increased CTL infiltration compared to chemotherapy alone in mouse models of colorectal cancer (Pietrocola et al, 2016).

In summary, autophagy plays a multifaceted role in the immune response against tumorigenesis, encompassing antigen processing, T cell priming, and the release of immunogenic signals, thereby establishing it as a cornerstone of cancer immunotherapy. Integrating autophagy into therapeutic strategies, as supported by evidence of improved anti-tumor outcomes, offers significant promise for advancing cancer treatment.

1.3 Mitochondrial dependency in AML Progression

1.3.1 Mitochondria as the multifaced cellular powerhouse

The mitochondrion is a central organelle essential for the maintenance of cellular physiological functions. Structurally, mitochondria are characterized by a double-membrane architecture, comprising a distinct outer mitochondrial membrane (OMM) and an inner mitochondrial membrane (IMM), which encloses the mitochondrial matrix and is separated from the OMM by the intermembrane space (IMS). The IMM is extensively folded into cristae, which serve to increase the surface area available for the localization of numerous enzymes and protein complexes integral to mitochondrial metabolism and the regulation of cell fate, as depicted in Figure 1.8 (Peng et al., 2023).

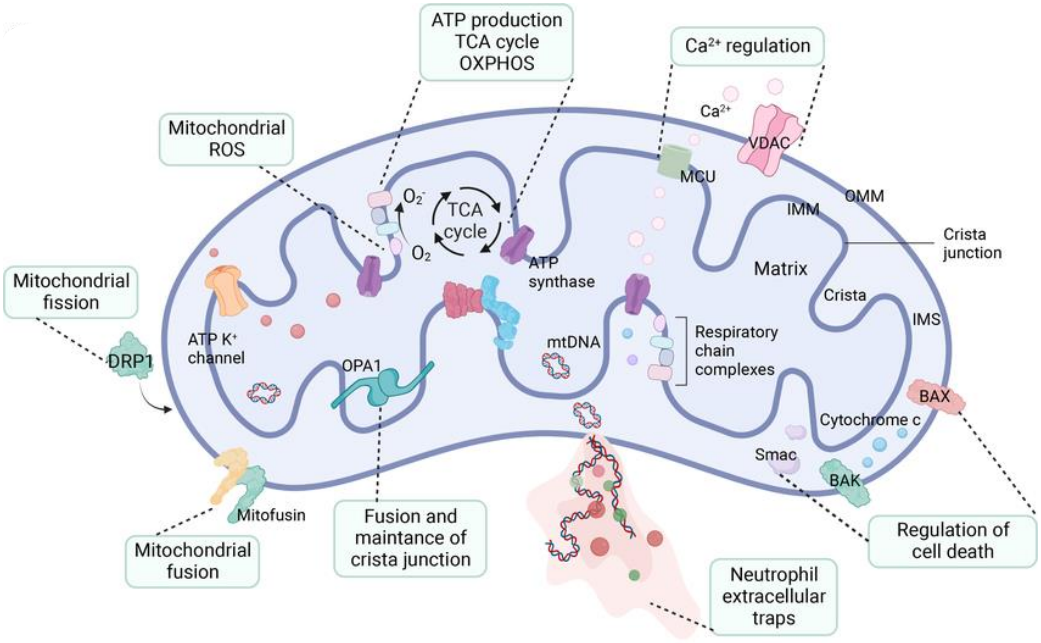

Figure 1.8 Overview of mitochondrial functions (Peng et al, 2023).

Mitochondrial ATP synthesis is primarily driven by the tricarboxylic acid (TCA) cycle and oxidative phosphorylation (OXPHOS), both of which are dependent on the coordinated function of the electron transport chain (ETC) complexes, ATP synthase, and the maintenance of a proton gradient across the IMM (Bertram et al., 2006; Martínez & Chandel, 2020). This electrochemical gradient establishes the mitochondrial membrane potential (ΔΨm), a hallmark feature of functional mitochondria. Beyond its critical role in ATP production, ΔΨm also facilitates the transport of ions such as calcium (Ca^{2+}) and potassium (K^{+}). Specifically, Ca^{2+} uptake into the mitochondrial matrix is mediated by the mitochondrial calcium uniporter (MCU), a process driven by ΔΨm. Subsequent export of Ca^{2+} to the IMS occurs via Na^{+}/Ca^{2+} or H^{+}/Ca^{2+} exchangers, thereby maintaining mitochondrial and cellular Ca^{2+} homeostasis. As a pivotal second messenger, Ca^{2+} orchestrates mitochondrial responses to cytosolic signals, effectively linking cellular energy demands to mitochondrial output. Under physiological conditions, the exchange of molecules and ions across mitochondrial membranes is tightly regulated, with the permeability transition pore restricting the passage of molecules larger than approximately 1.5 kDa.

Upon exposure to pathological stimuli, mitochondrial dysfunction can compromise cellular homeostasis and precipitate cell death by disrupting energy production and initiating deleterious signaling cascades. For instance, a reduction in ΔΨm, as observed in cells subjected to malignant or stress stimuli, leads to impaired membrane integrity and mitochondrial dysfunction. Disruption under these conditions

results in excessive generation of reactive oxygen species (ROS), which can induce oxidative damage, activate redox-sensitive signaling pathways, and trigger the opening of the mitochondrial permeability transition pore (MPTP). While transient MPTP opening may facilitate the selective removal of damaged mitochondria or cells via autophagy, sustained pore opening—often due to persistent ROS production or calcium overload—can result in catastrophic cellular outcomes, contributing to the pathogenesis of conditions such as ischemia-reperfusion injury, cardiac dysfunction, and age-related diseases (Zorov et al., 2014; Palma et al., 2024).

1.3.2 Mitochondrial dysfunction as potential target for AML therapy

The induction of mitochondrial damage in tumor cells has emerged as a promising strategy for inhibiting cancer cell proliferation. Lethal activation of the MPTP—triggered by factors such as excessive ROS, calcium overload, pH alterations, or pharmacological agents—compromises mitochondrial membrane selectivity, dissipates the mitochondrial membrane potential, and permits the passage of larger molecules. This process results in mitochondrial swelling, cristae disintegration, and the release of mitochondrial DNA and pro-death signals. These molecules serve as danger-associated molecular patterns (DAMPs), initiating mitochondria-mediated cell death pathways such as apoptosis or pyroptosis, as illustrated in Figure 1.9 (Bonora et al., 2022; Flores-Romero et al., 2023).

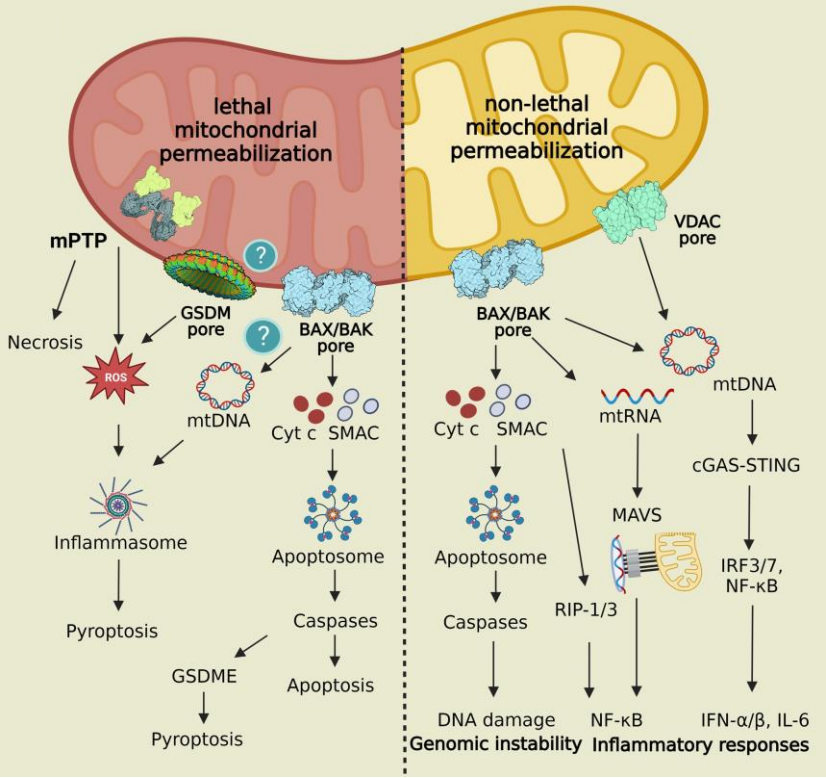

Figure 1.9 MPTP in cell death and inflammation (Flores-Romero et al., 2023).

Mitochondrial metabolism is increasingly recognized as a critical factor in the maintenance of leukemogenesis. Both rapidly proliferating AML blasts and leukemic stem cells (LSCs) exhibit a high demand for mitochondrial-derived energy. However, evidence suggests that LSCs are particularly reliant on oxidative phosphorylation (OXPHOS) compared to AML cells. Therefore, targeting OXPHOS represents a promising strategy for the selective eradication of LSCs, which are notoriously resistant to conventional therapies and contribute to disease relapse and poor patient outcomes—one of the major challenges in AML treatment (Peng et al., 2022; Egan & Schimmer, 2023). Furthermore, direct mitochondrial transfer from bone marrow mesenchymal stromal cells to AML blasts via tunneling nanotubes has been observed, further supporting the metabolic requirements of AML cells (Griessinger et al., 2017).

Clinical evidence from a proteomic analysis of 252 AML patients identified a distinct subtype, termed "Mito-AML," characterized by significant overexpression of mitochondrial proteins and associated with poor prognosis. This study demonstrated that the pathological features of Mito-AML are linked to aberrant mitochondrial metabolism, and this subtype exhibits hypersensitivity to agents targeting mitochondrial complex I (Jayavelu et al., 2022). Notably, of the eleven novel drugs approved by the FDA for AML since 2017, four are directly associated with the induction of mitochondrial cell death or the modulation of mitochondrial metabolism, as discussed in Section 1.1.3. This remarkable progress underscores the therapeutic potential of targeting mitochondria in AML. In addition to these approved agents, a diverse array of candidate drugs targeting mitochondrial-associated cellular processes—including Mcl-1 inhibitors, OXPHOS inhibitors, TCA cycle inhibitors, and electron transport chain (ETC) inhibitors—are currently in clinical or preclinical development (Panina et al., 2021; Firmanty et al., 2024).

In summary, mitochondria are pivotal organelles orchestrating a wide range of cellular activities, from energy production to the regulation of cell death. Therapeutic strategies that modulate mitochondrial function represent a promising avenue for cancer treatment. In AML, both preclinical and clinical evidence support the notion that targeting mitochondrial metabolism can effectively eliminate leukemic cells, reduce disease burden, and improve patient prognosis.

1.4 Peptides targeting Beclin-1 as a potential anti-cancer novel therapy

1.4.1 Optimization strategy for peptide drugs

With further advancements in functional and structural studies, protein-protein interactions (PPIs) have been shown to exhibit considerable complexity. However, they also offer inspiration for drug discovery. Targeting strategies based on PPIs have significantly advanced disease treatment, exemplified by antibody drugs, small molecules, and peptide-based therapies.

Peptide drugs are often considered challenging to develop due to their poor stability, susceptibility to degradation, and limited ability to penetrate cell membranes. These challenges result from their amino acid composition, which makes them hydrophilic and charged, impeding intracellular delivery. Additionally, their short residue lengths often prevent the formation of secondary or tertiary structures, which are crucial for conformational stability. For instance, unmodified insulin is rapidly eliminated in vivo within minutes of administration. Despite these challenges, peptide drugs have gained increasing attention as a novel therapeutic modality in the past decade, driven by advances in structural biology, synthesis, and analytical techniques. Efforts to overcome these limitations include chemical modifications such as cyclization or stapling, nanoparticle formulations, and the attachment of ligands or linkers. For example, lipid conjugation to insulin has been shown to extend its in vivo half-life (Lee et al., 2019; Wang et al., 2022).

One noteworthy advancement is hydrocarbon stapling, a method for stabilizing the α-helical structure of peptides. First introduced by Verdine's lab in 2000, that olefin tethers were used at specific positions along the peptide sequence to enhance structural stability (Kim et al., 2011; Walensky & Bird, 2014). Stapling positions are typically located outside the target recognition interface, at positions such as “i, i+3,” “i, i+4,” or “i, i+7,” as shown in Figure 1.10 (Kim et al., 2011). Hydrocarbon-stapled peptides exhibit improved in vivo functionality in modulating PPIs. For instance, stapled BH3 peptides have demonstrated enhanced α-helicity, protease resistance, and increased binding affinity for Bcl-2 family proteins. This modification stabilizes α-helices of the BCL-2 domain (SAHBs) and improves interactions with Bcl-2 family members (Walensky & Bird, 2014). While concerns about cell penetration remain for some stapled peptides, the method has nonetheless demonstrated significant improvements in biological activity.

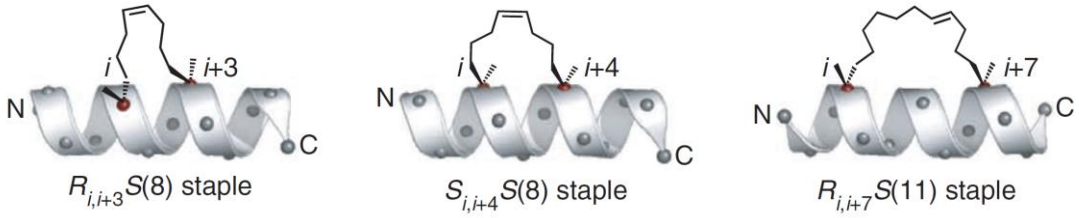

Figure 1.10 Three examples of hydrocarbon stapling (Kim et al., 2011).

Cell-penetrating peptides (CPPs) play a vital role in drug delivery. These short peptides, typically 4 to 40 amino acids in length, serve as vehicles for delivering various cargos, including nucleic acid-based drugs, nanoparticles, and small molecules, into

cells. The primary mechanism of delivery often includes endocytosis. One of the earliest examples of CPPs is the transactivator of transcription (Tat) peptide, derived from the HIV-1 Tat protein. Tat peptides were first identified as being capable of penetrating the cell membrane and internalizing to activate viral promoters. These peptides efficiently deliver macromolecules across the cell membrane, improving the bioavailability of their cargo with a short key sequence of RKKRRQRRR (Gump & Dowdy, 2007; Zorko & Langel, 2022). Shortly after, another CPP called penetratin, was discovered in the Antennapedia homeodomain of *Drosophila*. This 16-amino-acid peptide enables energy-independent internalization into live cells, driving cellular membrane translocation. These groundbreaking discoveries marked the beginning of the CPP field. To date, approximately 1,700 CPPs have been identified and are cataloged in the CPP database, CPPsite 2.0. Beyond their role in cargo delivery, CPPs have expanded functionalities, including acting as cellular modulators (Koren & Torchilin, 2012; Gori et al., 2023).

1.4.2 Rational design of stapled peptides targeting Beclin-1

Beclin-1, the first mammalian autophagy protein identified, functions as a scaffold protein within the PI3KC3 and is characterized by a central coiled-coil domain (CCD), an evolutionarily conserved domain, and a Bcl-2 homology 3 (BH3) domain. The BH3 domain mediates interaction with Bcl-2, stabilizing Beclin-1 homodimerization, while the CCD enables context-dependent interactions with Atg14L or UVRAG, as displayed

in Figure 1.11 (Funderburk et al., 2010; Levine et al., 2015). Through recruitment of Atg14L or UVRAG, Beclin-1 assembles two distinct PI3KC3 complexes—PI3KC3-C1 and PI3KC3-C2 — each comprising Vps34 and Vps15, which are essential for autophagy, endo-lysosomal trafficking, and phagocytosis (Lu et al., 2014; Levine et al., 2015).

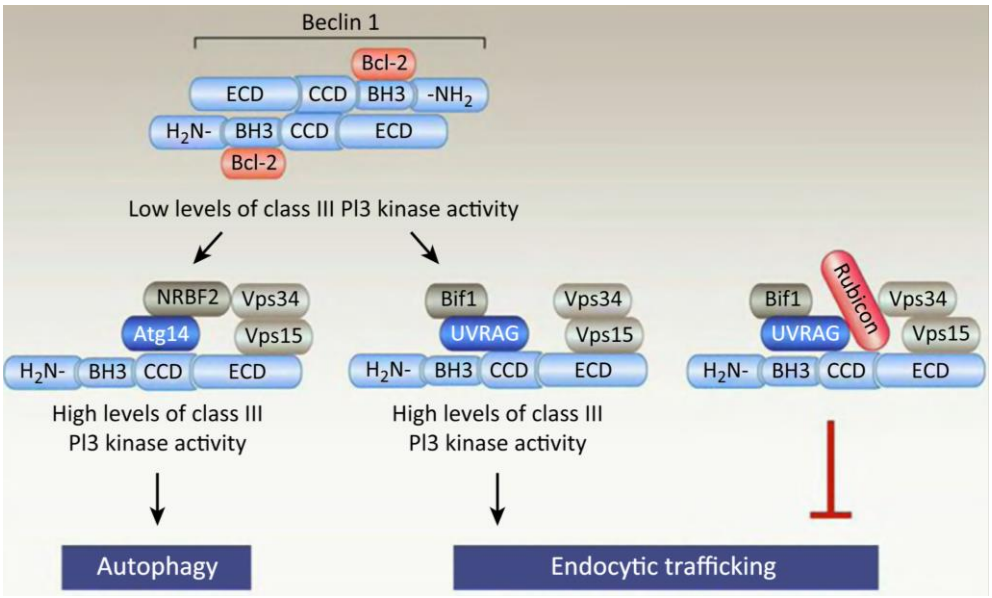

Figure 1.11 Beclin-1 as scaffold member of PI3KC3 (Lu et al,2014; Levine et al, 2015).

In our previous structural study, we identified the core binding site responsible for the interaction of Atg14L and UVRAG with Beclin-1, located within the coiled-coil domain (CCD) of Beclin-1. Specifically, the key binding occurs in the N-terminal half of the CCD. Additionally, we discovered that UVRAG has a higher binding potency, enabling it to outcompete Atg14L in interacting with the Beclin-1-Vps34 complex to facilitate endosomal trafficking. To enhance the protein-protein interactions between

Atg14L or UVRAG and Beclin-1, we designed peptide mimetics using rational design principles and computational approaches, including the creation of virtual libraries and binding affinity screening. These peptides are intended to strengthen Beclin-1's interaction with its substrates, thereby increasing autophagic activity and enhancing cancer cell cytotoxicity (Wu et al., 2018).

By employing hydrocarbon stapling techniques to stabilize the α-helical structures, we initially developed peptides stapled at the "i, i+7" positions. These peptides were further optimized by attaching a cell-penetrating sequence (YGRKKRRQRRR) at the N-terminus. Among these, a lead candidate, Tat-SP4, demonstrated favorable binding affinity to Beclin-1, with a dissociation constant (Kd) of approximately 6.8 μM. Further optimization, involving repositioning the staple closer to the peptide-Beclin-1 interface, led to the identification of another lead candidate, Tat-SP9. Tat-SP9 exhibited excellent cytotoxicity against cancer cells and was selected for further studies, as illustrated in Figure 1.12 (Wu et al., 2018; Yang et al., 2021).

A

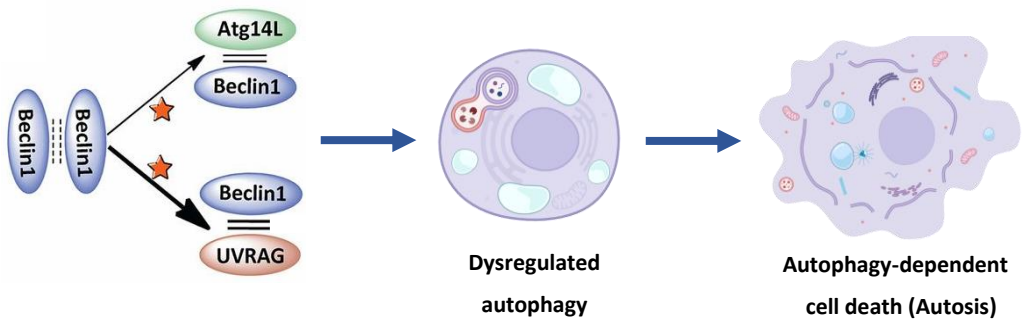

B

Number	Sequence	Interaction energy (kcal/mol)
SP1	Ac-RLIQEL(R8)DREAQR(S5)V-NH₂	-29.75±6.62
SP2	Ac-RLIQEL(R8)DREAQR(S5)S-NH₂	-43.69±5.21
SP3	Ac-RLISEL(R8)DREKQR(S5)V-NH₂	-47.51±3.96
SP4	Ac-RLISEL(R8)DREKQR(S5)A-NH₂	-56.05±6.87
SP5	Ac-RLIQEL(R8)DREKQR(S5)S-NH₂	-40.75±5.59
SP6	Ac-RLISEL(R8)DREKQR(S5)S-NH₂	-47.40±6.90
SP7	Ac-RLIQEL(R8)DREKQR(S5)R-NH₂	-45.77±5.13
SP8	Ac-RLIQEL(R8)DREKER(S5)A-NH₂	-49.78±6.34
SP9	Ac-LLISEL(R8)DREKQR(S5)A-NH₂	-74.52 ±4.31
SP10	Ac-RLLSEL(R8)DREKQR(S5)A-NH₂	-55.69 ±5.15
SP11	Ac-LLLSRL(R8)DREKQR(S5)A-NH₂	-50.47 ±5.23
SP12	Ac-LLISQL(R8)DREKQR(S5)A-NH₂	-56.05±4.35

C

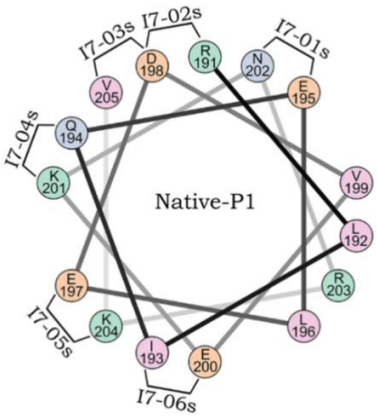

D

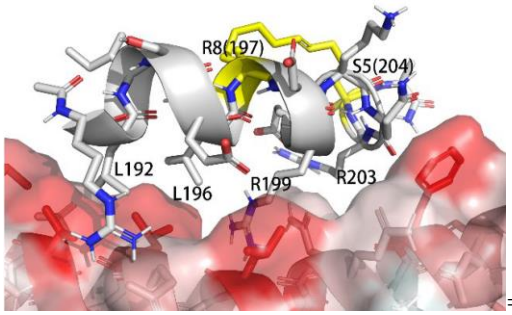

=

E

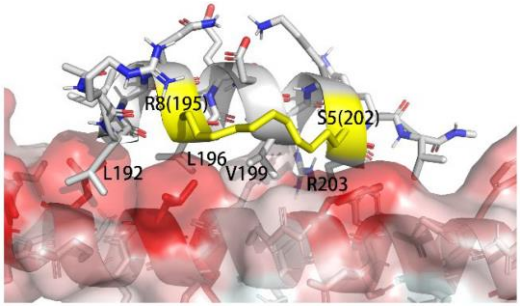

Figure 1.12 Beclin-1 targeting peptides (Wu et al., 2018; Yang et al., 2021). (A) Tat-SPs design strategy, star stands for Tat-SPs; (B) Sequence of stapled peptides; (C) and (E) Optimization of stapling sites; (D) Interaction prediction of Tat-SP4 and Beclin-1.

Chapter 2 Objectives

This project aims to advance therapeutic development and explore improved strategies for the treatment of acute myeloid leukemia (AML). Specifically, we investigate the application of Beclin-1-targeting stapled peptides as potential anticancer agents to address the challenges of AML treatment and improve patient survival outcomes. The research encompasses comprehensive studies on the antiproliferative effects, mechanisms of action, therapeutic efficacy, and pharmacokinetics of these peptides to evaluate their potential as novel anti-AML drug candidates.

Objective 1: Characterization of Beclin-1 targeting stapled peptide as anti-proliferative agents in acute myeloid leukemia cell lines.

Antiproliferation investigation will be conducted to evaluate the cytotoxic effects of Tat-SPs on AML cell lines. We will focus on two lead candidate peptides, Tat-SP4 and Tat-SP9, which came from our first- and second-generation design studies. The study will assess the anti-proliferative effect of both peptides across a broad range of AML cell lines. This comprehensive analysis aims to identify sensitive cell lines, which will subsequently be prioritized for efficacy studies and in vivo assessments of anti-AML outcomes.

Objective 2: Investigation of cell death mechanisms induced by Beclin-1-targeting stapled peptides.

To elucidate the molecular mechanism of anti-proliferation by our designed Tat-SPs, we will first investigate whether programmed cell death pathways, including apoptosis, ferroptosis, necroptosis, and pyroptosis, are involved. We will make use of specific inhibitors for these cell death programs and study whether they would rescue the anti-proliferative effect of Tat-SPs. Additionally, as Tat-SPs are designed to enhance Beclin-1 activity and promote autophagic activity, the impact of Tat-SPs on autophagy in different AML cell lines will be analyzed. Furthermore, considering previous findings that Tat-SPs trigger mitochondrial dysfunction, the impact of Tat-SPs on mitochondrial activity in AML cells will also be thoroughly investigated. These studies aim to provide a comprehensive mechanistic framework for the functional effects of Tat-SPs, informing their therapeutic optimization and minimizing potential toxicity for future in vivo applications.

Objective 3: Evaluation of the anti-leukemic efficacy of stapled peptides in animal models of AML.

In vivo validation is essential for assessing the anti-AML efficacy of Tat-SPs. The first step is to establish suitable mouse models. AML cells will be introduced into the hematological system via intravenous injection. For xenograft models, immune system

suppression may be necessary and could involve the use of immunodeficient mouse strains or the application of immune-disrupting chemical agents or radiation, as described in prior research. The administration method will follow protocols established in previous studies on other cancer models, with intraperitoneal injection being the primary approach considered. The efficacy of Tat-SPs will be evaluated based on leukemia burden in AML-bearing mice, and overall survival data will be collected to determine therapeutic outcomes.

Objective 4: Analysis of the pharmacokinetic profiles of stapled peptides to assess their drug-like features *in vivo*

Druggability is a critical criterion for the in vivo application of novel therapies. In addition to efficacy studies, pharmacokinetic analyses will be conducted to investigate the dynamic behavior of Tat-SPs following their entry into the circulatory system. Plasma concentration-time curves will be generated by detecting the intact peptide using LC-MS/MS methods. Pharmacokinetic parameters will be analyzed using a noncompartmental model with WinNonlin software. Fundamental dynamics, including absorption and elimination profiles of Tat-SPs, will then be characterized. Unlike efficacy studies, pharmacokinetic experiments will be performed in healthy mouse models to ensure a controlled evaluation of peptide dynamics. These pharmacokinetic insights will provide valuable guidance for optimizing peptide design, administration routes, dosing regimens, and potential toxicity mitigation strategies.

Chapter 3 Materials and Methodology

3.1 Cell lines and cell culture

THP-1 and RAW264.7 cell lines were obtained from the American Type Culture Collection (ATCC). Molm13 and OCI-AML3 cell lines were purchased from Wuhan Pricella Biotechnology Co., Ltd., while MV-4-11 and Kasumi-1 cell lines were acquired from the Cell Bank/Stem Cell Bank, Chinese Academy of Sciences. The HL60 cell line was generously provided by Prof. Larry Chow's laboratory, and the Jurkat E6.1 cell line was kindly donated by Prof. Qian Zhao's laboratory. The culturing conditions for these cell lines are summarized in Table 3.1.

Table 3.1 Cell culture conditions

Cell line	Base medium	Complete media additives
THP-1	RPMI 1640 (Gibco)	10% FBS (Gibco), 0.05 mM 2-mercaptoethanol (Gibco)
HL60		10% FBS (Gibco)
Molm13		10% FBS (Gibco), 1% Penicillin-Streptomycin (Gibco)
Jurkat e6.1		10% FBS (Gibco)
Kasumi-1		20% FBS (Gibco)
OCI-AML3	IMDM (Gibco)	10% FBS (Gibco), 1% Penicillin-Streptomycin
MV-4-11	IMDM-GlutaMAX	10% FBS (Gibco)
RAW264.7	DMEM (Gibco)	10% FBS (Gibco)

The Molm13-GFP-luc cell line was generated in our laboratory by transducing Molm13 cells with reporter genes. Molm13 cells were seeded in 24-well plates at a

density of 5×10^5 cells per 0.5 mL per well. Gradient concentrations of puromycin were applied for tolerance selection, with media replacement conducted every two days for up to seven days. A concentration of 5μg/mL puromycin was determined as optimal for subsequent lentiviral transfection. For lentiviral transfection, Molm13 cells were treated with lentiviral solution and ADV infection reagent (WZ Biosciences) at the recommended multiplicity of infection (MOI) for three days. Puromycin was then added to select for successfully transfected cells. Transfected Molm13 cells expressing the luciferase tag were subsequently used in efficacy experiments.

3.2 Cell viability assay

For the IC50 assay, 96-well microplates were used for cell seeding. Depending on their proliferation rates, 4×10^4 to 5×10^4 cells per well were seeded. Drug treatments at the desired concentrations were applied later, and the plates were incubated at 37°C and 5% CO_2 atmosphere for 24 hours. Cell viability was assessed using Trypan Blue (Gibco) and the CellTiter-Lumi™ Luminescent Cell Viability Assay Kit (Beyotime).

For the 5-day proliferation assay, lower cell densities, 1×10^4 to 2.5×10^4 AML cells per 0.5mL, were seeded in 24-well culture plates. After drug administration, cells were cultured for 5 days, and cell counts were recorded every 24 hours using the Trypan Blue exclusion method. Experiments were conducted in replicates and statistical analysis of the data was performed using GraphPad Prism 8.0.

3.3 Colony formation assay

The colony formation assay was performed using agar-containing culture media. RPMI 1640 medium was mixed with agar to prepare two concentrations: 0.3% and 0.6%. A base layer of 0.6% agar-medium was added to a 6-well plate and allowed to solidify for 1 hour. HL60 cells were then treated with the desired conditions and mixed with 0.3% agar-medium, which was layered on top of the 0.6% agar-medium. Then cells were incubated in 37°C and 5% CO_2 condition. After 14 days of incubation, colonies were stained with Nitro Blue Tetrazolium Chloride (NBT, Invitrogen) to visualize colony formation under different treatment conditions.

3.4 Flow cytometry analysis

A total of 4×10^5 to 5×10^5 AML cells/mL were seeded in 12-well culture plates. Cells were treated with Tat-SPs or specific stimulators in culture media under different experimental conditions and subsequently stained with fluorescent dyes. At the designated time points, cells were collected, the culture media were removed, and samples were washed with PBS. The cells were then resuspended in PBS and analyzed using a BD Accuri C6 Flow Cytometer.

Apoptosis detection in Tat-SP9-treated HL60 cells was also performed using Propidium Iodide and Annexin V Alexa Fluor™ 488 (Gibco) with provided binding

buffer. TMRM (tetramethylrhodamine methylester, Invitrogen) was used for assessing mitochondrial membrane potential. Cellular ROS levels were evaluated using CellROX® Green Flow Cytometry Assay Kits (Invitrogen). MitoProbe™ Transition Pore Assay Kit (Invitrogen) was employed to test mitochondrial permeability transition pore (MPTP) activation.

For phagocytosis observation, RAW264.7 cells were seeded in 12-well plates at a density of 4.5×10^5 cells/mL per well. Phagocytosis activation was induced by treating the cells with 500ng/mL LPS and Tat-SP4 overnight. Molm13-GFP-luc cells were then added to the activated RAW264.7 cells at a density of 1.5×10^5 cells per well, and co-treatment was conducted overnight. After co-treatment, non-phagocytosed Molm13-GFP-luc cells were removed by PBS washing, and GFP signals in RAW264.7 cells were analyzed using a BD Accuri C6 Flow Cytometer.

3.5 Seahorse extracellular flux analysis

Mitochondrial oxidative phosphorylation (OXPHOS) was assessed using the Seahorse XF Cell Mito Stress Test Kit with the XFe24 Analyzer (Agilent). The assay began with plate preparation, where 50μL of Poly-D-lysine was applied to a 24-well plate and incubated overnight at 4°C. After incubation, the coating solution was removed, the plate was washed, and AML cells were seeded at a density of approximately 2×10^5 cells per 0.5 mL per well in assay buffer. The plate was then

placed in a 37°C incubator without CO_2.

The sensor cartridge was loaded with mitochondrial respiration modulators, including Oligomycin (Cayman), FCCP (Cayman), Rotenone (Sigma), and Antimycin A (Sigma), to induce different stages of mitochondrial respiration alteration. Tat-SPs were also loaded, while in a distinct position in the cartridge. The loaded sensor cartridge was assembled with the cell-containing culture plate, and the entire setup was placed in the XFe24 Analyzer.

During the assay, stimulators were injected into the cells first, followed by sequential injections of the respiration modulators. This allowed observation of the effects of Tat-SPs on cellular oxygen consumption rates (OCR) at each stage. All experimental conditions were performed in replicates, with three measurements collected for each stage. Statistical analysis of the results was conducted using GraphPad Prism 8.0. Detailed information about this assay is available on the manufacturer's website: Agilent Seahorse XF Cell Mito Stress Test Kit.

3.6 Enzyme-Linked Immunosorbent Assay (ELISA) assay

The Human IL-2 Uncoated ELISA Kit (Invitrogen) was used with a 96-well plate (Corning) to quantify IL-2 levels. Jurkat e6.1 cells were cultured in 6-well plates at a density of 1×10^6 cells per 2 mL per well. Dynabeads™ Human T-Activator CD3/CD28

(Gibco) was used as a positive control at a 1:1 bead-to-T cell ratio, following the manufacturer's instructions. Treatments were incubated for 24 hours, after which cell culture supernatants were collected by centrifugation to remove cells and debris. IL-2 levels were measured via ELISA, and statistical analysis was performed using GraphPad Prism 8.0.

3.7 Real-Time quantitative PCR (qPCR)

Quantitative-PCR was performed on Jurkat e6.1 cells after 3 hours of stimulation under different conditions. Total RNA was extracted using the RNeasy™ Animal RNA Extraction Kit (Beyotime) and reverse-transcribed into cDNA using the PrimeScript™ RT Master Mix (Takara). cDNA samples were subjected to real-time PCR using *IL-2* qPCR primers (Genepharma), *GAPDH* qPCR primers (Beyotime), and TB Green Premix Ex Taq (Takara).

3.8 Confocal microscopy imaging

NFAT1 nuclear translocation was studied using confocal imaging. Jurkat e6.1 cells were seeded in 12-well culture plates at a density of 5×10^5 cells/mL. Positive controls included 50ng/mL PMA (Invitrogen) and 1μg/mL Ionomycin (MCE), alongside Tat-SPs treatments, incubated overnight. Stimulated T cells were transferred onto Poly-D-lysine-coated slides placed in 12-well plates. After centrifugation to settle

the cells on the slides, PBS washing and fixation procedures were performed. Immunofluorescence staining was conducted, and slides were imaged using a Leica TCS SP8-MP confocal microscope.

3.9 Western blot analysis

To collect cell lysates under different treatment conditions, cells were centrifuged to remove culture media at 1500rpm for 5 minutes or 3000rpm for 3 minutes, depending on their sensitivity to centrifugation. The cell pellets were washed with PBS two to three times. Subsequently, the cells were lysed using a lysis buffer containing 1% protease inhibitor cocktail. The lysis process was facilitated by vortexing, and once complete, the lysates were boiled for 10 minutes to denature proteins. Protein samples were then stored at −80°C until further use.

SDS-PAGE was used to separate target proteins, followed by transfer to PVDF membranes for protein-protein interaction analysis. Primary antibodies used in this study included Anti-LC3 (CST), Anti-p62 (CST), Anti-Cleaved PARP (CST), Anti-Caspase 3 (CST), Anti-Gasdermin D (Abcam), and Anti-β-actin (Santa Cruz Biotechnology). Secondary antibodies included Anti-Mouse IgG-HRP (Invitrogen) and Anti-Rabbit IgG-HRP (Sigma-Aldrich).

3.10 AML Animal experiments

Subcutaneous AML model: Male Balb/c nude mice, 4 weeks old, 20 g, n=6 per group, were used to establish a subcutaneous AML model. One million Molm13 cells, suspended in Matrigel, were injected near the armpit to induce solid tumor growth. Treatment started when tumors reached 70mm^3 and continued until they reached 1500mm^3, per animal ethics requirements. Tumor volume and mouse weight were monitored, and tumor tissue was collected and weighed at the end of the experiment.

Molm13-GFP-luc AML model: Male Balb/c nude mice, 7 weeks old, 20 g, n = 7 per group, were used to establish the AML model. Mice were pretreated with 150mg/kg cyclophosphamide for two consecutive days prior to inoculation. AML was induced by injecting 1 × 10^5 Molm13-GFP-luc cells in 100μL PBS via the tail vein. Leukemia burden was monitored using the IVIS (In Vivo Imaging System), with bioluminescence signals correlating to tumor size and spread, as indicated by signal intensity and distribution. Imaging was conducted every five days to track AML progression. Survival outcomes were recorded, and the median survival time for each treatment group was calculated.

For treatment administration, mice were randomly assigned to three groups for subcutaneous AML model with PBS (control), 40mg/kg Tat-SP4, 10mg/kg Tat-SP9; and four groups for Molm13-GFP-luc AML model with PBS (control), 40mg/kg Tat-

SP4, 150mg/kg Venetoclax, and a combination treatment group. Tat-SPs was administered via intraperitoneal injection with PBS as the vehicle, while Venetoclax was delivered via oral gavage using a vehicle mixture of corn oil, 30% PEG400, and 10% ethanol. All treatments were administered once daily. Statistical analysis was performed using GraphPad Prism 8.0.

3.11 Pharmacokinetic profiling of Tat-SPs

Healthy male C57BL/6 mice, 4 to 6 weeks old, 20g, n = 6 per group, were used for pharmacokinetic analysis. Blood samples were collected into anticoagulant tubes at designated time points: 0min, 5min, 15min, 30min, 1hr, 2hr, 4hr, and 8hr, via tail vein. Plasma was obtained by centrifuging blood samples at 3500 rpm for 15 minutes. For each sample, 50μL of plasma was mixed with 250μL pre-chilled 4M urea to denature proteins and inhibit unexpected biochemical reactions. The mixture was centrifuged at 12,000rpm for 10 minutes. The supernatant was subjected to protein precipitation by adding 20μL methanol, 10μL trichloroacetic acid (TCA), and 50μL acetonitrile (ACN). After ACN extraction, the precipitate was centrifuged again, and the supernatant was lyophilized using a Labconco Refrigerated CentriVap Vacuum Concentrator.

3.12 Mass spectrometry analysis

Sciex 6500+ Liquid Chromatography/Electrospray Ionization-QTrap Mass

Spectrometer was applied to analyze the reconstituted PK samples. A T3 reversed-phase chromatography column was used as the stationary phase, with MilliQ water and LC/MS-grade acetonitrile containing 0.1% formic acid as the mobile phase. Statistical analysis was performed using GraphPad Prism 8.0. Pharmacokinetic parameters were estimated using a non-compartmental model in Phoenix WinNonlin 8.0.

3.13 Statistical analysis

All data were analyzed using GraphPad Prism 8.0. Statistical analyses, including ordinary one-way ANOVA, two-way ANOVA, umpired t-test, and Long-tank test for trend, were performed based on the experimental design and data characteristics. Western blot band intensities were quantified using Image J, followed by statistical evaluation. Mass spectrometry data were processed using Sciex OS software, and pharmacokinetic parameters were analyzed with WinNonlin 8.0.

Chapter 4 Evaluation of the anti-proliferative activity of Tat-SPs in AML cells

4.1 Measurement of antiproliferation efficacy of Tat-SPs in AML cells

To evaluate the antiproliferative effects of Tat-SP peptides, AML cells were seeded into 96-well plates and treated with varying concentrations of Tat-SPs on the same day. Two lead peptides were selected for investigation based on their binding affinity to Beclin-1: Tat-SP4 from the first generation and Tat-SP9 from the second generation. Following overnight incubation, antiproliferative activity was assessed by determining the half-maximal inhibitory concentration (IC_{50}) values. Previous IC_{50} measurements using MTT assays did not accurately quantify Tat-SP-induced cell death, as the assay signal may inversely correlate with actual cytotoxicity and thus may not fully reflect cell viability. To address this limitation, trypan blue exclusion staining was employed to more accurately assess the cytotoxic effects of Tat-SPs in AML cells.

Multiple human AML cell lines were utilized in this assay to comprehensively evaluate the cytotoxicity of Tat-SPs, including HL60, THP-1, Molm13, OCI-AML3, MV-4-11, and Kasumi-1. The inclusion of these cell lines ensured representation of diverse genetic backgrounds and mutational profiles commonly observed in AML. According to information provided by the manufacturers, both Molm13 and MV-4-11 cells harbor the *FLT3-ITD* mutation, the most prevalent subtype of *FLT3* alterations. The THP-1 cell line, derived from human acute monocytic leukemia, carries the *MLL-*

AF9 fusion gene. OCI-AML3 cells possess mutations in *NPM1* and *DNMT3A*, while Kasumi-1 cells are characterized by the *AML1-ETO* fusion gene. This panel of cell lines thus encompasses key genetic alterations relevant to AML pathogenesis and therapeutic response.

As shown in Figure 4.1, both Tat-SP4 and Tat-SP9 exhibited concentration-dependent cytotoxicity in AML cell lines following overnight incubation. HL60, THP-1, and Molm13 cells demonstrated greater sensitivity to Tat-SP4 compared to MV-4-11, OCI-AML3, and Kasumi-1 cells, a trend that was similarly observed with Tat-SP9. Notably, the second-generation peptide Tat-SP9 displayed enhanced antiproliferative activity, as evidenced by lower IC_{50} values across the tested cell lines relative to Tat-SP4. In particular, Tat-SP9 treatment resulted in a pronounced reduction in cell viability in Molm13 cells, with the lowest IC_{50} value observed at 4.30 μM.

The observed differences in IC_{50} values among the six AML cell lines are likely attributable to their distinct genetic backgrounds. The similar patterns of sensitivity across these cell lines for both first- and second-generation Tat-SPs suggest that these peptides may induce AML blast cell death via a shared underlying mechanism. Notably, the second-generation Tat-SP9 consistently exhibited greater cytotoxic potency, indicating that structural optimization of the peptide enhances its efficacy against AML cells.

A B

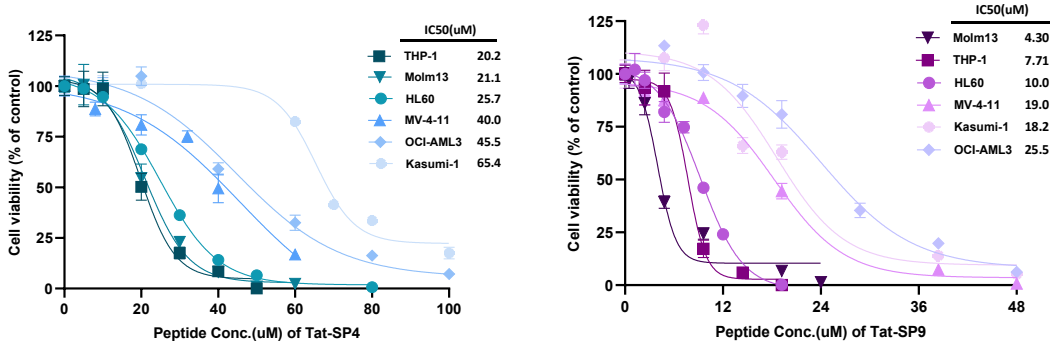

Figure 4.1 Antiproliferation efficacy of Tat-SPs in AML cell lines.

(A) Antiproliferation efficacy of Tat-SP4 in AML cell lines was assessed to determine IC_{50} values. (B) Antiproliferation efficacy of Tat-SP9 in AML cell lines was assessed to determine IC_{50} values. Cells were exposed to a range of peptide concentrations for 24 hours. Following treatment, viable cell numbers were quantified manually by hemocytometer using the trypan blue dye exclusion method. Data represent mean ± SEM of replicates.

A five-day cytotoxicity assay was established to evaluate the effects of Tat-SP peptides on AML blast cell viability. As shown in Figure 4.2, the chemotherapeutic agent cisplatin exhibited potent antiproliferative activity during the five-day culture period of HL60 cells. Treatment with 0.5 μM cisplatin resulted in a significant reduction in cell proliferation, while 1 μM induced even greater cytotoxicity, as evidenced by a sustained decrease in cell viability beyond 48 hours. Similarly, both Tat-SP4 and Tat-SP9 markedly inhibited AML cell growth over the five-day period. Specifically, 15 μM Tat-SP4 significantly impaired the proliferation of HL60, Molm13, and THP-1 cells,

and 25 μM nearly abolished cell viability in these lines. Tat-SP9 demonstrated even greater potency, with 5 μM inducing substantial cytotoxicity in the five-day assay, and treatment with 10 μM resulting in minimal survival of HL60 and Molm13 cells.

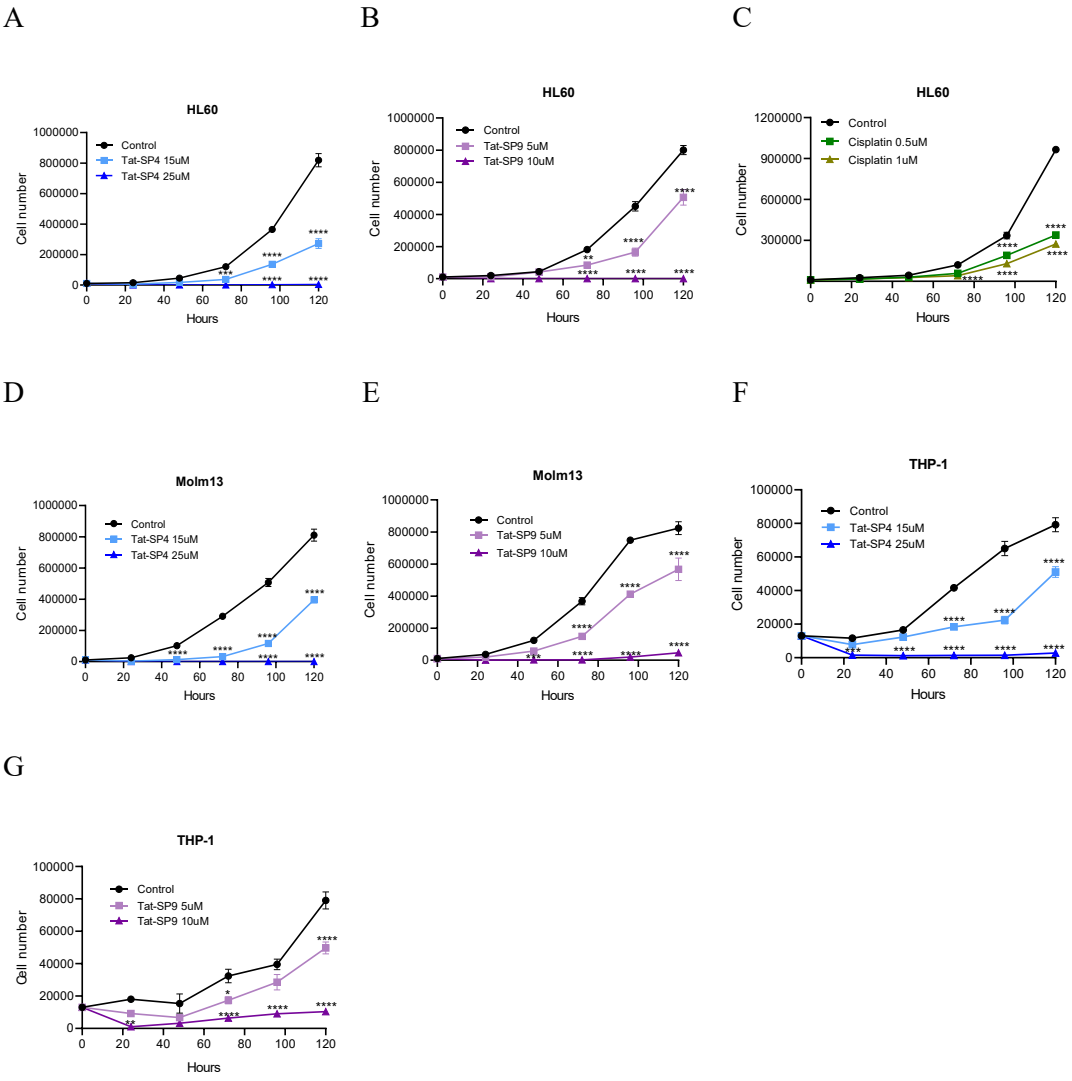

Figure 4.2 Antiproliferation effects of Tat-SPs on AML cell lines following 5 days treatment. (A–C) Proliferation of HL60 cells following treatment with the indicated concentrations of Tat-SP peptides and Cisplatin. (D, E) Antiproliferative effects of Tat-SPs in Molm13 cells. (F, G) Antiproliferative effects of Tat-SPs in THP-1 cells. Cell proliferation assays were conducted over a five-day period, with drug treatments

administered on day 0. Cell counts were determined every 24 hours using a hemocytometer and the trypan blue exclusion method. Data are presented as mean ± SEM of replicate experiments. Statistical significance was assessed by two-way ANOVA, $**P < 0.01$, $***P < 0.001$, $****P < 0.0001$.

In the five-day proliferation assay, HL60 and Molm13 AML cell lines exhibited rapid malignant growth, expanding from an initial seeding of 10,000 cells on day 0 to 800,000 to 1,000,000 cells by day 5. In contrast, THP-1 cells demonstrated a slower proliferation rate, with cell numbers increasing approximately tenfold over the same period. Despite these inherent differences in growth kinetics, high-dose peptide treatment resulted in marked inhibition of cell proliferation across all tested cell lines. While Cisplatin consistently suppressed cell growth throughout the five-day assay, leading to persistently low cell numbers in treated groups, Tat-SPs appeared to exert their maximal cytotoxic effects early during treatment. Notably, although peptide-treated groups showed significantly reduced cell numbers compared to controls at day 5, surviving AML cells exhibited a capacity for proliferative recovery and resumed aggressive growth following the initial cytotoxic phase. These findings suggest that while Tat-SPs induce substantial early cell death, residual AML cells may retain the ability to proliferate if not completely eradicated.

These findings suggest implications for in vivo efficacy, indicating that Tat-SPs may be most effective as an early intervention in AML treatment. Additionally, the

distinct cytotoxic mechanisms of Tat-SPs and chemotherapeutic agents like Cisplatin highlight their potential for synergy. Combining these treatments could leverage their complementary effects to enhance cancer cell inhibition.

In summary, Tat-SP peptides demonstrated potent cytotoxic activity against AML blast cells. Both peptides significantly reduced cell viability within 24 hours of treatment and effectively inhibited cell proliferation over a five-day period. Notably, the second-generation Tat-SP9 exhibited enhanced cytotoxicity compared to the first-generation Tat-SP4, as evidenced by lower IC_{50} values and the requirement for lower concentrations to achieve comparable antiproliferative effects in AML cell lines. This increased efficacy may be attributed to the optimized stapling position within the Beclin-1-targeting sequence of Tat-SP9. Collectively, these findings underscore the therapeutic potential of Tat-SPs as monotherapy for AML and support further evaluation in preclinical animal models.

4.2 Assessment of addictive cytotoxic effects with chemotherapeutic and targeted Agents

4.2.1 Enhancement of chemotherapy-induced cytotoxicity by Tat-SPs

To investigate potential combinatorial therapeutic strategies for inhibiting cancer cell proliferation, the chemo drugs Doxorubicin and Cytarabine (AraC) were evaluated

for their synergistic effects with Tat-SP peptides in cytotoxicity assays. Doxorubicin, an anthracycline widely employed in cancer therapy, exerts its potent cytotoxic effects primarily through DNA intercalation and inhibition of topoisomerase II, resulting in DNA damage and subsequent induction of apoptosis in rapidly proliferating cancer cells. AraC, a nucleoside analog and a key component of the "7+3" induction regimen for acute myeloid leukemia as previously discussed in Section 1.1.3, induces cell death by interfering with DNA synthesis through inhibiting DNA polymerase, and causing chain termination.

In this study, THP-1 cells were first utilized to evaluate the potential synergistic effects of Tat-SP4 in combination with Doxorubicin or AraC for AML therapy. To determine whether the addition of Tat-SP4 could enhance cytotoxicity beyond that achieved by Doxorubicin alone, THP-1 cells were seeded at a density of 25,000 cells per well in 96-well plates on day 0. Chemotherapeutic agents, either alone or in combination with Tat-SP4 at the indicated concentrations, were administered on the same day. Cell viability was assessed using the trypan blue exclusion method following 48 or 72 hours of incubation. As shown in Figure 4.3A, Doxorubicin treatment resulted in a dose-dependent reduction in THP-1 cell viability after 48 hours. Notably, the addition of Tat-SP4 further potentiated this cytotoxic effect in a dose-dependent manner. Consistent results were observed following 72 hours of co-treatment, as illustrated in Figure 4.3B.

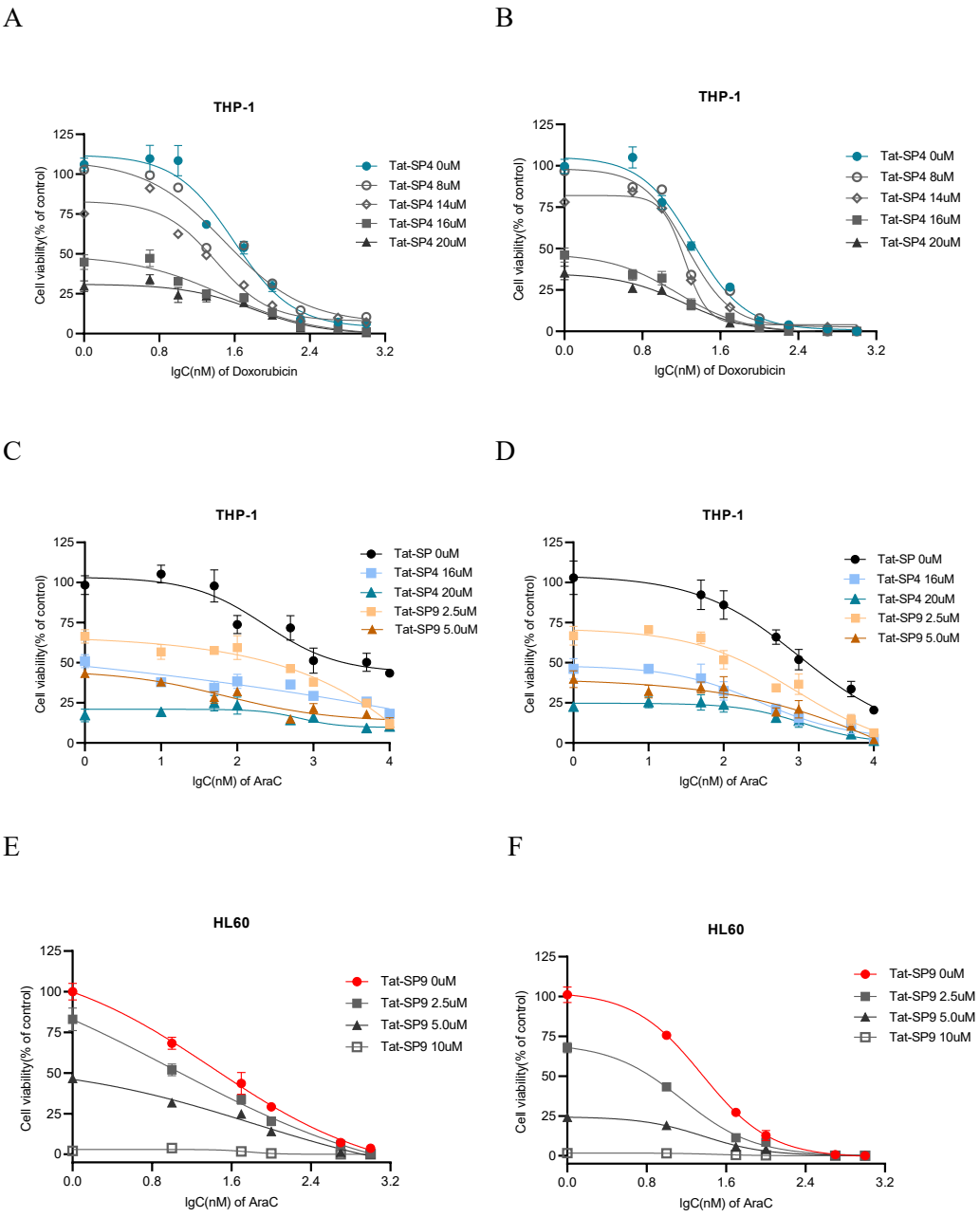

Figure 4.3 Synergistic cytotoxic effects of Tat-SPs with chemo drugs in AML cells.

(A, B) Synergistic cytotoxic effects of Tat-SP4 and Doxorubicin on THP-1 cells for 48 and 72 hours, respectively. (C, D) Synergistic cytotoxic effects of Tat-SP4 or Tat-SP9 and AraC on THP-1 cells for 48 and 72 hours, respectively. (E, F) Synergistic cytotoxic effects of Tat-SP9 and AraC on HL60 cells for 48 and 72 hours, respectively. Cell

viability was assessed using the trypan blue exclusion assay. Data represent mean ± SEM of replicates.

Similar to Doxorubicin, AraC exhibited dose-dependent cytotoxicity in THP-1 cells in 48 and 72 hours tretamnet, as demonstrated in Figures 4.3C and 4.3D. The combination of AraC with Tat-SP4 at concentrations of 16 and 20 μM, or with Tat-SP9 at 2.5 and 5 μM, resulted in enhanced cytotoxic effects during both 48- and 72-hour treatment periods. To further validate these findings, similar experiments were conducted in HL60 cells, which were seeded at 10,000 cells per well on day 0 and treated with AraC alone or in combination with Tat-SP9. Consistent with the results observed in THP-1 cells, the addition of Tat-SP9 at 2.5, 5 and 10 μM further reduced cell viability in the presence of AraC in HL60 cells, as shown in Figures 4.3E and 4.3F. These data collectively indicate that Tat-SP peptides can potentiate the cytotoxic effects of AraC in multiple AML cell lines.

The observed addictive effects between Tat-SP4 and Doxorubicin, as well as between Tat-SP4 or Tat-SP9 and AraC, in AML cell lines highlight the potential of these peptides to enhance the efficacy of standard chemotherapeutic agents. This dose-dependent augmentation of cytotoxicity suggests that Tat-SP peptides may potentiate the anti-leukemic activity of conventional chemotherapy, which forms the cornerstone of AML treatment regimens. The underlying mechanisms may involve modulation of cellular pathways associated with autophagic cell death or mitochondrial dysfunction,

as indicated by previous studies. Importantly, the consistent enhancement of cytotoxicity across multiple AML cell lines underscores the robustness of these synergistic interactions.

4.2.2 Potentiation of targeted therapy efficacy by Tat-SPs

In addition to evaluating conventional chemotherapeutic agents, we examined the potential addictive effects of Tat-SP peptides in combination with Venetoclax, a selective Bcl-2 inhibitor, in Molm13 and THP-1 cell lines.

Molm13 cells were seeded at a density of 10,000 cells per well in 96-well plates on day 0. Venetoclax, either as a single agent or in combination with Tat-SP peptides at specified concentrations, was administered on the same day. After 72 hours of incubation, cell viability was determined using the trypan blue exclusion assay. The results demonstrated that Venetoclax alone inhibited cell viability in a dose-dependent manner. However, the effects of combining Venetoclax with Tat-SP peptides were more complex. At lower concentrations, specifically 3 and 6 μM Tat-SP4, no appreciable increase in cytotoxicity was observed compared to Venetoclax alone, while 9 μM Tat-SP4 resulted in a modest enhancement of cell death, as shown in Figure 4.4A. In contrast, a pronounced increase in Venetoclax-induced cytotoxicity was observed when Tat-SP4 was administered at 12 and 15 μM. A similar trend was observed with Tat-SP9, where additional toxicity was evident only at concentrations of 6.0 and 7.5 μM, as illustrated in Figure 4.4B.

Consistent findings were observed in THP-1 cells, where Venetoclax induced cell death in a concentration-dependent manner. Notably, a significant enhancement of cytotoxicity was detected only when Tat-SP4 was administered at higher concentrations, specifically 16 and 20 μM, whereas lower concentrations did not result in a synergistic effect, as illustrated in Figure 4.4C.

A

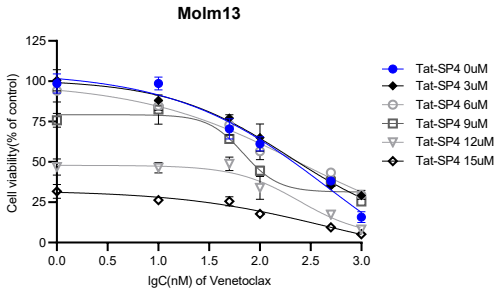

B

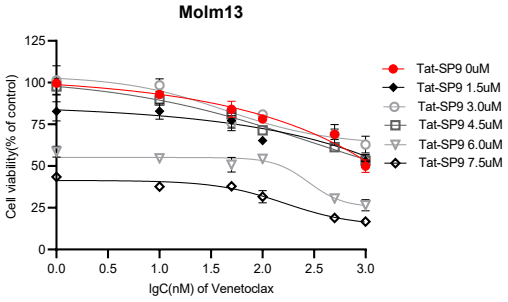

C

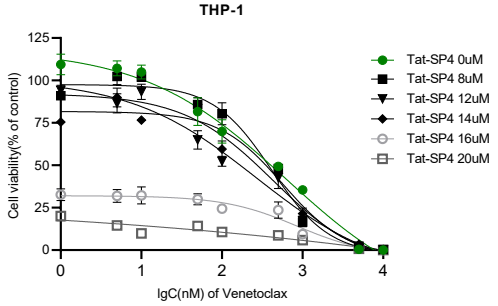

Figure 4.4 Synergistic cytotoxic effects of Tat-SPs with Venetoclax in AML cells. (A, B) Synergistic cytotoxicity of Tat-SP peptides and Venetoclax in Molm13 cells following three days of exposure. (C) Synergistic cytotoxicity of Tat-SP4 and Venetoclax in THP-1 cells following three days of exposure. Cell viability was assessed using the trypan blue exclusion assay at day 3. Data represent mean ± SEM of replicates.

In contrast to conventional chemotherapeutic agents, the synergistic interaction between Tat-SP peptides and Venetoclax demonstrates a concentration-dependent enhancement of cytotoxicity in AML cell lines. The observation that higher concentrations of Tat-SPs are required to achieve better cytotoxicity indicate that effective synergy between Tat-SP peptides and Venetoclax in AML cells may require the use of Tat-SPs at sufficiently high concentrations, underscoring the importance of optimizing peptide dosage in future therapeutic strategies. Although further investigation is warranted to elucidate the molecular mechanisms underlying this synergistic interaction and to assess the efficacy of these combinations in preclinical models, the present findings support the potential of Tat-SPs as promising adjuvant agents in combination with either targeted therapies or conventional chemotherapy for the treatment of AML.

4.2.3 Inhibition of colony formation by Tat-SPs and combination treatments

The additive cytotoxicity of Tat-SP peptides in combination with chemotherapeutic agents or targeted therapeutics were further evaluated using the colony formation assay. This assay assesses the ability of individual cells to proliferate and form colonies, thereby providing a measure of clonogenic potential, tumorigenicity, and cellular response to treatment. To accurately model the growth conditions of AML suspension cells, a semi-solid culture system was employed. Specifically, a base layer

of culture medium containing 0.6% agar was prepared, and HL60 cells were seeded in an upper layer containing 0.3% agar to prevent cell attachment to the dish and facilitate colony formation. In this study, 800 HL60 cells were plated per well in a 6-well plate and incubated in agar-based media for 14 days to allow colony development. At the conclusion of the incubation period, colonies were stained using nitroblue tetrazolium (NBT), and images were captured with the ChemiDoc™ Imaging System for subsequent analysis.

As shown in Figure 4.5, HL60 cells in the control group exhibited extensive colony formation, indicative of robust clonogenic potential. Treatment with 1 nM AraC or Venetoclax resulted in a marked reduction in colony size; however, the total number of colonies remained less unaffected. In contrast, Tat-SP4 alone significantly decreased the number of HL60 colonies in a dose-dependent manner, with 20 μM demonstrating a more pronounced inhibitory effect than 14 μM. Notably, the combination of Tat-SP4 with AraC further suppressed colony formation, while co-treatment with Tat-SP4 and Venetoclax nearly eradicated HL60 colonies. These findings are consistent with the results of cell viability assays and collectively demonstrate a synergistic interaction between Tat-SP4 and both chemotherapeutic and targeted agents. The distinct effects observed—where AraC and Venetoclax primarily limited colony growth, but Tat-SP4 reduced overall colony numbers—suggest that Tat-SP4 may impair the proliferative capacity in a complementary action to AraC and Venetoclax.

A

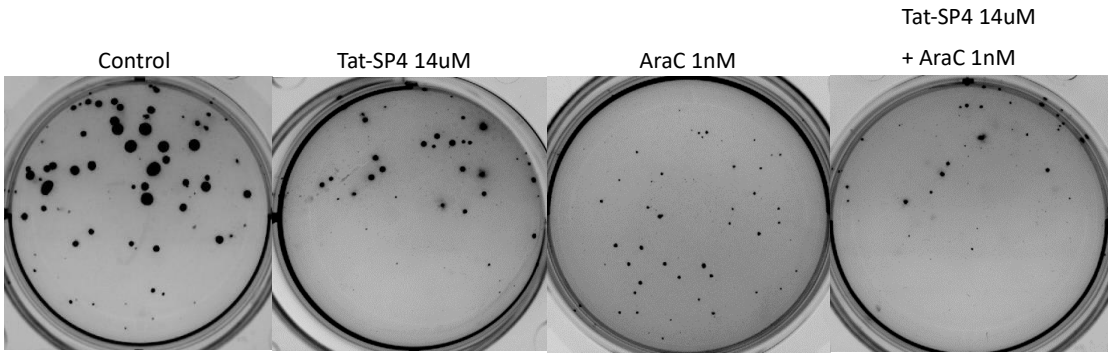

B

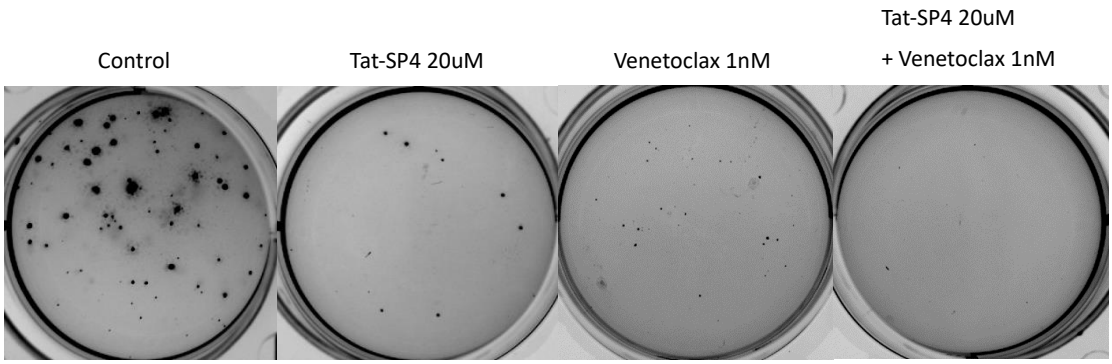

Figure 4.5 Colony formation of Tat-SPs with AraC or Venetoclax in AML cells. (A) Synergistic analysis of colony formation in HL60 cells treated with Tat-SP4 and AraC. (B) Synergistic analysis of colony formation in HL60 cells treated with Tat-SP4 and Venetoclax. For each condition, 800 HL60 cells were seeded in agar-containing semi-solid media and subjected to the indicated treatments. After 14 days of incubation, colonies were washed with PBS, stained with nitroblue tetrazolium (NBT), and imaged using the ChemiDoc™ Imaging System.

However, a notable low concentration of AraC and Venetoclax, at only 1 nM, significantly inhibited HL60 colony formation. This pronounced effect may be

attributed to the low seeding density, with only 800 cells initially plated in agar medium. Although synergistic effects with Tat-SP4 were observed, the changes were subtle, as monotherapy with AraC, Venetoclax, or Tat-SP4 also markedly reduced HL60 colony numbers. This suggests that assay optimization is needed, particularly in dose selection and treatment regimen design, to better delineate synergistic interactions and enhance the robustness of the findings.

Collectively, while Tat-SPs demonstrated strong cytotoxicity primarily against AML blasts, their potential synergistic effects can also be achieved when combined with first-line chemotherapeutic agents or targeted therapies such as Bcl-2 inhibitors. Although the mechanisms underlying the synergy between Tat-SPs and AraC or Venetoclax require further investigation, the demonstrated synergistic applications hold potential for reducing the toxicity of chemotherapeutic drugs and mitigating drug resistance in targeted therapies.

4.3 Investigation of subcellular localization of Tat-SPs in AML cells using rhodamine labeling and fluorescent imaging

The potent cytotoxic effects of Tat-SP peptides prompted further investigation into their subcellular localization to elucidate potential mechanisms of action. To visualize peptide distribution within cells, we utilized Rhod-SP4, a fluorescently labeled analog of Tat-SP4 conjugated with a rhodamine moiety. Additionally, previous experiments revealed that the MTT assay failed to detect Tat-SP-induced cell death, leading us to

hypothesize that Tat-SP peptides may interfere with mitochondrial function. Given that the MTT assay depends on mitochondrial enzymes—primarily succinate dehydrogenase, a key component of the electron transport chain—this observation suggests that Tat-SP-induced mitochondrial damage may compromise the assay's ability to accurately assess cytotoxicity. Thus, investigating the subcellular localization of Tat-SP peptides may provide critical insights into their impact on mitochondrial integrity and function.

Confocal microscopy was employed in live AML cells using dual staining with Rhod-SP4 and MitoTracker Green to investigate the subcellular localization of Tat-SP peptides. HL60, Molm13, THP-1, and Kasumi-1 cells were seeded at a density of one million cells per well in 1mL of culture medium, with poly-D-lysine coating applied to facilitate cell attachment prior to seeding. Staining was performed 15 minutes before imaging to ensure optimal visualization. As shown in Figure 4.6, Rhod-SP4 demonstrated strong co-localization with mitochondria, as evidenced by the overlap with MitoTracker Green fluorescence, across all four AML cell lines examined. These findings indicate that the stapled peptides preferentially target and accumulate within mitochondria in AML cells.

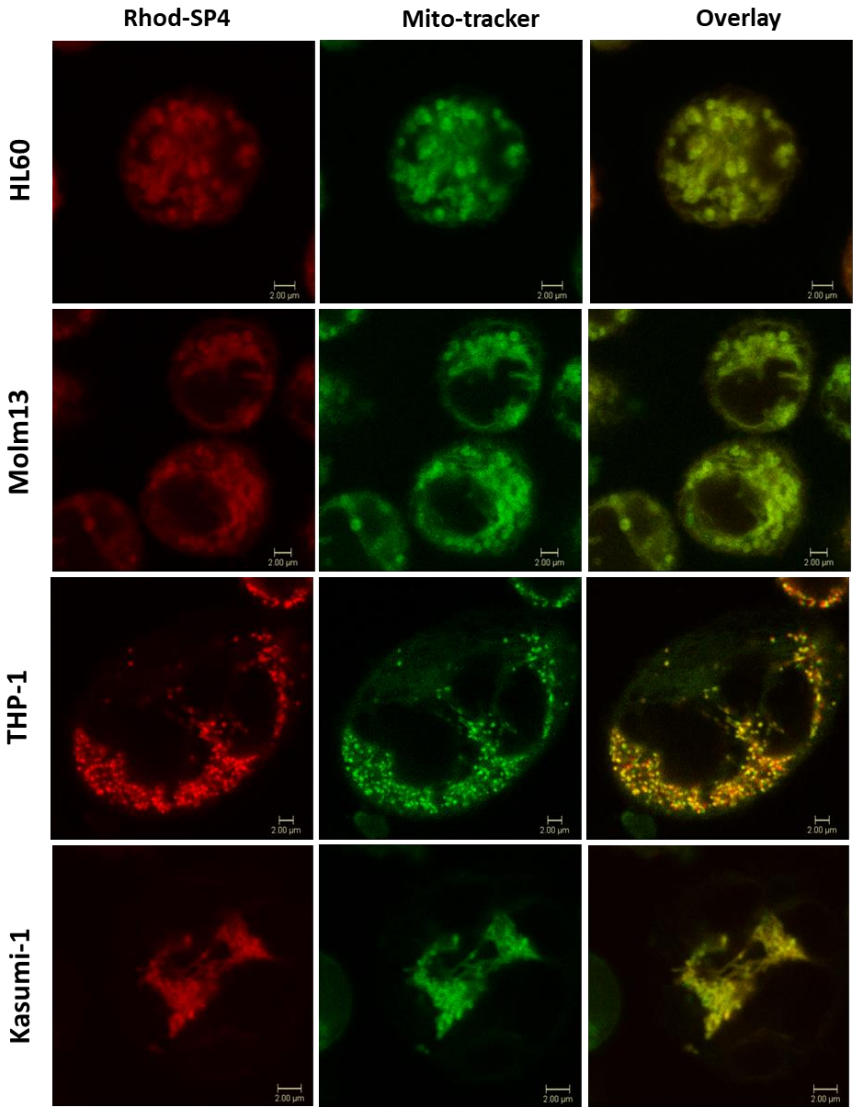

Figure 4.6 Colocalization of Rhod-SP4 and mitochondria in live AML cells. Live AML cells were seeded onto poly-D-lysine-coated confocal culture dishes and simultaneously stained with Rhod-SP4 (red) and MitoTracker Green (green) for 15 minutes prior to imaging. Fluorescence images were acquired using confocal microscopy. Scale bar: 2 μm.

Although the precise mechanism underlying the observed co-localization of Rhod-SP4 with mitochondria remains to be elucidated, these findings warrant further

investigation into the impact of Tat-SP peptides on mitochondrial function, given the organelle's central role in cellular homeostasis. Moreover, as the structure of Rhod-SP4 differs slightly from that of Tat-SP4, future studies may employ radiolabeling approaches to more accurately track the intracellular dynamics and distribution of Tat-SP peptides.

4.4 Impact of Tat-SPs on mitochondrial function in AML cells

The observation that Rhod-SP4 co-localizes with mitochondria is particularly significant, given the central role of mitochondria in maintaining cellular homeostasis and their specific influence on the biology of AML blasts, as discussed in Section 1.1.3. This finding prompts the hypothesis that Tat-SP peptides may impact mitochondrial function. To explore this possibility, a series of investigations were undertaken to assess key aspects of mitochondrial physiology, including mitochondrial membrane potential, cellular reactive oxygen species (ROS) levels, mitochondrial permeability transition pore (MPTP) activation, and oxidative phosphorylation (OXPHOS) activity. These analyses aim to elucidate the potential mechanisms by which Tat-SP peptides exert their cytotoxic effects in AML cells.

4.4.1 Induction of mitochondrial membrane potential dissipation

In healthy mitochondria, the membrane potential is sustained by the integrity of

the organelle's double-membrane structure. The mitochondrial matrix maintains a negative charge, which facilitates the accumulation of cationic ions and the export of anions, processes essential for normal physiological function. Tetramethylrhodamine methyl ester (TMRM) is a cell-permeant, cationic fluorescent dye that selectively accumulates within the intact mitochondria of living cells, thereby serving as a reliable indicator of mitochondrial membrane potential. Disruptors of mitochondrial potential, such as carbonyl cyanide 3-chlorophenylhydrazone (CCCP), function as protonophores, dissipating the membrane potential and compromising mitochondrial structural integrity, as illustrated in Figure 4.7A.

To assess whether Tat-SP peptides disrupt mitochondrial membrane depolarization, HL60 and THP-1 cells were seeded at a density of 500,000 cells per well in 12-well plates and treated with either 15 μM or 25 μM Tat-SP4 for 1 hour. Following treatment, cells were stained with TMRM for 30min and analyzed by flow cytometry to quantify changes in mitochondrial membrane potential. CCCP was included as a positive control for mitochondrial depolarization.

A

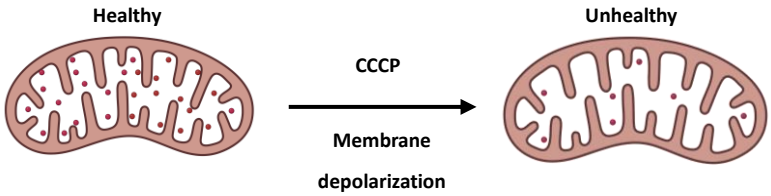

B

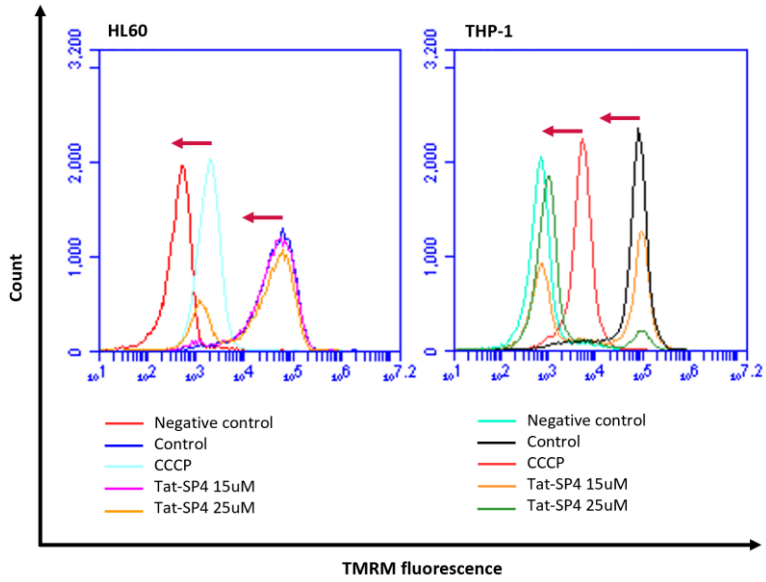

Figure 4.7 Loss of mitochondrial membrane potential induced by Tat-SP4. (A) Schematic overview of the experimental approach for assessing mitochondrial membrane potential loss using TMRM fluorescence. (B) Flow cytometry plots of HL60 and THP-1 cells treated with the indicated concentrations of Tat-SP4. Following treatment, cells were stained with TMRM for 30 minutes and analyzed by flow cytometry. Red arrows indicate the reduction of TMRM fluorescence signal induced by mitochondrial membrane potential disruptors.

After a 1-hour treatment with Tat-SP4 in HL60 cells, a decrease in the TMRM signal was observed in the 25 μM group but not in the 15 μM group. Similar to the effect of CCCP, a decreased peak appeared at the same position as that of CCCP. However, unlike the single-peak shift induced by CCCP, the TMRM signal displayed a double-peak pattern, suggesting that Tat-SP4 induces mitochondrial membrane potential loss through a mechanism distinct from CCCP. A similar double-peak pattern was observed in THP-1 cells. Compared to HL60 cells, THP-1 cells demonstrated increased sensitivity to Tat-SP4, as evidenced by pronounced mitochondrial membrane depolarization at both 15 μM and 25 μM concentrations. This was reflected by a reduction in the high-TMRM-intensity peak and a concomitant increase in the low-TMRM-intensity peak. Notably, in THP-1 cells, the depolarized TMRM signal shifted beyond that observed with CCCP treatment, closely aligning with the fluorescence profile of unstained cells, as illustrated in Figure 4.7B. These results suggest that Tat-SP4 induces a more profound loss of mitochondrial membrane potential in THP-1 cells relative to HL60 cells.

To assess the effect of treatment duration on mitochondrial membrane potential, HL60 cells were exposed to Tat-SP9 for 30, 60, and 120 minutes, followed by analysis of TMRM fluorescence. As shown in Figure 4.8A, no significant differences in TMRM fluorescence intensity were observed among the three time points, suggesting that the loss of mitochondrial membrane potential induced by Tat-SP9 is not time-dependent

within this timeframe, but is instead primarily determined by the peptide concentration. Increasing concentrations of Tat-SP9 led to a marked shift in the TMRM fluorescence distribution, with a greater proportion of cells exhibiting low TMRM fluorescence intensity and a corresponding reduction in the high-intensity population. Notably, the low-TMRM-intensity peak observed in Tat-SP9-treated HL60 cells closely overlapped with the peak position induced by CCCP.

A

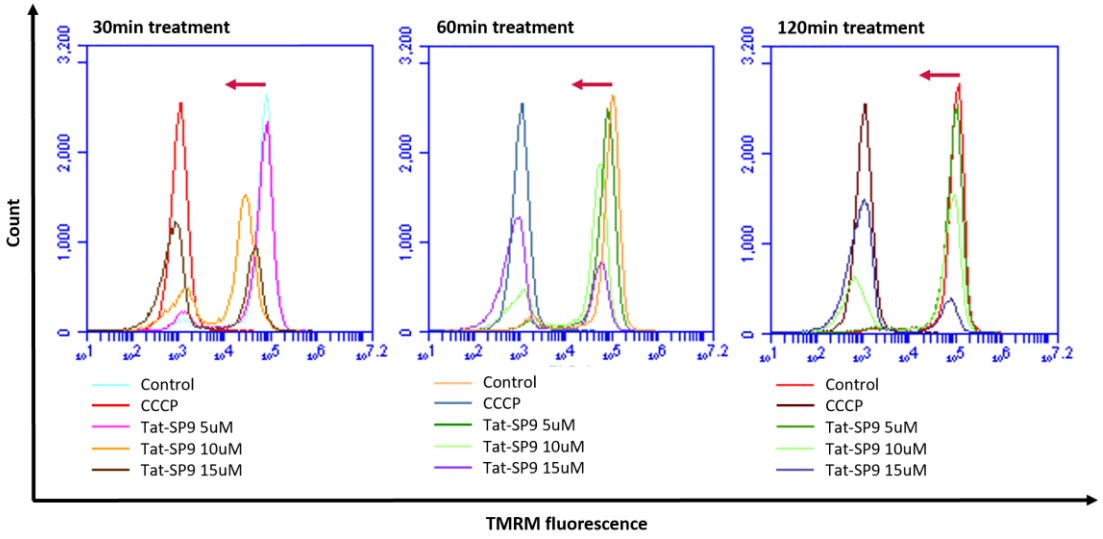

B

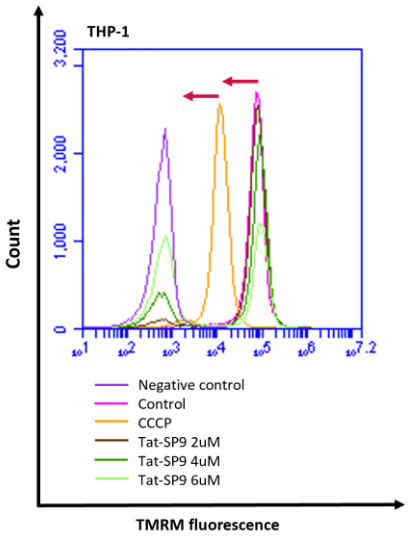

Figure 4.8 Loss of mitochondrial membrane potential induced by Tat-SP9. (A) Flow cytometry plots of HL60 cells treated with the Tat-SP9 for different treatment duration. (B) Flow cytometry plots of THP-1 cells treated with the indicated concentrations of Tat-SP9. Cells were stained with TMRM for 30 minutes prior analyzed by flow cytometry. Red arrows indicate the reduction of TMRM fluorescence

signal induced by mitochondrial membrane potential disruptors.

In THP-1 cells treated with Tat-SP9 for 60 minutes, a comparable shift in TMRM fluorescence intensity was observed, as shown in Figure 4.8B. At a concentration of 2 μM Tat-SP9, only minor alterations were detected, with a slight increase in the low-TMRM-intensity peak and a corresponding decrease in the high-TMRM-intensity peak. These effects became more pronounced at 4 μM and were markedly evident at 6 μM, indicating a concentration-dependent response. Notably, in contrast to HL60 cells, the low-TMRM-intensity peak in Tat-SP9-treated THP-1 cells overlapped with the fluorescence profile of the unstained control group, mirroring the pattern observed with Tat-SP4 treatment in THP-1 cells. This suggests a more profound loss of mitochondrial membrane potential in THP-1 cells upon exposure to Tat-SP peptides.

Collectively, these findings demonstrate that Tat-SP peptides induce a dose-dependent, rather than time-dependent, disruption of mitochondrial membrane potential, resulting in the emergence of two distinct cell populations characterized by high and low TMRM fluorescence intensity. This effect is likely mediated by specific interactions of Tat-SPs with mitochondrial proteins or lipids, ultimately compromising mitochondrial integrity. Notably, the depolarizing effects of Tat-SPs differ from those of CCCP, underscoring the possibility of a unique mechanism of action and highlighting the necessity for further investigation into the precise molecular targets of Tat-SPs and their broader impact on mitochondrial function. Additionally, a clear cell line-

dependent sensitivity was observed, with THP-1 cells exhibiting mitochondrial membrane depolarization at lower Tat-SP concentrations and displaying more pronounced shifts in TMRM fluorescence compared to HL60 cells. While baseline TMRM staining did not reveal intrinsic differences in membrane potential between the two cell lines, these results suggest that other mitochondrial characteristics may underlie the differential responses, warranting further exploration of cell line-specific mitochondrial vulnerabilities to Tat-SP-induced dysfunction.

4.4.2 Activation of the mitochondrial permeability transition pore

To further investigate mitochondrial structural integrity, activation of the mitochondrial permeability transition pore was assessed using Calcein fluorescence. MPTP opening is a critical event in cell death pathways, as it leads to mitochondrial swelling, loss of membrane selectivity, and the release of pro-apoptotic factors such as cytochrome c, ultimately resulting in apoptotic or necrotic cell death. Calcium overload is a well-established trigger for MPTP activation. In this study, Calcein acetoxymethyl ester (Calcein AM), a cell-permeant dye, was employed to monitor MPTP status. Upon entry into viable cells, Calcein AM is hydrolyzed by intracellular esterases to yield fluorescent Calcein. To specifically assess mitochondrial Calcein retention, cobalt chloride—a fluorescence quencher impermeable to intact mitochondrial membranes—was added to selectively quench cytosolic Calcein fluorescence, thereby allowing the detection of mitochondrial-localized Calcein. Ionomycin, a calcium ionophore, was

utilized as a positive control to induce MPTP opening. An overview of the experimental approach is illustrated in Figure 4.9A (diagram adapted from https://www.yajimall.com/product/detail/12725.html).

A

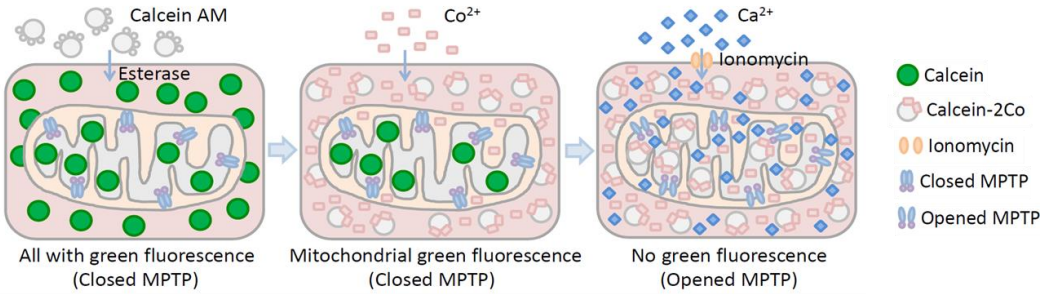

B

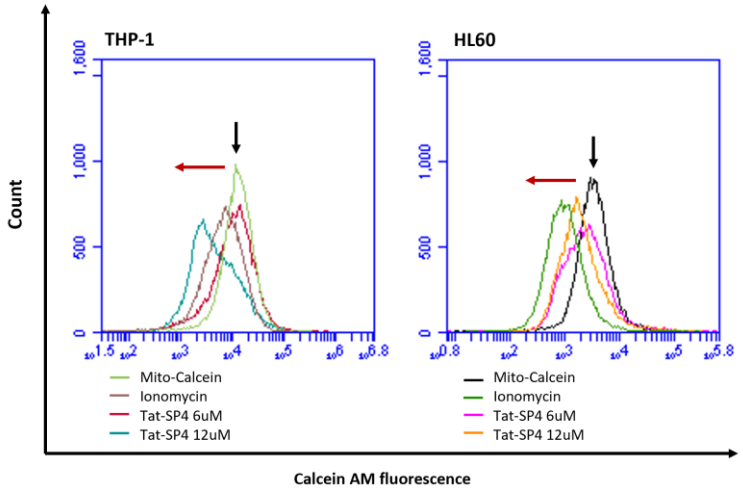

C

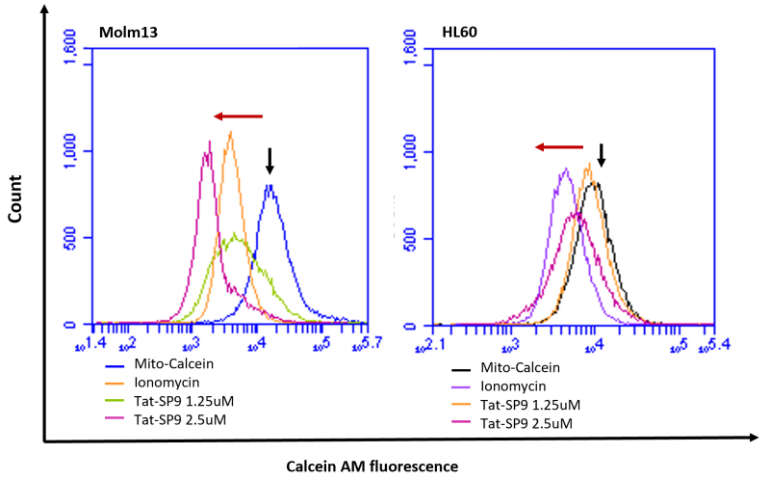

Figure 4.9 MPTP activation by Tat-SPs. (A) Schematic representation of MPTP activation by ionomycin. Diagram adapted from YaJi Biological

(https://www.yajimall.com/product/detail/12725.html). (B) Flow cytometry analysis of MPTP opening in THP-1 and HL60 cells following treatment with Tat-SP4. (C) Flow cytometry analysis of MPTP opening in Molm13 and HL60 cells following treatment with Tat-SP9. In all panels, black arrows indicate the mito-Calcein fluorescence signal, while red arrows denote the reduction in fluorescence intensity induced by MPTP activators.

HL60, THP-1, and Molm13 cells were seeded in 12-well culture plates at a density of 5×10^5 cells/mL per well, using serum-free culture medium to minimize interference with fluorescence signals. Cells were incubated with Calcein AM, $CoCl_2$, and the indicated treatments of ionomycin or peptides for 1 hour. Following incubation, cells were washed and resuspended in PBS prior to flow cytometric analysis.

As shown in Figure 4.9B, Tat-SP4 induced MPTP opening in both THP-1 and HL60 cells in a dose-dependent manner, with effects comparable to those observed following treatment with 250 nM ionomycin. Notably, 250 nM ionomycin elicited a greater degree of mitochondrial disruption in HL60 cells compared to THP-1 cells, as indicated by a more pronounced decrease in fluorescence intensity. For Tat-SP4, a concentration of 6 μM resulted in a moderate reduction in mito-Calcein fluorescence, while 12 μM induced substantial signal loss in both cell lines. A similar pattern was observed with Tat-SP9, as depicted in Figure 4.9C, although at considerably lower concentrations. Specifically, 1.25 μM Tat-SP9 caused a mild decrease in mito-Calcein

fluorescence in HL-60 cells, whereas 2.5 μM led to a more pronounced induction of MPTP opening. This effect was even more evident in Molm13 cells, where dramatic reductions in mito-Calcein fluorescence were observed at both 1.25 μM and 2.5 μM Tat-SP9, indicating heightened sensitivity to Tat-SP9-induced mitochondrial dysfunction.

Although the shift in Calcein fluorescence observed in this assay is less pronounced than the changes detected in the mitochondrial membrane potential assay, it is significant that low concentrations of Tat-SP peptides are sufficient to induce MPTP activation in both HL60 and THP-1 cells. Notably, in the Tat-SP4 treatment group, concentrations as low as 12 μM resulted in a marked loss of mitochondrial Calcein fluorescence, indicating MPTP opening and compromised mitochondrial integrity prior to the onset of widespread cell death. This finding is particularly noteworthy given that the IC_{50} values for these cell lines are higher, approximately 20 μM, suggesting that mitochondrial dysfunction precedes overt cytotoxicity.

Consistent with previous findings, mitochondrial susceptibility to Tat-SP-induced dysfunction is cell line-dependent, as evidenced by the greater reduction in mito-Calcein fluorescence observed in Molm13 cells compared to HL-60 cells at equivalent concentrations of Tat-SP9, in Figure 4.9C. This increased sensitivity in Molm13 cells aligns with their lower IC_{50} value (approximately 4.3 μM) relative to HL-60 cells (approximately 10 μM) following Tat-SP9 exposure. However, it is important to

acknowledge potential technical limitations of the Calcein-based assay; at higher peptide concentrations, the formation of intracellular Calcein conjugates observed by microscopy may compromise the accuracy of flow cytometric detection. Despite these challenges, the data support that Tat-SPs induce MPTP opening at concentrations as low as 6 or 12 μM for Tat-SP4 and no more than 2.5 μM for Tat-SP9. To enhance the sensitivity and reliability of MPTP activation detection, the implementation of alternative or complementary protocols may be warranted.

4.4.3 Elevation of cellular reactive oxygen species by Tat-SPs

Mitochondrial dysfunction is a central contributor to various forms of cellular damage. One significant consequence of MPTP activation is the elevation of intracellular reactive oxygen species (ROS) levels. Disruption of mitochondrial membrane permeability and the consequent loss of the electrochemical gradient essential for maintaining membrane potential impair the efficiency of oxidative phosphorylation, thereby promoting excessive ROS production. Elevated ROS, in turn, can inflict widespread cellular damage by reacting with critical biomolecules, including DNA, RNA, proteins, and lipids, ultimately compromising their structural integrity and biological function.

ROS levels were quantified using the CellROX fluorescent dye. Following peptide treatment, HL60 and THP-1 cells were harvested, stained with CellROX, and analyzed

by flow cytometry. As illustrated in Figure 4.10, Tat-SPs treatment resulted in a marked elevation of ROS levels in both cell lines. Specifically, exposure to 20 μM Tat-SP4 induced a substantial increase in ROS production, as evidenced by a rightward shift in CellROX fluorescence intensity. This effect was further amplified at 40 μM Tat-SP4, with ROS levels approaching those observed in the positive control group treated with tert-butyl hydroperoxide (TBHP), a well-established inducer of cellular ROS, as shown in Figure 4.10A. Comparable results were obtained with Tat-SP9 in Figure 4.10B: in THP-1 cells, 5 μM Tat-SP9 elicited a detectable increase in ROS, which became more pronounced at 10 μM. In HL-60 cells, a mild increase in ROS was observed at 7.5 μM Tat-SP9, while a significant elevation was detected at 15 μM. These findings collectively indicate that Tat-SP peptides induce robust, concentration-dependent ROS generation in AML cell lines.

A

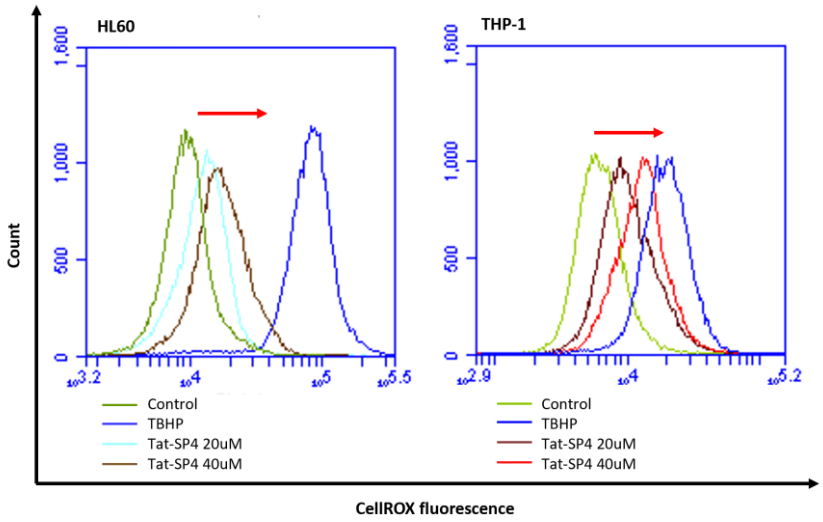

B

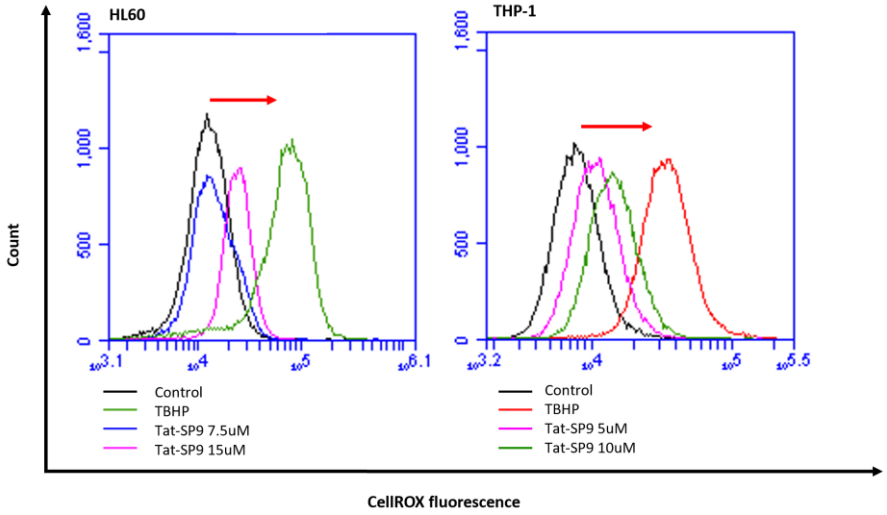

Figure 4.10 Cellular ROS level increasement induced by Tat-SPs. (A) Flow cytometry analysis of ROS production in HL-60 and THP-1 cells following treatment with Tat-SP4. (B) Flow cytometry analysis of ROS production in HL-60 and THP-1 cells following treatment with Tat-SP9. In both panels, red arrows indicate the rightward shift in fluorescence intensity corresponding to increased ROS levels upon peptide treatment.

Consistent with the observed loss of mitochondrial membrane potential, additional hallmarks of mitochondrial dysfunction—most notably, elevated cellular ROS levels—were detected in AML blasts from both HL60 and THP-1 cell lines. These findings corroborate the occurrence of MPTP opening and the resultant widespread cellular damage. ROS induction by both Tat-SP4 and Tat-SP9 was dose-dependent, with Tat-SP4 eliciting more pronounced ROS production at higher concentrations compared to Tat-SP9. This trend is in agreement with their respective IC_{50} values: 20 μM Tat-SP4 resulted in approximately 50% cell death, while 40 μM reduced cell viability by about 80%. Furthermore, HL60 cells exhibited a lower degree of ROS induction than THP-1 cells at lower Tat-SP9 concentrations, consistent with previous observations of differential mitochondrial susceptibility between these cell lines.

4.4.4 Impairment of oxidative phosphorylation

Given the observed disruptive effects of Tat-SP peptides on mitochondrial function in AML blast cells, we further investigated whether Tat-SPs impair oxidative phosphorylation (OXPHOS) in these cancer cells. Mitochondria are essential for cellular bioenergetics, primarily through their role in OXPHOS, which generates the majority of cellular ATP. Impairment of mitochondrial function can lead to a deficit in energy production, thereby compromising cellular viability and potentially contributing to cancer cell death.

To evaluate the impact of Tat-SPs on oxidative phosphorylation (OXPHOS), we

measured the oxygen consumption rate (OCR) in AML cell lines using mitochondrial respiratory chain complex inhibitors. This approach enables the delineation of specific OXPHOS parameters affected by Tat-SPs treatment, including basal respiration, ATP-linked respiration, maximal respiratory capacity, and spare respiratory capacity. By sequentially administering inhibitors targeting complexes I through IV of the electron transport chain and employing a sensor system to monitor real-time changes in oxygen consumption and extracellular acidification, we systematically assessed alterations in mitochondrial function following Tat-SP peptides exposure. A schematic overview of the assay workflow and the inhibitors utilized is presented in Figure 4.11 (diagram adapted from Agilent Technologies, Inc.; https://www.agilent.com/en/product/cell-analysis/real-time-cell-metabolic-analysis/xf-assay-kits-reagents-cell-assay-media/seahorse-xf-cell-mito-stress-test-kit-740885).

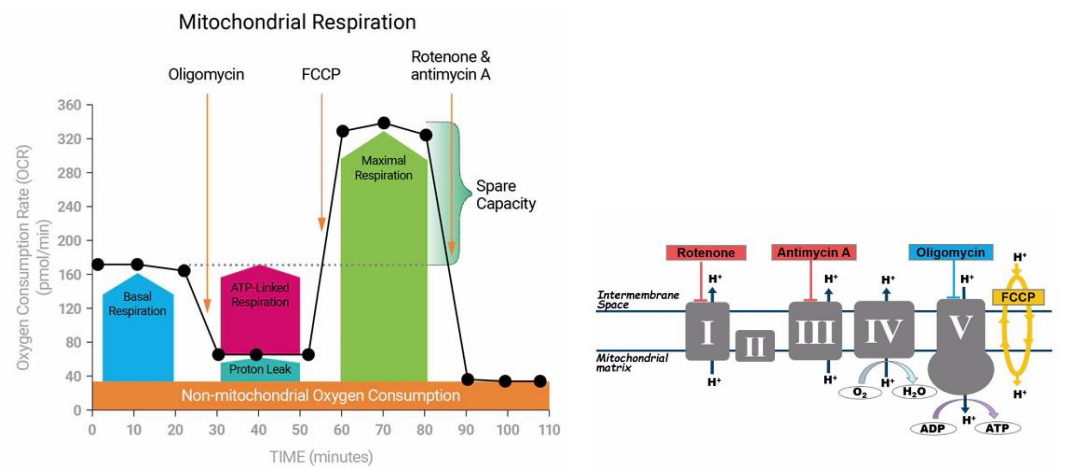

Figure 4.11 The schematic diagram of OXPHOS analysis. Diagram adapted from Agilent Technologies, Inc.

MV-4-11, THP-1, and Molm13 cells were seeded at a density of approximately 200,000 to 250,000 cells per well in 0.5 mL of assay buffer using Seahorse assay cell plates. Prior to seeding, wells were coated with poly-D-lysine to facilitate AML cell adherence. Inhibitors targeting specific complexes of the electron transport chain, as well as Tat-SP peptides, were loaded into the Seahorse sensor plate according to the manufacturer's protocol. Upon completion of the assay, cell viability and number were determined using trypan blue exclusion, and all OCR data were normalized to cell number.

As shown in Figure 4.12A, MV-4-11 cells treated with Tat-SP4 exhibited a significant, dose-dependent reduction in both basal and maximal respiration, with 32 μM Tat-SP4 producing a more pronounced inhibitory effect than 16 μM. Comparable inhibitory effects on mitochondrial respiration were observed in THP-1 and Molm13 cell lines, in Figures 4.12B and 4.12C. Specifically, in THP-1 cells, treatment with 30 μM Tat-SP4 resulted in a marked decrease in basal OCR, further supporting the suppressive impact of Tat-SP4 on mitochondrial function across multiple AML cell lines.

A

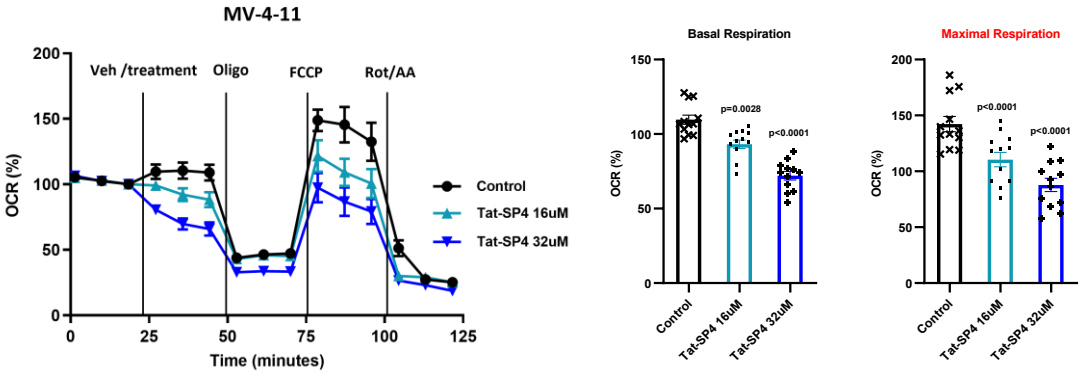

B

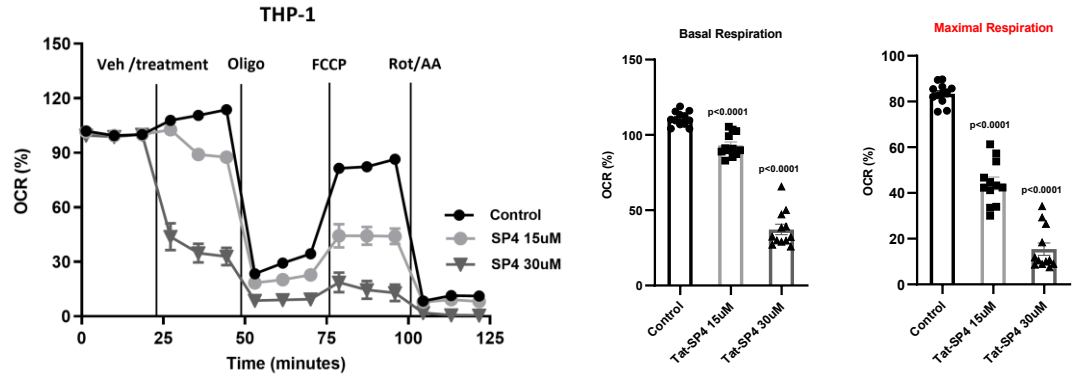

C

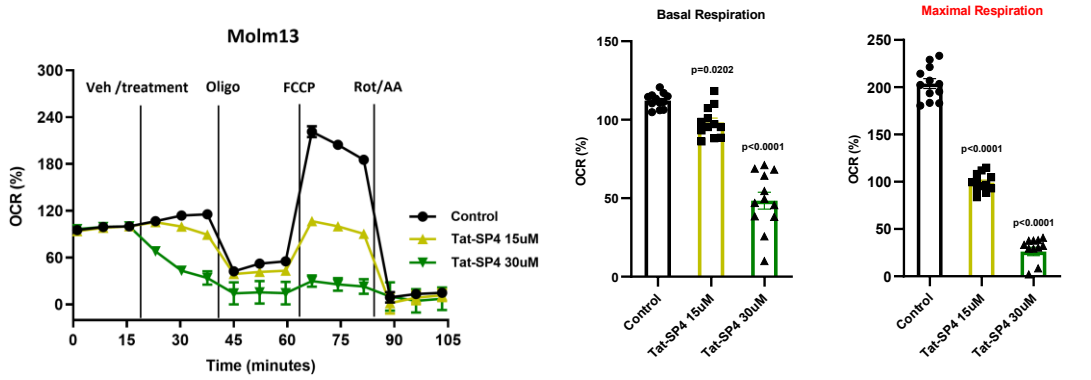

Figure 4.12 OXPHOS inhibition by Tat-SP4. (A) OCR profiles of MV-4-11 cells following treatment with Tat-SP4. (B) OCR profiles of THP-1 cells following treatment with Tat-SP4. (C) OCR profiles of Molm13 cells following treatment with Tat-SP4. OCR was measured using the Agilent Seahorse Analyzer, and values were normalized to cell number. Data are presented as mean ± SEM of replicate measurements. Statistical significance was determined by two-way ANOVA.

OCR analysis was similarly conducted to assess the effects of Tat-SP9 on mitochondrial respiration in MV-4-11, THP-1, and Molm13 cell lines. As shown in Figure 4.13, Tat-SP9 treatment resulted in dose-dependent suppression of OXPHOS, with pronounced inhibition of maximal respiratory capacity in both MV-4-11 and Molm13 cells, paralleling the effects observed with Tat-SP4. In contrast, treatment of THP-1 cells with 2.5 μM Tat-SP9 did not result in a significant reduction in OXPHOS activity. In Molm13 cells, while 2.5 μM Tat-SP9 had minimal impact on basal OCR, it nonetheless significantly inhibited maximal respiration.

A

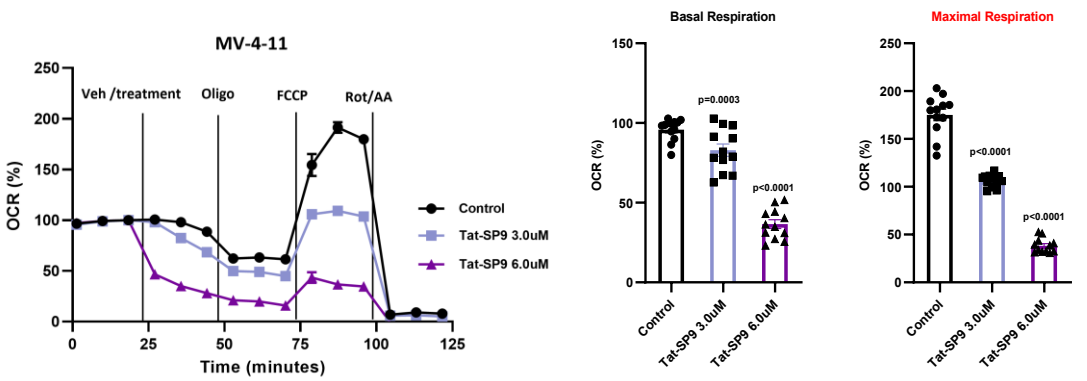

B

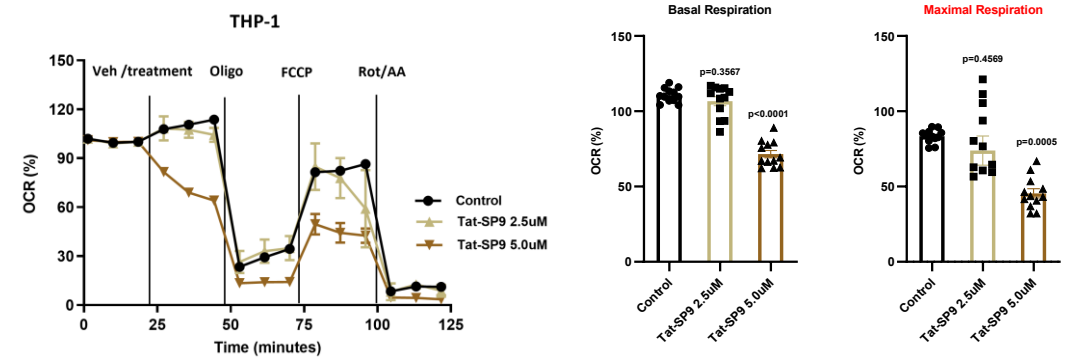

C

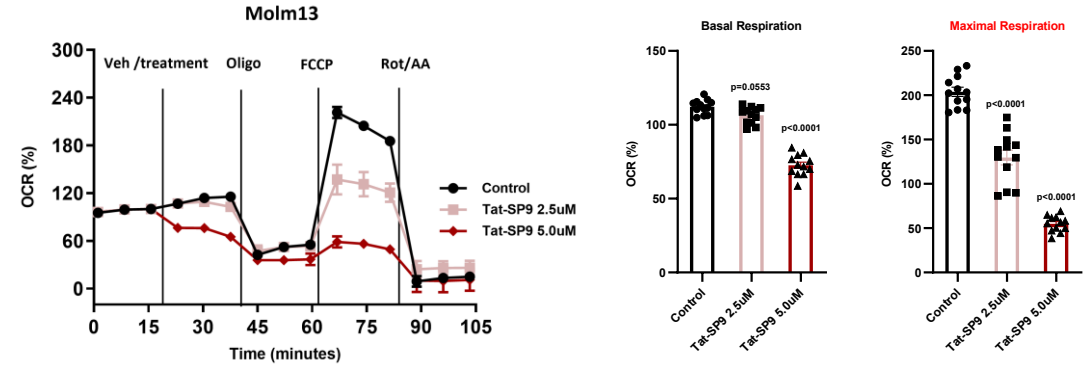

Figure 4.13 OXPHOS inhibition by Tat-SP9. (A) OCR profiles of MV-4-11 cells following treatment with Tat-SP9. (B) OCR profiles of THP-1 cells following treatment with Tat-SP9. (C) OCR profiles of Molm13 cells following treatment with Tat-SP9. OCR was measured using the Agilent Seahorse Analyzer, and values were normalized to cell number. Data are presented as mean ± SEM of replicate measurements.

Statistical significance was determined by two-way ANOVA.

Notably, an unexpected irregularity was observed in the maximal respiratory rates of THP-1 cells: the maximal OCR, including that of the control groups, was consistently lower than the basal OCR. Theoretically, the addition of FCCP, an uncoupling agent, should dissipate the proton gradient across the inner mitochondrial membrane, thereby eliciting the highest possible OCR. Despite optimization of FCCP concentrations, reliable measurement of maximal OCR in THP-1 cells could not be achieved. This anomaly may be attributable to suboptimal cell conditions or insufficient seeding density, indicating that further optimization of experimental parameters is necessary to resolve these issues.

Our findings demonstrate that Tat-SP peptides potently disrupt OXPHOS activity in AML cells, leading to significant impairment of mitochondrial function. Importantly, Tat-SPs markedly suppress maximal respiratory capacity, a critical determinant of cancer cell survival under metabolic stress conditions such as nutrient deprivation, which frequently occur during uncontrolled proliferation. Furthermore, high concentrations of Tat-SPs also inhibited basal respiration in AML cells, providing additional evidence for the ablation of OXPHOS activity. Taken together, these results indicate that Tat-SPs induce profound mitochondrial dysfunction upon entry into AML cells, ultimately resulting in mitochondrial failure and cell death.

4.5 Summary

AML cell lines exhibited differential sensitivities to Tat-SP-induced antiproliferative effects. HL60, THP-1, and Molm13 cells were notably more sensitive to Tat-SP4, with IC_{50} values ranging from 20.2 to 25.7 μM, whereas MV-4-11, OCI-AML3, and Kasumi-1 cells displayed reduced sensitivity, with IC_{50} values between 40 and 65.4 μM. These antiproliferative effects were consistently observed following both overnight and 5 days treatment regimens, underscoring the potential of Tat-SP peptides as a robust therapeutic strategy for AML. The second-generation peptide, Tat-SP9, which incorporates optimized stapling positions, demonstrated enhanced cytotoxicity, reducing IC_{50} values to ≤10 μM in sensitive cell lines and to 18.2–25.5 μM in previously resistant cell lines. The observed variability in sensitivity among AML cell lines to Tat-SP treatment suggests that intrinsic signaling pathways or microenvironmental factors may influence therapeutic response, that underscore the importance for optimizing and tailoring Tat-SP-based therapies to specific AML subtypes.

In line with the observed dose-dependent cytotoxicity, Tat-SPs were found to induce significant mitochondrial damage, which likely contributes substantially to cell death in AML blasts. Mechanistically, Tat-SPs disrupted mitochondrial function in a dose-dependent manner by abolishing mitochondrial membrane potential, promoting MPTP opening, elevating cellular ROS levels, and inhibiting OXPHOS. Collectively, these effects impose a substantial metabolic burden on AML cells. Notably, given that

four of the eleven FDA-approved therapies for AML in the past decade target mitochondrial pathways, our findings further highlight the therapeutic potential of Tat-SPs.

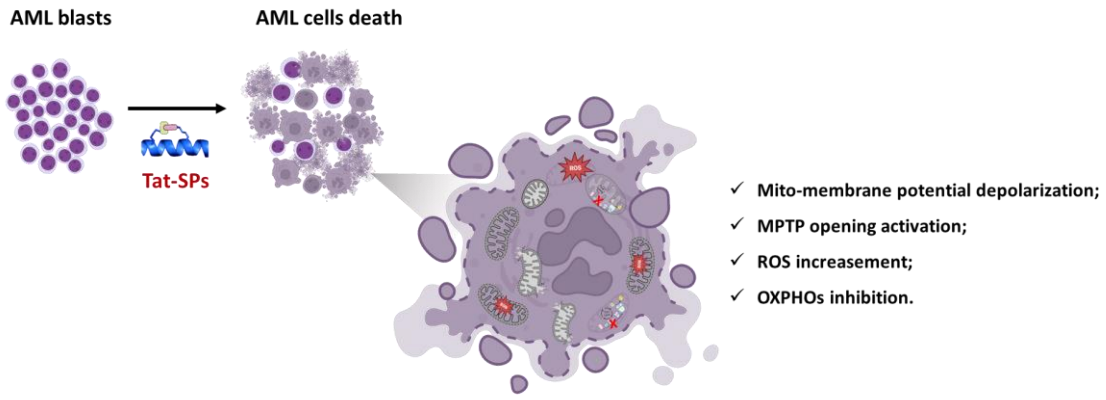

Figure 4.14 Tat-SPs induce cytotoxicity and mitochondrial dysfunction in AML cells.

Beyond their efficacy as monotherapies, Tat-SPs also exhibited synergistic effects with established chemotherapeutic and targeted agents in vitro, including first-line treatments such as Venetoclax and Cytarabine. These results broaden the potential application of Tat-SPs as anti-AML agents and suggest that their mechanisms of action may be distinct from those of Venetoclax or Ara-C. Nevertheless, the precise molecular mechanisms underlying Tat-SP-induced cell death remain to be elucidated, warranting further investigation into the basis of their cytotoxicity.

Chapter 5 Mechanistic insights into Tat-SPs-induced autotic cell death in AML

5.1 Exclusion of canonical programmed cell death pathways in Tat-SP-induced cytotoxicity

Given the pronounced cytotoxicity and mitochondrial dysfunction elicited by Tat-SPs in AML cells, we undertook a series of mechanistic studies to elucidate the pathways through which Tat-SPs mediate malignant cell death. Programmed cell death (PCD) encompasses a spectrum of tightly regulated cellular processes, each characterized by distinct molecular signatures and morphological features. The principal PCD modalities include apoptosis, necroptosis, ferroptosis, and pyroptosis, all of which play critical roles in maintaining tissue homeostasis and physiological function. To delineate the mechanism underlying Tat-SP-induced cytotoxicity, we systematically interrogated these canonical PCD pathways using established molecular and pharmacological markers.

Necroptosis is a caspase-independent, regulated necrotic cell death pathway, typified by plasma membrane rupture and the subsequent release of intracellular contents, often provoking inflammatory responses. This pathway is critically dependent on receptor-interacting serine/threonine-protein kinase 1 (RIPK1), and can be selectively inhibited by Necrostatin-1. To evaluate the involvement of necroptosis, HL60 cells were seeded at a density of 5×10^4 cells per 100 μL per well in 96-well

plates and co-treated with Necrostatin-1 and Tat-SPs. Cell viability was assessed via trypan blue exclusion following overnight incubation. As depicted in Figures 5.1A and 5.1B, Necrostatin-1 alone did not affect cell viability, nor did it rescue Tat-SP-induced cell death. These findings suggest that necroptosis does not contribute to Tat-SP-mediated cytotoxicity in HL60 cells.

Ferroptosis is an iron-dependent form of regulated cell death, closely linked to cellular metabolic processes and characterized by mitochondrial dysfunction and lipid peroxidation. In HL60 cells, the ferroptosis inducer Erastin significantly reduced cell viability, an effect that was reversed by the ferroptosis inhibitor Ferrostatin-1. In contrast, co-treatment with Ferrostatin-1 failed to restore viability in Tat-SP-treated HL60 cells in Figures 5.1C and D, indicating that ferroptosis is not implicated in Tat-SP-induced cell death.

Pyroptosis is a pro-inflammatory form of cell death, distinguished by membrane rupture and the release of cytokines, and is mechanistically defined by the cleavage of gasdermin proteins (GSDMs), which form membrane pores. To assess pyroptosis, THP-1 cells were seeded at 1×10^6 cells per well in 6-well plates and treated with Tat-SPs or Venetoclax. Western blot analysis was performed to detect cleaved GSDME. As shown in Figure 5.1E, cleaved GSDME was minimally detected in Tat-SP-treated cells, whereas Venetoclax induced a dose-dependent increase in GSDME cleavage. These results indicate that pyroptosis is not a major contributor to Tat-SP-induced cell death

in THP-1 cells.

A

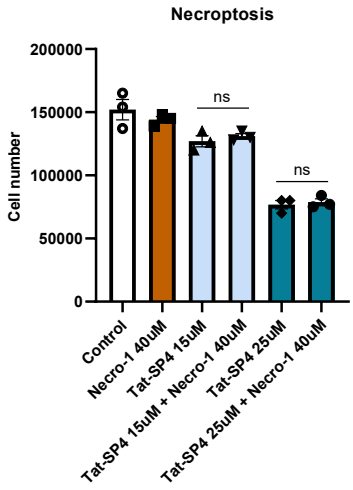

B

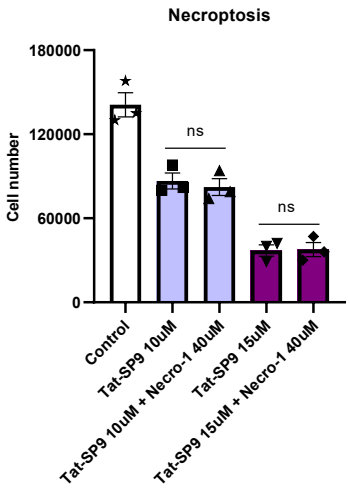

C

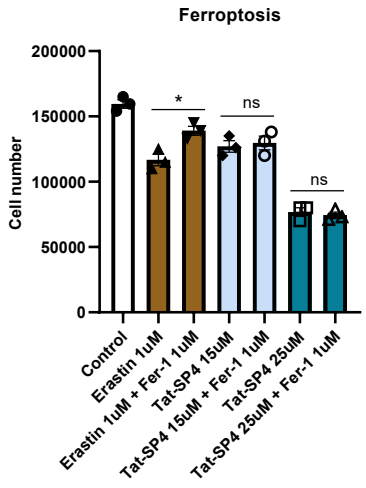

D

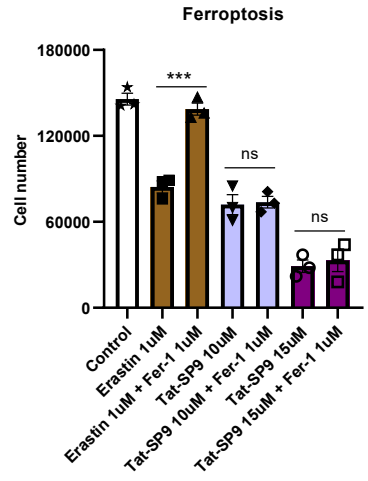

E

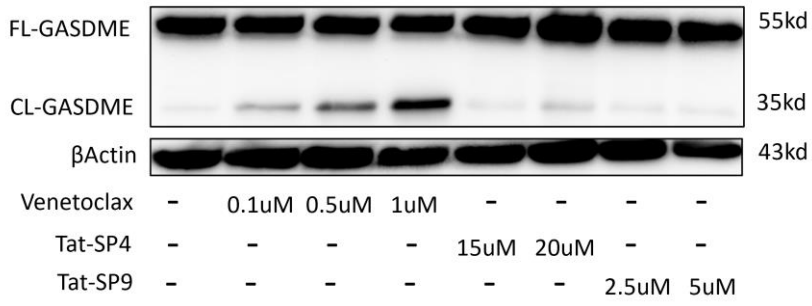

Figure 5.1 Mechanistic study of necroptosis, ferroptosis, and pyroptosis for Tat-

SPs in AML cells. (A, B) Cell viability analysis of HL60 cells co-treated with Tat-SPs and the necroptosis inhibitor Necrostatin-1. (C, D) Cell viability analysis of HL60 cells co-treated with Tat-SPs and the ferroptosis inhibitor Ferrostatin-1; Erastin was used as a positive control for ferroptosis induction. For all viability assays, cells were treated overnight, and viable cell counts were determined using a hemocytometer and the trypan blue exclusion method. Data are presented as mean ± SEM from replicate experiments. Statistical significance was determined by two-way ANOVA, $*P < 0.05$, $***P < 0.001$. (E) Western blot analysis of THP-1 cells following treatment of Tat-SPs or Venetoclax, assessing the cleavage of GSDME as a molecular marker of pyroptosis.

Apoptosis is characterized by specific features, including cell shrinkage and intact cell membranes throughout the process, making it an immune-silent form of cell death as no intracellular contents are released. It plays a crucial role in eliminating damaged or unwanted cells, thereby maintaining tissue development and homeostasis. A hallmark of apoptosis is its caspase-dependent mechanism, involving initiator caspases such as caspase-8 and caspase-9 in the initiation phase, and effector caspases such as caspase-3 and caspase-7 in the degradation phase. HL60 cells were treated with Tat-SPs overnight or with Venetoclax for 48 hours, followed by annexin V and propidium iodide (PI) staining for flow cytometric analysis. As illustrated in Figure 5.2A, Venetoclax induced apoptosis in a dose-dependent manner, as evidenced by increased annexin V positivity. In contrast, Tat-SP9 treatment resulted in a predominant shift of the cell population to the necrotic quadrant, rather than the apoptotic region.

A

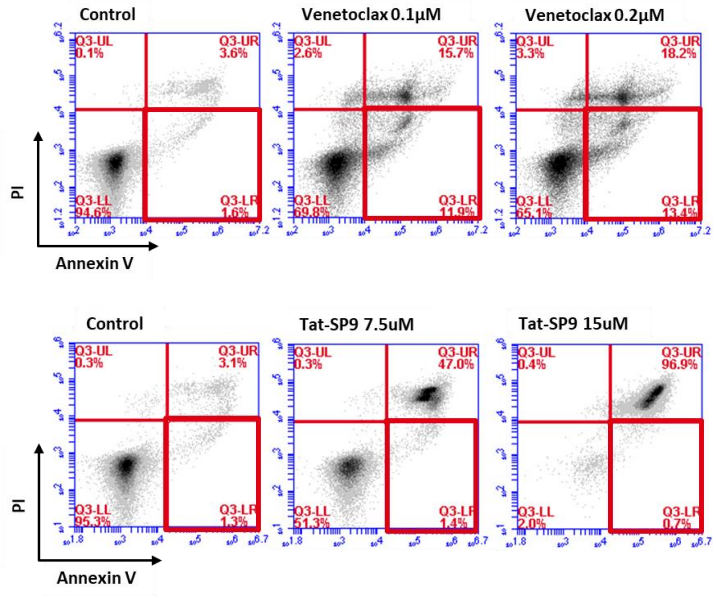

B

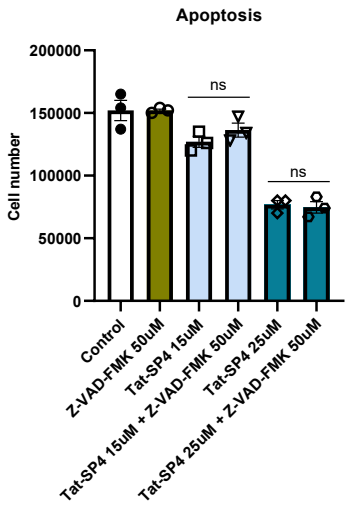

C

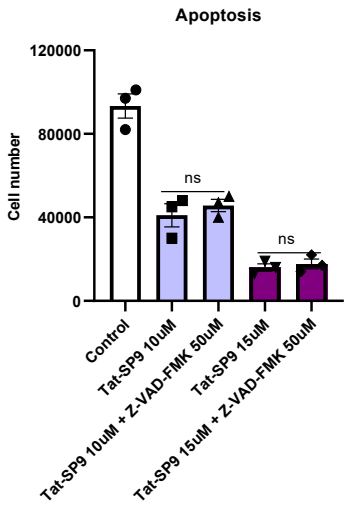

D

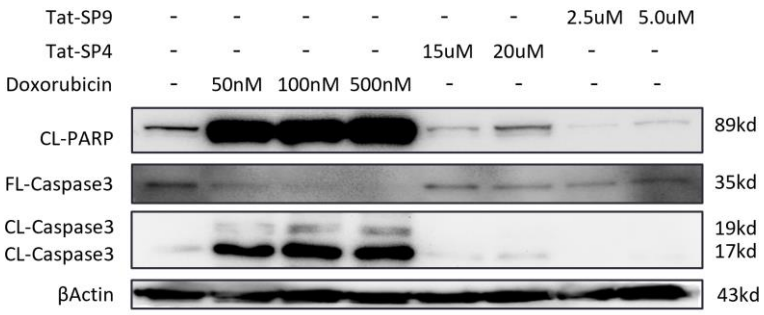

Figure 5.2 Mechanistic study of apoptosis for Tat-SPs in AML cells. (A) Flow

cytometric analysis of HL60 cells treated with Venetoclax or Tat-SP9. The red frame indicates the population corresponding to apoptotic cell death, as determined by annexin V and propidium iodide staining. (B, C) Cell viability analysis of HL60 cells co-treated with Tat-SPs and the pan-caspase inhibitor Z-VAD-FMK. Viable cell counts were determined using a hemocytometer and the trypan blue exclusion method following the indicated treatments. Data are presented as mean ± SEM from replicate experiments. Statistical significance was assessed by two-way ANOVA. (D) Western blot analysis of Molm13 cells treated with Tat-SPs or the apoptosis inducer Doxorubicin, evaluating the cleavage of PARP and caspase-3 (17 and 19 kDa fragments) as molecular markers of apoptosis.

To further probe the involvement of apoptosis, cells were co-treated with the pan-caspase inhibitor Z-VAD-FMK. As shown in Figures 5.2B and C, Z-VAD-FMK did not confer protection against Tat-SP-induced cell death. Additionally, in Molm13 AML cells, western blot analysis revealed that Tat-SPs treatment did not induce cleavage of caspase-3 or its downstream substrate poly (ADP-ribose) polymerase (PARP), in contrast to the robust cleavage observed with the apoptosis inducer Doxorubicin, shown in Figure 5.2D. These data collectively indicate that Tat-SP-induced cell death proceeds independently of the canonical apoptotic pathway.

It is important to note that the absence of a positive control for necroptosis limits the conclusiveness of our findings regarding this pathway. Morphological observations

of membrane rupture and loss of cellular architecture in Tat-SP-treated cells are reminiscent of necroptosis; however, definitive involvement requires further investigation, including assessment of key necroptotic regulators such as RIPK1 and RIPK3. Given the complexity and potential interplay of cell death pathways, it is plausible that multiple mechanisms may contribute to Tat-SP-induced cytotoxicity. Nevertheless, our data suggest that necroptosis is not the primary mode of cell death in this context.

Notably, Venetoclax, a BCL-2 inhibitor, has been shown to induce both apoptosis and pyroptosis in AML cells, as evidenced by GSDME cleavage in THP-1 cells, consistent with previous reports (Ye et al., 2023). In contrast, Tat-SPs induce profound mitochondrial damage, including mitochondrial permeability transition pore opening and loss of membrane potential, which would typically be expected to trigger cytochrome c release and apoptosis. However, the absence of apoptotic and pyroptotic markers in Tat-SP-treated cells suggests that Tat-SPs activate a distinct, non-canonical cell death pathway. The divergent mechanisms of Venetoclax and Tat-SPs, particularly regarding their effects on mitochondrial integrity, raise the intriguing possibility that combination therapy could synergistically enhance AML cell eradication by maximizing mitochondrial dysfunction.

5.2 Characterization of autophagy modulation by Tat-SPs in AML cells

5.2.1 Detection of subtle autophagic responses following Tat-SP treatment

Given that Tat-SPs were rationally designed to target Beclin-1 and enhance autophagy in tumor cells, we assessed their effects on canonical markers of autophagic flux, namely microtubule-associated protein 1A/1B-light chain 3 (LC3) and Sequestosome-1 (p62/SQSTM1). As detailed in Section 1.2, conversion of cytosolic LC3-I to its lipidated form LC3-II reflects autophagosome formation, with LC3-II accumulation serving as a hallmark of increased autophagic activity. In contrast, p62 acts as an autophagy adaptor and is degraded during autophagy; thus, decreased p62 levels indicate efficient autophagic flux. Accordingly, a simultaneous increase in LC3-II and decrease in p62 is indicative of enhanced autophagy. To further delineate autophagic flux, we utilized chloroquine (CQ), which inhibits autophagosome-lysosome fusion and prevents degradation of autophagic cargo. This approach enables discrimination between increased autophagosome formation and impaired autophagic degradation.

In this study, Molm13 cells were seeded in 6-well plates at a density of 1×10^6 cells per well in 2mL of culture medium. Following treatment with Tat-SPs or CQ for three hours, cells were harvested, washed with PBS, and lysed. Protein denaturation was achieved by boiling, and samples were subjected to SDS-PAGE followed by

immunoblotting. Band intensities were quantified using ImageJ software. All experiments were performed in triplicate to enable statistical analysis.

In Molm13 cells, Tat-SP4 treatment resulted in a dose-dependent reduction of p62 levels, while LC3-II expression remained largely unchanged at concentrations of 15 and 20 μM. With CQ cotreatment, both LC3-II and p62 levels increased in all groups, and the significant reduction in p62 induced by Tat-SP4 persisted, as presented in Figure 5.3B. In contrast, LC3-II levels were minimally affected by Tat-SP4, regardless of CQ treatment. Similarly, Tat-SP9 elicited a dose-dependent decrease in p62 levels, both with and without CQ, although the statistical significance was less pronounced compared to Tat-SP4, likely due to greater experimental variability, as shown in Figure 5.3A and D. Interestingly, a reduction in LC3-II levels was observed at 2.5 and 5 μM Tat-SP9, though this did not reach statistical significance, in Figure 5.3A and E.

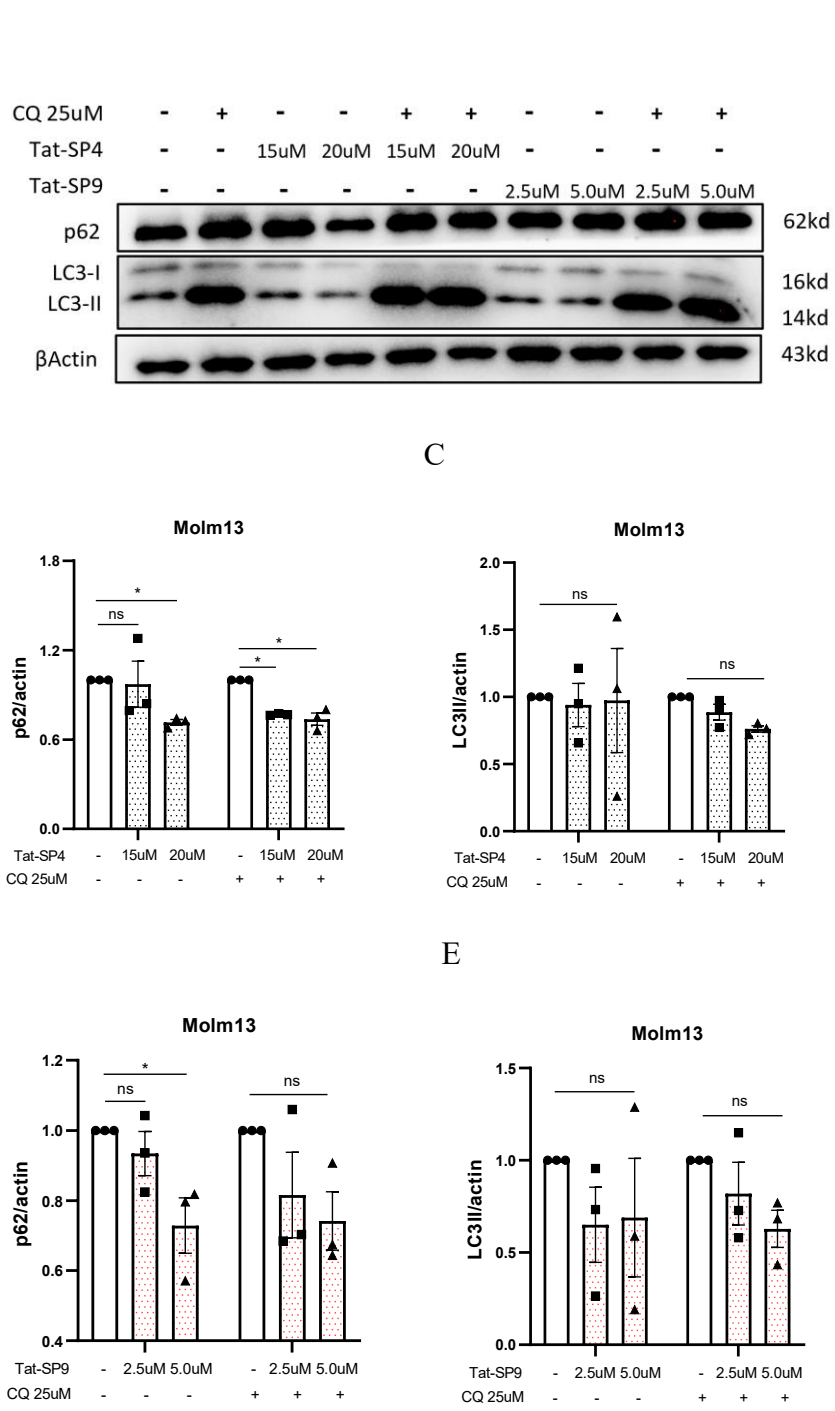

Figure 5.3 Tat-SPs enhance mild autophagy in AML cells. (A) Representative Western blot analysis of Molm13 cells treated with Tat-SPs in the presence or absence of chloroquine (CQ) for 3 hours. (B, C) Quantitative analysis of p62 and LC3-II expression levels in Molm13 cells following treatment with Tat-SP4 for 3 hours, as determined by densitometric analysis of Western blot bands. (D, E) Quantitative

analysis of p62 and LC3-II expression levels in Molm13 cells following treatment with Tat-SP9 for 3 hours. Densitometric quantification was performed using ImageJ software. Data are presented as mean ± SEM from three independent experiments. Statistical significance was assessed using two-way ANOVA; *P < 0.05.

While both Tat-SP4 and Tat-SP9 consistently decreased p62 levels, their effects on LC3-II were less definitive. Notably, LC3-I was scarcely detectable in Molm13 cells (Figure 5.3A, first lanes), suggesting a limited capacity for further conversion to LC3-II upon autophagy induction. This may account for the absence of a marked increase in LC3-II following Tat-SP4 treatment, as presented in Figure 5.3A and C. The substantial increase in LC3-II observed after CQ treatment in control cells indicates a high basal level of autophagy in Molm13 cells, which may mask mild enhancement induced by Tat-SPs. Additionally, the large error bars observed in LC3-II quantification reflect considerable experimental variability, highlighting the need for further optimization to draw definitive conclusions. Collectively, these findings suggest that subtle autophagic activity can be induced by Tat-SPs in Molm13 cells. Although robust autophagic disruption is unlikely to be the primary mechanism underlying Tat-SP-induced cell death, a contributory role for autophagy cannot be excluded.

The observed decrease in LC3-II levels with Tat-SP9 treatment is difficult to interpret, as high variability among replicates suggests limited experimental reproducibility. It is also possible that Molm13 cells possess intrinsic defects in LC3

processing due to their leukemic origin. For future studies, several improvements should be considered. The inclusion of positive controls, such as established autophagy inducers like rapamycin, would enhance the interpretability and robustness of these results. Furthermore, optimization of experimental parameters—including treatment duration, peptide concentration, and lysis buffer composition—may improve detection sensitivity and reproducibility. Finally, to determine whether the limited autophagic response is specific to Molm13 cells, it would be informative to extend these analyses to additional AML cell lines.

5.2.2 Rescue of Tat-SP-induced cytotoxicity by autophagy inhibitors

In addition to evaluating the expression levels of p62 and LC3-II, we further investigated the role of autophagy in Tat-SP-induced cytotoxicity by employing the autophagy inhibitor 3-Methyladenine (3-MA). 3-MA is a well-characterized inhibitor that blocks PI3K activity, thereby suppressing autophagy at an early stage by preventing autophagosome nucleation. To assess the impact of autophagy inhibition on Tat-SP-mediated cell death, both HL60 and Molm13 cells were seeded at a density of 5×10^4 cells per well in 96-well opaque plates containing culture medium supplemented with 8 mM 3-MA. Following 3 hours pre-treatment with 3-MA, Tat-SP peptides were added to induce cytotoxicity. Cell viability was subsequently quantified using the CellTiter-Lumi assay, which measures ATP-dependent luminescence as an indicator of metabolically active, viable cells.

As shown in Figure 5.4, treatment with 8 mM 3-MA alone did not significantly affect the viability of either HL60 or Molm13 cells. However, pre-treatment with 3-MA markedly attenuated the cytotoxic effects of Tat-SPs in both cell lines with both low and high concentration, indicating that Tat-SPs were no longer able to efficiently induce cell death under conditions of autophagy inhibition. These findings suggest that the cytotoxicity of Tat-SPs is associated to the autophagic process, with early-stage autophagy playing a critical role in mediating Tat-SP-induced cell death in AML blasts.

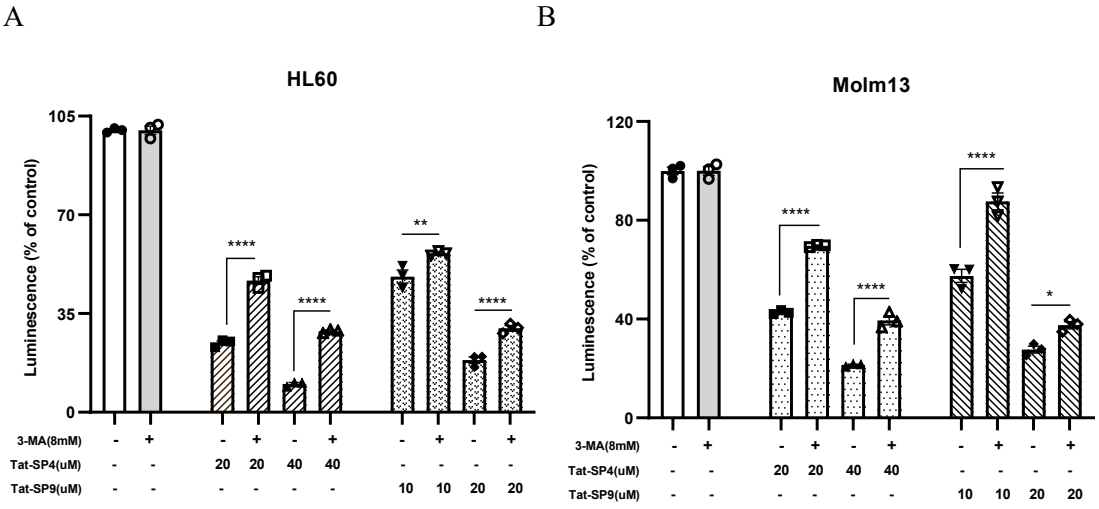

Figure 5.4 Tat-SPs induced cell death can be rescued by autophagy inhibitor. (A) Cell viability analysis of HL60 cells treated with Tat-SPs in the presence or absence of the autophagy inhibitor 3-MA, as measured by the CellTiter-Lumi assay. (B) Cell viability analysis of Molm13 cells under the same treatment conditions. Data represent mean ± SEM of replicates. Significance analyzed by two-way ANOVA, ∗P < 0.05, ∗∗P < 0.01, ∗∗∗P < 0.001, ∗∗∗∗P < 0.0001.

Although western blot analyses did not reveal robust reductions in p62 or

accumulation of LC3-II, the observation that 3-MA confers protection against Tat-SP-induced cell death is noteworthy. This result implies that a basal or selective level of autophagy, even if not strongly reflected by changes in bulk autophagy markers, may be essential for the cytotoxic action of Tat-SPs. It is well established that autophagy can facilitate cell death in certain contexts, particularly in cancer cells subjected to metabolic or therapeutic stress. Tat-SPs may therefore trigger a form of autophagy-related cell death, wherein inhibition of autophagosome formation by 3-MA disrupts this process and rescues cell viability. One possible mechanism is that autophagy primes cells for death by degrading survival factors or modulating mitochondrial function, which is consistent with previous findings of Tat-SP-induced mitochondrial toxicity. Furthermore, the absence of pronounced changes in p62 or LC3-II does not entirely exclude the involvement of autophagy, as Tat-SPs may induce selective autophagic pathways not fully captured by these conventional markers.

5.3 Validation of autotic cell death triggered by Tat-SPs

5.3.1 Suppression of Tat-SP-induced autosis by specific inhibitors

Autosis, a distinct form of cell death associated with excessive autophagy, was also investigated to elucidate its potential involvement in the mechanism of action of Tat-SPs. First characterized by Beth Levine's laboratory, autosis is defined by unique morphological features and can be specifically rescued by Na^+/K^+-ATPase inhibitors

such as Digoxin, although the precise molecular mechanisms remain incompletely understood (Liu et al., 2013; Liu & Levine, 2015). Given that Tat-SPs were designed to induce autophagy and that morphological evidence of plasma membrane damage—characteristic of autotic cell death—was observed during cell culture, we hypothesized that autosis may represent the predominant mode of cell death in AML cells treated with Tat-SPs.

To test this hypothesis, HL60 cells were seeded at a density of 5×10^4 cells per well in 96-well plates and pretreated with 5 μM Digoxin for 3 hours prior to the addition of Tat-SPs at various concentrations. Following peptide treatment for another 3 hours, cell viability was assessed using the trypan blue exclusion assay.

As shown in Figure 5.5, Digoxin alone did not affect the cell viability but pre-treatment with 5 μM Digoxin partially inhibited the cytotoxic effects of Tat-SPs in HL60 cells. Both low and high concentrations of Tat-SP4 and Tat-SP9 demonstrated significantly increased cell viability in the presence of Digoxin compared to groups without Digoxin pre-treatment. Although Digoxin did not completely abrogate Tat-SP-induced cytotoxicity at the highest peptide concentrations, such as in groups of 25 μM Tat-SP4 and 15 μM Tat-SP9, its protective effect was notable. The rescue effect of Digoxin appeared more pronounced than that observed with 8 mM 3-MA, although direct comparison is limited by the use of different viability assays, that CellTiter-Lumi for 3-MA and trypan blue exclusion for Digoxin. Furthermore, the robustness of these

findings would benefit from validation in additional AML cell lines to confirm the generalizability of Digoxin's protective effect.

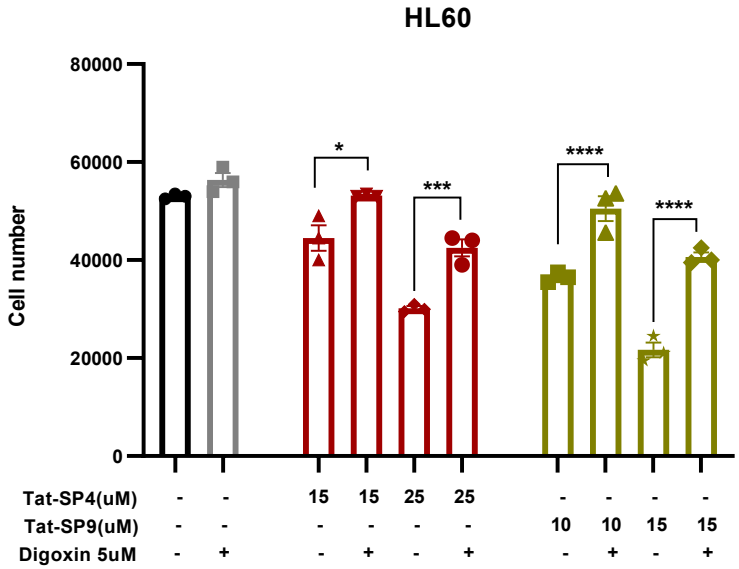

Figure 5.5 Tat-SPs induced cell death can be rescued by autosis inhibitor. Cell viability analysis of in HL60 cells treated with Tat-SPs and Digoxin. Viable cell counts were determined using a hemocytometer and the trypan blue exclusion method following the indicated treatments. Data represent mean ± SEM of replicates. Significance analyzed by two-way ANOVA. ∗P < 0.05, ∗∗∗P < 0.001, ∗∗∗∗P < 0.0001.

The observation that Digoxin rescues cells from Tat-SP-induced death, in a manner analogous to 3-MA, is particularly intriguing. Digoxin, a cardiac glycoside, inhibits the Na^+/K^+-ATPase pump, thereby altering membrane potential and disrupting ion homeostasis. In the context of autosis, Digoxin is thought to suppress autophagic flux indirectly, potentially by interfering with ion gradients required for autophagosome-lysosome fusion or by stabilizing cellular membranes under autophagic stress. The

ability of Digoxin to rescue cells from Tat-SP-induced cytotoxicity supports the hypothesis that Tat-SP-mediated cell death is autophagy-dependent and consistent with autosis. Microscopic observation of Tat-SP-treated AML cells revealed morphological features characteristic of autosis, including loss of plasma membrane integrity and depletion of intracellular organelles, further corroborating this mechanism in accordance with Levine's criteria.

5.3.2 Immunogenic features of Tat-SP-mediated autotic cell death

Morphological changes characteristic of autotic cell death was observed in Tat-SP-treated cells, together with the partial inhibition of cell death by the autosis inhibitor digoxin and the observed increase in cellular ROS, suggest that immunogenic cell death (ICD) may also be involved in the Tat-SP-induced autotic cell death process.

Immunogenic cell death is defined by the release of immunostimulatory molecules, collectively known as damage-associated molecular patterns (DAMPs), which serve to activate the immune system. Key DAMPs implicated in ICD include calreticulin (CRT), high-mobility group box 1 (HMGB1), and extracellular ATP, all of which are released during the execution of ICD. This form of cell death is of particular interest in cancer immunotherapy, as it promotes the recruitment and maturation of DCs, enhances antigen presentation to cytotoxic T lymphocytes, and ultimately facilitates the elimination of malignant cells, as illustrated in Figure 5.6 (Arimoto et al., 2024).

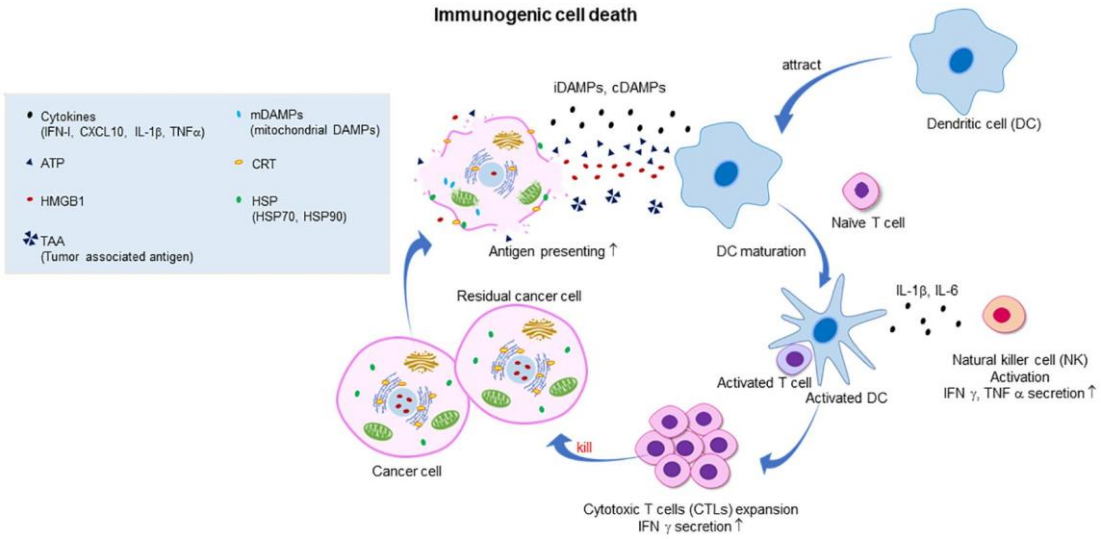

Figure 5.6 Immunogenic cell death (Arimoto et al, 2024).

To investigate the potential immunogenicity of Tat-SP-induced cell death, we specifically assessed extracellular ATP release and HMGB1 secretion in Tat-SP-treated cells. For the analysis of extracellular ATP, HL60 and THP-1 cells were seeded at a density of 5×10^4 cells per well in opaque 96-well plates and subjected to treatment with various concentrations of Tat-SP peptides. Real-time ATP release was quantified using the RealTime-Glo™ Extracellular ATP Assay (Promega) and measured with a microplate reader.

As shown in Figures 5.7A and 5.7B, ATP release was closely correlated with Tat-SP4 dosage. At lower concentrations, ATP release increased gradually and reached lower peak levels, whereas higher concentrations of Tat-SP4 induced a more rapid and pronounced ATP release, with peaks occurring earlier and sustained elevated levels.

Notably, significant ATP release was detected as early as 10 to 20 minutes post-treatment, with the process largely completed within 60 minutes. In HL60 cells, Tat-SP4 at 30 or 40 μM significantly stimulated ATP release, and 50 μM Tat-SP4 resulted in a marked increase, although the time to peak remained consistent. THP-1 cells exhibited a similar trend, but lower concentrations (≤10 μM) of Tat-SP4 failed to induce substantial ATP release. For THP-1 cells, 30 and 40 μM Tat-SP4 elicited dose-dependent ATP generation, albeit at slightly lower levels than in HL60 cells, indicating cell line-specific differences in sensitivity.

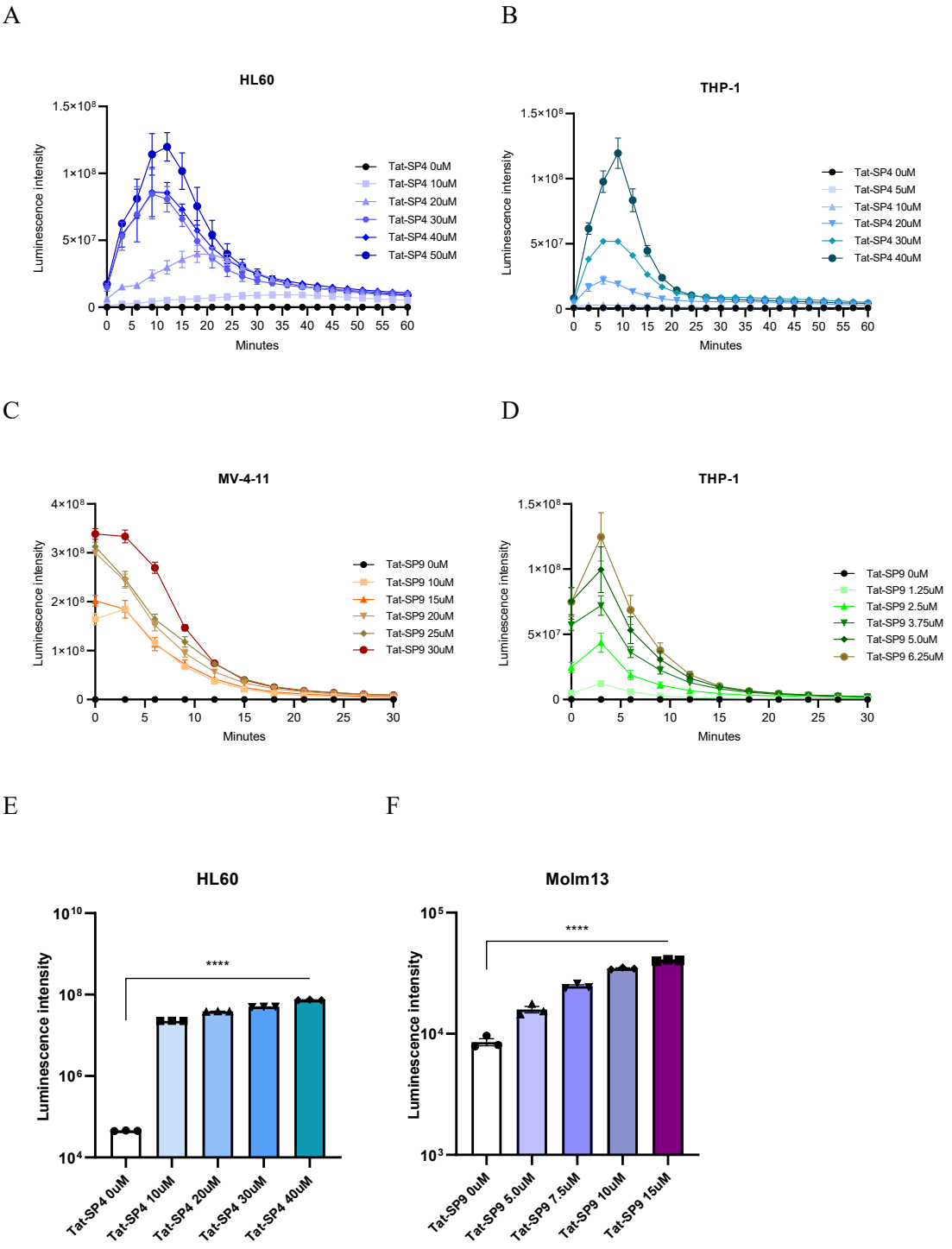

Figure 5.7 Autotic cell death caused by Tat-SPs is immunogenic cell death. (A–D) Real-time analysis of extracellular ATP release in HL60, THP-1, and MV-4-11 cells treated with a series of Tat-SPs concentrations. Luminescence was measured at 3-minute intervals using a plate reader maintained at 37°C. (E, F) Quantification of

extracellular HMGB1 levels in HL60 and Molm13 cells following treatment with Tat-SP4 and Tat-SP9, respectively. Data represent mean ± SEM of replicates. Significance analyzed by two-way ANOVA, ****P < 0.0001.

For Tat-SP9, ATP release occurred more rapidly than with Tat-SP4, as illustrated in Figures 5.7C and D. In MV-4-11 cells, peak ATP levels were detected within approximately 5 minutes, and in THP-1 cells, within 10 minutes of treatment. Tat-SP9 also induced dose-dependent ATP release, with THP-1 cells demonstrating greater sensitivity; for instance, 6.25μM Tat-SP9 achieved peak ATP levels comparable to those observed with 40μM Tat-SP4.

Extracellular HMGB1 levels were measured using the Lumit™ HMGB1 (Human/Mouse) Immunoassay (Promega), following the manufacturer's protocol. HL60 and Molm13 cells were seeded as described for the eATP experiments, treated with Tat-SPs, and subsequently stained with the Lumit™ detection reagent prior to analysis by microplate reader. As shown in Figures 5.7E and 5.7F, a significant and dose-dependent increase in HMGB1 release was observed in both HL60 and Molm13 cells following Tat-SPs treatment. These findings further support the involvement of ICD in Tat-SP-induced cell death.

Collectively, our results demonstrate that Tat-SP-induced autotic cell death exhibits hallmarks of immunogenic cell death, suggesting that peptide treatment in vivo

could elicit robust immune responses through the release of immunogenic DAMPs. This adds a novel dimension to the therapeutic potential of Tat-SPs. This raises the possibility of combining Tat-SPs with immune checkpoint inhibitors, such as anti-PD-1 or anti-PD-L1 antibodies, to potentiate anti-leukemic immunity. Ongoing studies are aimed at further elucidating the immune activation effects of Tat-SPs and their potential for combination immunotherapy.

5.4 Calcium-dependent regulation of Tat-SP-induced autosis

5.4.1 Attenuation of Tat-SP cytotoxicity by extracellular calcium

Our previous research demonstrated that calcium plays a significant role in modulating the cytotoxicity of Tat-SPs in cancer cells. Building on these findings, we further investigated the potential of extracellular calcium to rescue acute myeloid leukemia cells from Tat-SP-induced cell death. HL60 and Molm13 cells were seeded in white opaque 96-well plates and cultured in media supplemented with varying concentrations of calcium. Following peptide treatment, cell viability was assessed using the CellTiter-Lumi assay in conjunction with a microplate reader.

As illustrated in Figure 5.8A, both HL60 and Molm13 cell lines exhibited substantial resistance to Tat-SP-induced cytotoxicity in the presence of elevated extracellular calcium, even at concentrations as high as 3.0 mM. The addition of

extracellular calcium to the culture medium conferred a dose-dependent protective effect against Tat-SP-induced cell death. Specifically, increasing calcium concentrations from 0.6 mM to 3.0 mM progressively rescued HL60 cells from cytotoxicity induced by 20μM Tat-SP4, with near-complete protection observed at 2.4 mM calcium. A similar trend was observed for Tat-SP9-induced cytotoxicity, although the maximal protective effect was achieved at 2.4 mM calcium, with a slight reduction in rescue efficacy at 3.0 mM in the presence of 10μM Tat-SP9. In Molm13 cells, as shown in Figure 5.8B, extracellular calcium also exerted a protective effect, though to a lesser extent; significant rescue from 10 μM Tat-SP9-induced cytotoxicity was only observed at calcium concentrations exceeding 1.8 mM.

A

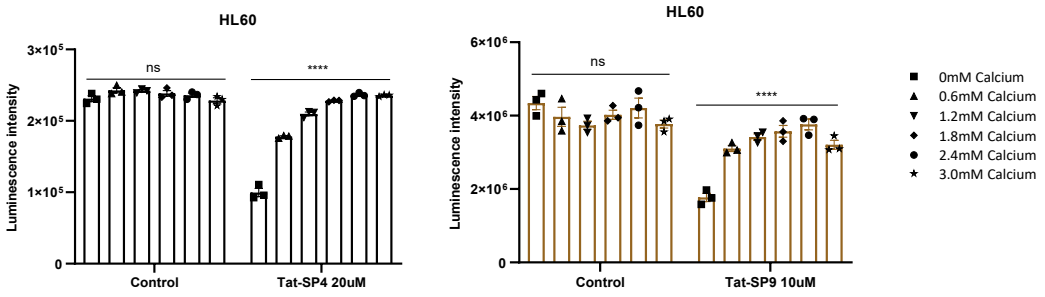

B

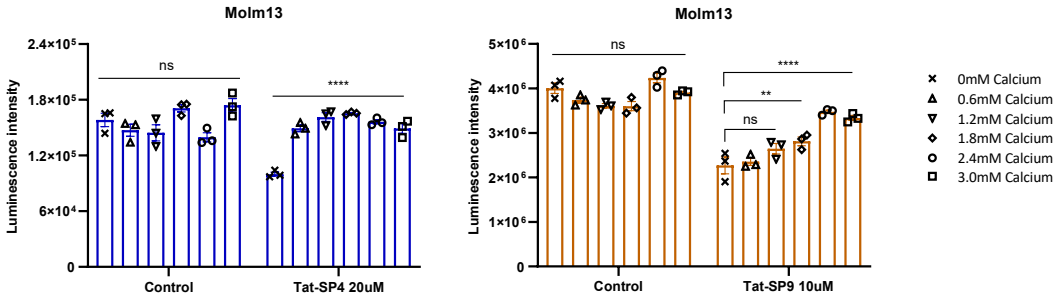

Figure 5.8 Tat-SPs induced cell death can be blocked by addition of calcium. (A) Cell viability analysis of HL60 cells treated with Tat-SPs in the presence or absence of calcium by CellTiter-Lumi assay. (B) Cell viability analysis of Molm13 cells treated with Tat-SPs in the presence or absence of calcium by CellTiter-Lumi assay. Data represent mean ± SEM of replicates. Significance analyzed by two-way ANOVA, ∗P < 0.05, ∗∗P < 0.01, ∗∗∗P < 0.001, ∗∗∗∗P < 0.0001.

These results suggest that the cytotoxic effects of Tat-SPs are closely linked to calcium-dependent pathways. Our previous investigations into MPTP activation indicated that Tat-SPs may enhance mitochondrial calcium signaling, supporting the hypothesis that calcium dynamics contribute to Tat-SP-induced cell death in AML cells. Intriguingly, supplementation with high levels of extracellular calcium abrogated,

rather than potentiated, the cytotoxic effects of Tat-SPs. This observation implies that extracellular calcium may either compete with Tat-SPs for binding to ion-regulatory pathways or activate compensatory cellular mechanisms that mitigate Tat-SP-induced cytotoxicity. These findings highlight the complex interplay between Tat-SPs and calcium signaling in AML cells and suggest that modulation of extracellular calcium levels may significantly influence the therapeutic efficacy of Tat-SP-based treatments.

5.4.2 Modulation of Tat-SP-induced autosis by intracellular calcium dynamics

Inspired by the observed protective effects of extracellular calcium against Tat-SP-induced cytotoxicity, we further investigated the role of intracellular calcium regulation in modulating Tat-SP activity. The endoplasmic reticulum (ER) serves as the principal intracellular calcium reservoir, maintaining calcium concentrations in the millimolar range. The ER functions as a dynamic calcium buffer, importing calcium via sarcoplasmic/endoplasmic reticulum calcium ATPase (SERCA) pumps and releasing it through inositol 1,4,5-trisphosphate receptors (IP3Rs). The close physical association between the ER and mitochondria forms specialized structures known as mitochondria-associated membranes (MAMs), which facilitate the transfer of calcium from the ER to mitochondria via the mitochondrial calcium uniporter (MCU). This inter-organelle calcium flux is critical for mitochondrial ATP production, oxidative phosphorylation, and the maintenance of cellular calcium homeostasis.

To dissect the contribution of intracellular calcium flux to Tat-SP-induced cell death, we employed three pharmacological agents targeting distinct aspects of calcium regulation: the cytosolic calcium chelator BAPTA-AM, the ER stress inducer Thapsigargin, and the MCU inhibitor RU360. The mechanisms of action for these inhibitors are summarized in Figure 5.9A (Giorgi et al., 2018).

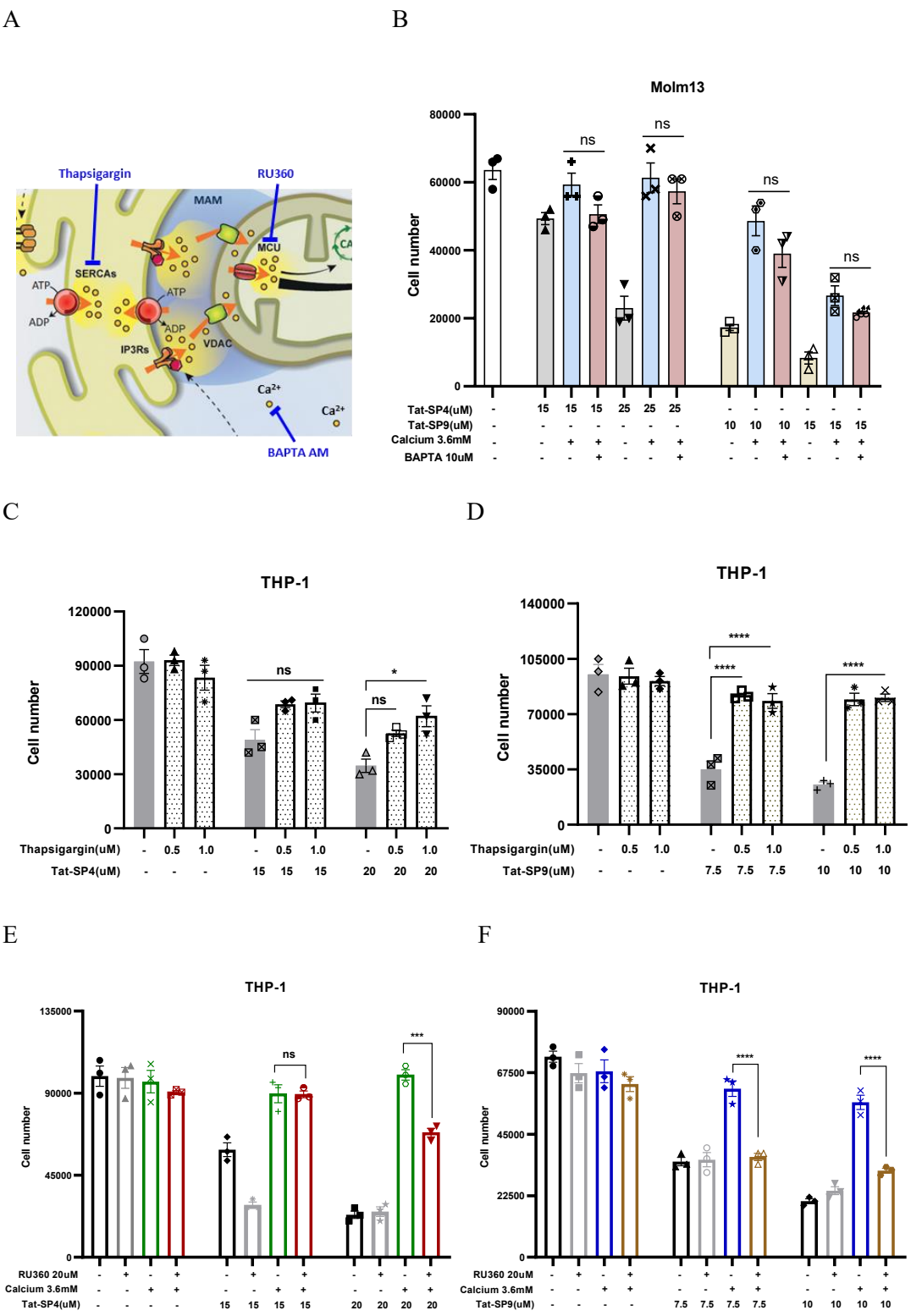

Figure 5.9 Tat-SPs cytotoxicity can be affected by intracellular calcium regulators.

(A) The mechanisms of action of these inhibitors applied in calcium regulation study

(Giorgi et al., 2018). (B) Cell viability analysis of Molm13 cells treated with Tat-SPs and the cytosolic calcium chelator BAPTA-AM in the presence of supplemental extracellular calcium. (C, D) Cell viability analysis of THP-1 cells treated with Tat-SPs and the ER stress inducer Thapsigargin. (E, F) Cell viability analysis of THP-1 cells treated with Tat-SPs and the MCU inhibitor RU360, with supplemental extracellular calcium. In this experimental setting, THP-1 cells were pretreated with RU360 for 6 hours prior to the addition of Tat-SPs and calcium. In all panels, viable cell counts were determined using a hemocytometer and the trypan blue exclusion assay following the indicated treatments. Data represent mean ± SEM of replicates. Significance analyzed by two-way ANOVA, $*P < 0.05$, $**P < 0.01$, $***P < 0.001$, $****P < 0.0001$.

BAPTA-AM is a membrane-permeable, highly selective calcium chelator. Upon entry into the cell, its acetoxymethyl ester group is cleaved, allowing BAPTA to bind free cytosolic calcium and thereby reduce its intracellular concentration. Molm13 cells were seeded in 96-well plates and treated with Tat-SPs, calcium supplementation, and BAPTA-AM simultaneously. Cell viability was assessed 24 hours later using the trypan blue exclusion assay, with results presented in Figure 5.9B. The protective effect of 3.6 mM extracellular calcium against Tat-SP-induced cytotoxicity was attenuated by BAPTA-AM in both Tat-SP4 and Tat-SP9 treatment groups, across a range of peptide concentrations. However, these effects did not reach statistical significance. These findings suggest that alterations in free cytosolic calcium alone have a limited direct impact on Tat-SP-mediated cytotoxicity, indicating a more complex mechanism of

action.

To further probe the role of ER calcium stores, THP-1 cells were co-treated with Thapsigargin and Tat-SPs, and cell viability was measured after overnight incubation. As shown in Figures 5.9C and D, Thapsigargin exhibited a notable protective effect against Tat-SP-induced cytotoxicity. Treatment with 0.5 and 1 μM Thapsigargin rescued THP-1 cells from Tat-SP4-induced cell death, with 1 μM Thapsigargin providing the most pronounced protection. This rescue effect was even more significant in Tat-SP9-treated cells, where 0.5 μM Thapsigargin substantially increased cell viability in the presence of 7.5 and 10 μM Tat-SP9. The likely explanation for this phenomenon is that Thapsigargin-induced ER stress leads to the release of calcium from the ER into the cytosol and mitochondria, thereby elevating cytosolic and mitochondrial calcium levels. This increase may interfere with the cytotoxic action of Tat-SPs, ultimately promoting cell survival.

In a separate experimental setting, THP-1 cells were pre-treated with RU360 for 6 hours prior to the addition of Tat-SPs and calcium, followed by overnight incubation and cell viability assessment via trypan blue exclusion. As shown in Figures 5.9E and F, RU360 pre-treatment did not rescue cells from Tat-SP-induced death. In fact, a higher proportion of THP-1 cells died following treatment with 15 μM Tat-SP4 after RU360 priming. This suggests that mitochondrial calcium overload is unlikely to be the direct cause of Tat-SP-induced cell death. Interestingly, RU360 significantly diminished the

calcium-mediated protective effect against Tat-SP-induced cytotoxicity, particularly in the 20 μM Tat-SP4 group and both Tat-SP9 groups. This observation raises the possibility that mitochondrial calcium uptake is essential for the calcium-mediated rescue of Tat-SP-induced cell death, implying that Tat-SPs may exert their cytotoxic effects within the mitochondrial matrix. However, the increased cell death observed in the group treated with 15 μM Tat-SP4 in the presence of both calcium and RU360 warrants further investigation to clarify the underlying mechanisms.

In conclude, these findings highlight the complexity of calcium signaling in the regulation of Tat-SP-induced cytotoxicity. While extracellular calcium confers a protective effect, the precise roles of cytosolic, ER, and mitochondrial calcium pools require further elucidation to fully understand the interplay between Tat-SPs and intracellular calcium homeostasis in AML cells.

5.5 Summary

Our mechanistic investigations reveal that both first- and second-generation Tat-SP peptides exhibit similar biological activities and induce a distinctive form of cell death known as autosis, which is closely associated with excessive autophagy. Unlike other forms of programmed cell death—including apoptosis, ferroptosis, necroptosis, and pyroptosis—the cytotoxic effects of Tat-SPs were not mitigated by inhibitors targeting these pathways. In contrast, both autophagy and autosis inhibitors effectively

attenuated Tat-SP-induced cytotoxicity, despite only minimal autophagic activity being detected by western blot analysis. While these findings suggest that excessive autophagy may not directly trigger autotic cell death, further studies with more robust autophagic markers are warranted to substantiate this mechanism.

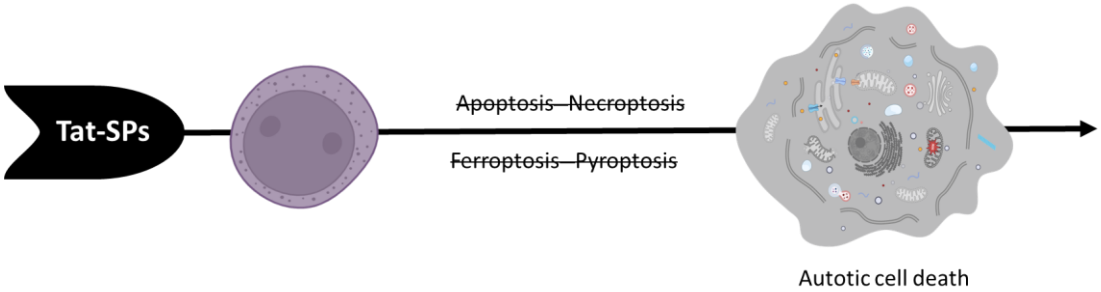

Figure 5.10 Tat-SPs induce autotic cell death in AML blasts.

Additionally, we observed that the cytotoxicity of Tat-SPs in AML cell lines could be dose-dependently rescued by supplementation with extracellular calcium. Notably, chelation of cytosolic calcium alone did not fully abrogate the protective effect of calcium, whereas inhibition of mitochondrial calcium uptake markedly suppressed calcium-mediated rescue. Furthermore, induction of endoplasmic reticulum stress also conferred protection against Tat-SP-induced cytotoxicity, likely by facilitating calcium transfer from the ER to the mitochondria. Collectively, these results suggest that accumulation of calcium within the mitochondrial matrix constitutes a critical pool that counteracts the cytotoxic effects of Tat-SPs, implicating disruption of mitochondrial matrix homeostasis as a key mechanism underlying Tat-SP-induced cell death.

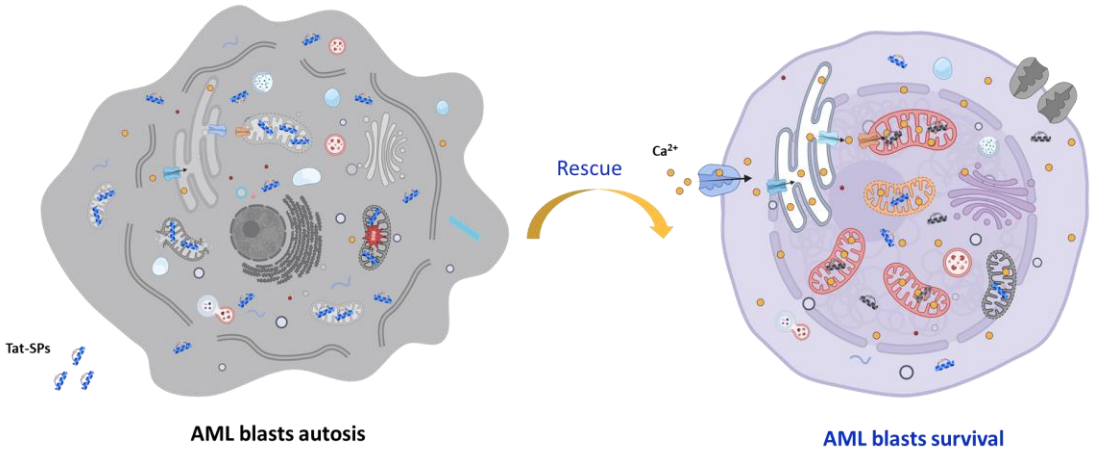

Figure 5.11 Proposed mechanism of intra-mitochondrial matrix calcium in attenuating Tat-SPs cytotoxicity.

Finally, Tat-SP-induced autotic cell death was found to exhibit hallmarks of immunogenic cell death (ICD). Tat-SP treatment triggered a dose-dependent release of extracellular ATP and a significant increase in HMGB1 secretion, indicative of the release of pro-inflammatory DAMPs from AML blasts. These findings suggest that Tat-SPs have the potential to activate the adaptive immune system, thereby enhancing their anti-tumor efficacy in vivo.

Taken together, our data provide compelling evidence that Tat-SPs induce autotic cell death in AML cells through mechanisms involving mitochondrial calcium dynamics and immunogenic signaling, highlighting their promise as novel therapeutic agents for acute myeloid leukemia.

Chapter 6 Investigation of Tat-SP-induced immunological activation

6.1 Induction of autophagy in Jurkat e6.1 T cells by Tat-SPs

As a master regulator of cellular recycling, autophagy plays a pivotal role in supporting the metabolic reprogramming required for T cell activation following antigen recognition. It is conceivable that Tat-SPs may enhance autophagic processes, thereby potentially mitigating T cell exhaustion during anti-tumor immune responses in vivo. Intriguingly, Tat-SPs also appear to modulate calcium homeostasis, which may involve activation of the calcineurin pathway—a critical signaling axis in T cell activation. In this study, we investigated the effects of Tat-SPs on autophagy and activation in Jurkat e6.1 T cells.

Jurkat e6.1T cells were employed as a model to assess T cell function. Cells were treated with Tat-SPs, and autophagy induction was evaluated by immunoblot analysis of LC3 and p62 expression. As observed in AML Molm13 cells, Tat-SPs treatment in Jurkat cells did not result in robust autophagy induction, as shown in Figures 6.1A and 6.1B. A minimal decrease in p62 protein was detected in the 40 μM Tat-SP4 group in the absence of CQ. However, when CQ was used to inhibit autophagic degradation, a more pronounced reduction in p62 levels was observed in the 40 μM Tat-SP4 group compared to the control, although the p62 protein level was still lower than in the corresponding group without CQ. The increase in lipidated LC3 was modest with no substantial accumulation of LC3-II evident in either the 20 or 40 μM Tat-SP4 groups.

Similar results were obtained with Tat-SP9 treatment.

A

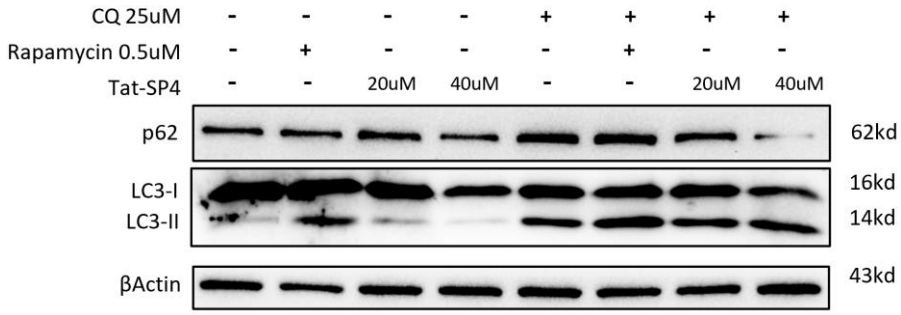

B

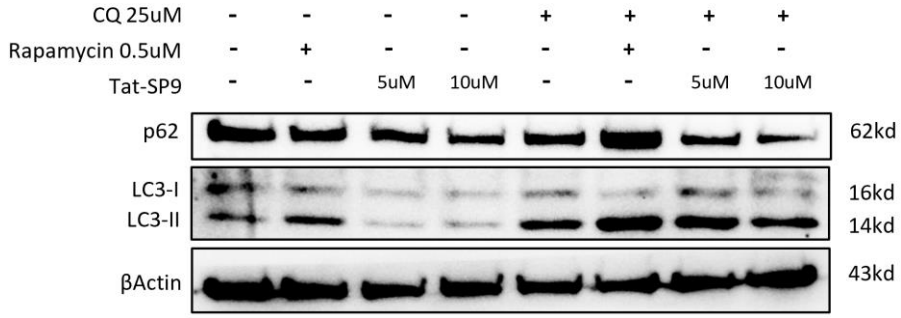

Figure 6.1 Autophagy induction investigation of Tat-SPs in Jurkat e6.1T cells. (A) Western blot analysis of Jurkat e6.1 cells treated with Tat-SP4 in the presence or absence of CQ for 3 hours. (B) Western blot analysis of Jurkat e6.1 cells treated with Tat-SP9 in the presence or absence of CQ for 3 hours.

For comparison, treatment with rapamycin, a well-established autophagy inducer, led to a marked increase in LC3-II levels in Jurkat cells, indicating enhanced autophagosome formation. However, no significant reduction in p62 was observed, suggesting that rapamycin primarily stimulates early-stage autophagy rather than

promoting robust autophagic flux in this cell line. In contrast, Tat-SP treatment did not upregulate LC3-II but did result in a mild reduction of p62, indicating a potential preferential promotion of autophagic flux rather than initiation of early autophagic events in Jurkat e6.1 cells.

It is noteworthy that LC3-I detection was inconsistent in experiments involving Tat-SP9, which may be attributable to suboptimal cell conditions or degradation of long-stored lysate samples. To ensure the reliability of these findings, further optimization of experimental conditions and repeated trials are warranted. Additionally, comprehensive statistical analyses should be conducted to assess the significance of these observations and to elucidate the differential effects of Tat-SPs on autophagy regulation in Jurkat e6.1 T cells.

6.2 Stimulation of interleukin-2 expression during T cell activation

T cell activation was evaluated by measuring interleukin-2 (IL-2) expression, a well-established hallmark of T cell activation. IL-2 production and secretion constitute the third stimulatory signal required for effective T cell activation. To mimic antigen-presenting cell interactions, anti-CD3/CD28 antibody-coated beads were employed as a positive control. Jurkat e6.1 cells were seeded at a density of 1×10^6 cells per 2 mL per well in 6-well plates. Anti-CD3/CD28 beads were added at a 1:1 cell-to-bead ratio according to the manufacturer's protocol. Following treatment with Tat-SPs or

antibodies, total RNA was extracted after 3 hours, and cDNA was synthesized for subsequent real-time PCR analysis. For protein-level assessment, supernatants were collected after 24 hours for ELISA-based quantification of IL-2.

As shown in Figure 6.2A, Tat-SP treatment resulted in a dose-dependent increase in IL-2 secretion into the culture medium, indicating robust T cell activation compared to control groups. Notably, higher concentrations of 50 μM Tat-SP4 and12 μM Tat-SP9 elicited significantly enhanced IL-2 production. Consistent with these findings, IL-2 mRNA expression was also markedly upregulated, as demonstrated in Figure 6.2B. High-dose peptide treatment led to pronounced transcriptional activation, with approximately a fivefold increase in the 50 μM Tat-SP4 group and a fourfold increase in the 12 μM Tat-SP9 group, mirroring the protein-level results observed in the ELISA assay.

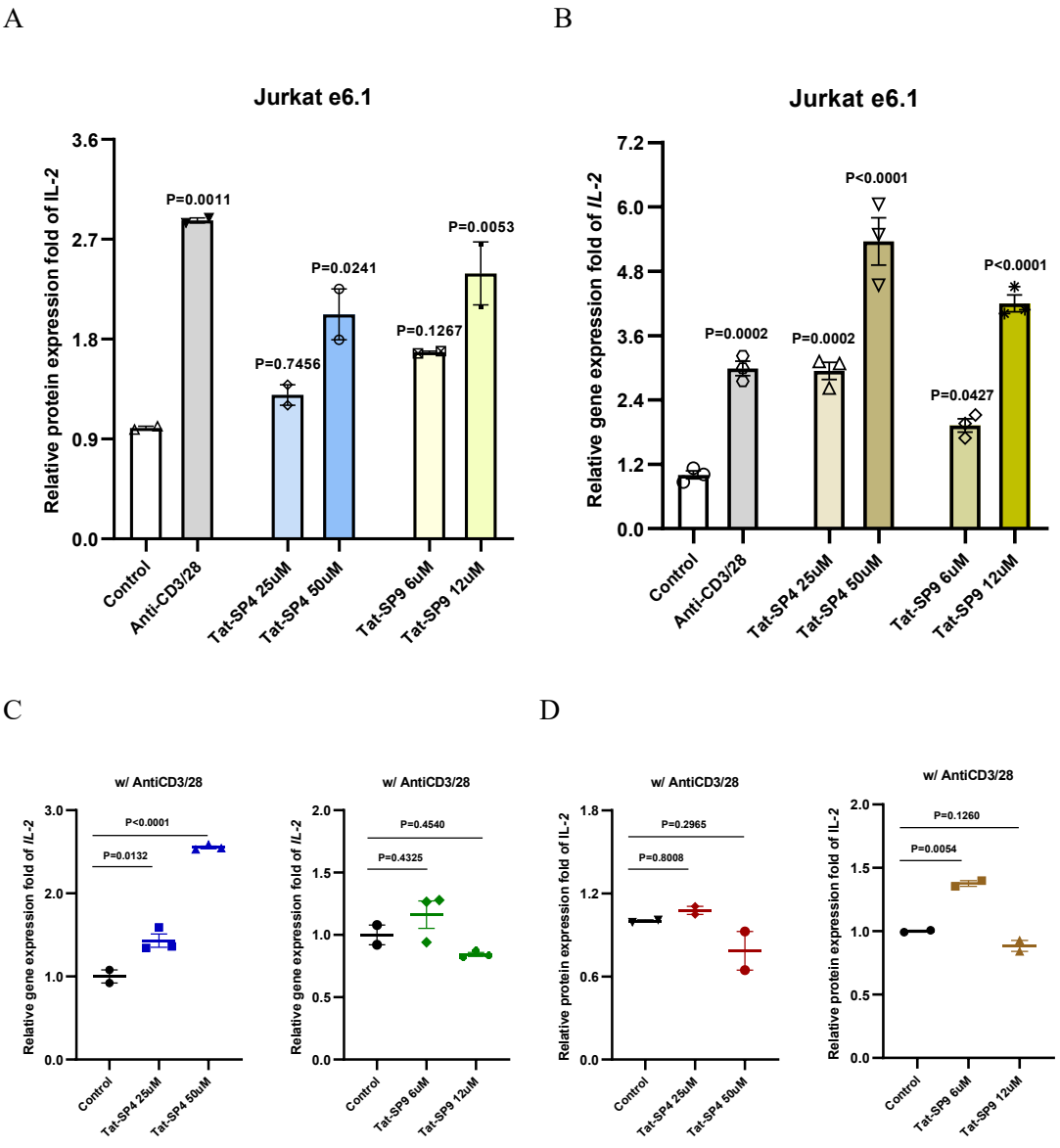

Figure 6.2 Interleukin-2 stimulation by Tat-SPs in T cell activation. (A) IL-2 protein levels in Jurkat e6.1 cell culture supernatants were quantified by ELISA following 24 hours of treatment with Tat-SPs or anti-CD3/CD28 antibody-coated beads. (B) IL-2 mRNA expression was assessed by real-time PCR after 3 hours of Tat-SP treatment. For this analysis, cells were lysed prior to removal of antibody-coated beads. (C) IL-2 mRNA expression was analyzed by real-time PCR after 3 hours of co-treatment with Tat-SPs and anti-CD3/CD28 antibody-coated beads. Cells were lysed before bead

removal. (D) IL-2 protein levels in culture supernatants were measured by ELISA after 24 hours of co-treatment with Tat-SPs and anti-CD3/CD28 antibody-coated beads. Data represent mean ± SEM of replicates. Significance analyzed by Ordinary one-way ANOVA, ∗P < 0.05, ∗∗P < 0.01, ∗∗∗P < 0.001, ∗∗∗∗P < 0.0001.

However, when Tat-SPs were co-administered with anti-CD3/CD28 antibodies, the T cell activation profile became more complex. As shown in Figures 6.2C and D, 50 μM Tat-SP4 further enhanced IL-2 transcriptional activation relative to antibody-only controls, whereas 25 μM Tat-SP4 and both Tat-SP9 treatment groups exhibited minimal additional effects. A modest increase in IL-2 production was observed with 6 μM Tat-SP9, but this effect was not apparent at 12 μM Tat-SP9 or in the lower Tat-SP4 treatment group. Collectively, these findings suggest that, under specific experimental conditions, Tat-SPs may promote T cell activation through a TCR-independent mechanism.

The observed dose-dependent induction of IL-2 by Tat-SPs, at both the transcriptional and protein levels, underscores their capacity to enhance T cell activation. The possibility of Tat-SPs to stimulate T cells independently of TCR engagement has important therapeutic implications, particularly in contexts where TCR signaling is compromised, such as in immunosuppressive tumor microenvironments or chronic infections (Wherry & Kurachi, 2015).

To further substantiate these findings, future studies should assess additional T cell activation markers, such as CD69 and CD25, to provide a more comprehensive understanding of Tat-SP-mediated activation effects. The observed variability in response to different Tat-SP doses and co-treatments also warrants further investigation through detailed dose-response and time-course analyses. Finally, validation of these results in primary human T cells or in vivo models will be essential to establish the translational potential of Tat-SPs as novel immunomodulatory agents.

6.3 Promotion of NFAT1 nuclear translocation in T Cells

In parallel with the assessment of IL-2 activity, we investigated the subcellular localization of nuclear factor of activated T-cells cytoplasmic 2 (NFAT1, also known as NFATc2) in Jurkat e6.1 T cells treated with Tat-SPs. NFAT1 is a pivotal transcription factor that orchestrates the initiation of IL-2 transcription. In resting T cells, NFAT1 resides in the cytoplasm in a phosphorylated state. Upon T cell activation, NFAT1 undergoes dephosphorylation and translocates to the nucleus, where it forms a transcriptional complex to drive the expression of genes such as IL-2.

For these experiments, coverslips were pre-coated with poly-D-lysine and incubated overnight at 4°C in 12-well plates to facilitate cell adherence. Jurkat e6.1 cells were treated with Tat-SPs, or with the positive inducers phorbol 12-myristate 13-acetate (PMA) in combination with ionomycin, in another 12-well plates at a density

of 5×10^5 cells per mL for overnight incubation. On the following day, cells were collected and reseeded onto the coated coverslips, then fixed and subjected to immunofluorescence staining with primary and secondary antibodies. After mounting and drying, confocal microscopy was performed to assess NFAT1 localization.

Confocal imaging revealed efficient nuclear translocation of NFAT1 in Tat-SP-treated Jurkat T cells, as evidenced by the co-localization of NFAT1 immunofluorescence with DAPI-stained nuclei, as presented in Figure 6.3. In contrast, NFAT1 in untreated control cells remained predominantly cytoplasmic. T cells treated with PMA and ionomycin exhibited partial nuclear translocation of NFAT1, with most fluorescence overlapping the nuclear region but lacking the complete nuclear entry observed in a subset of Tat-SP-treated cells.

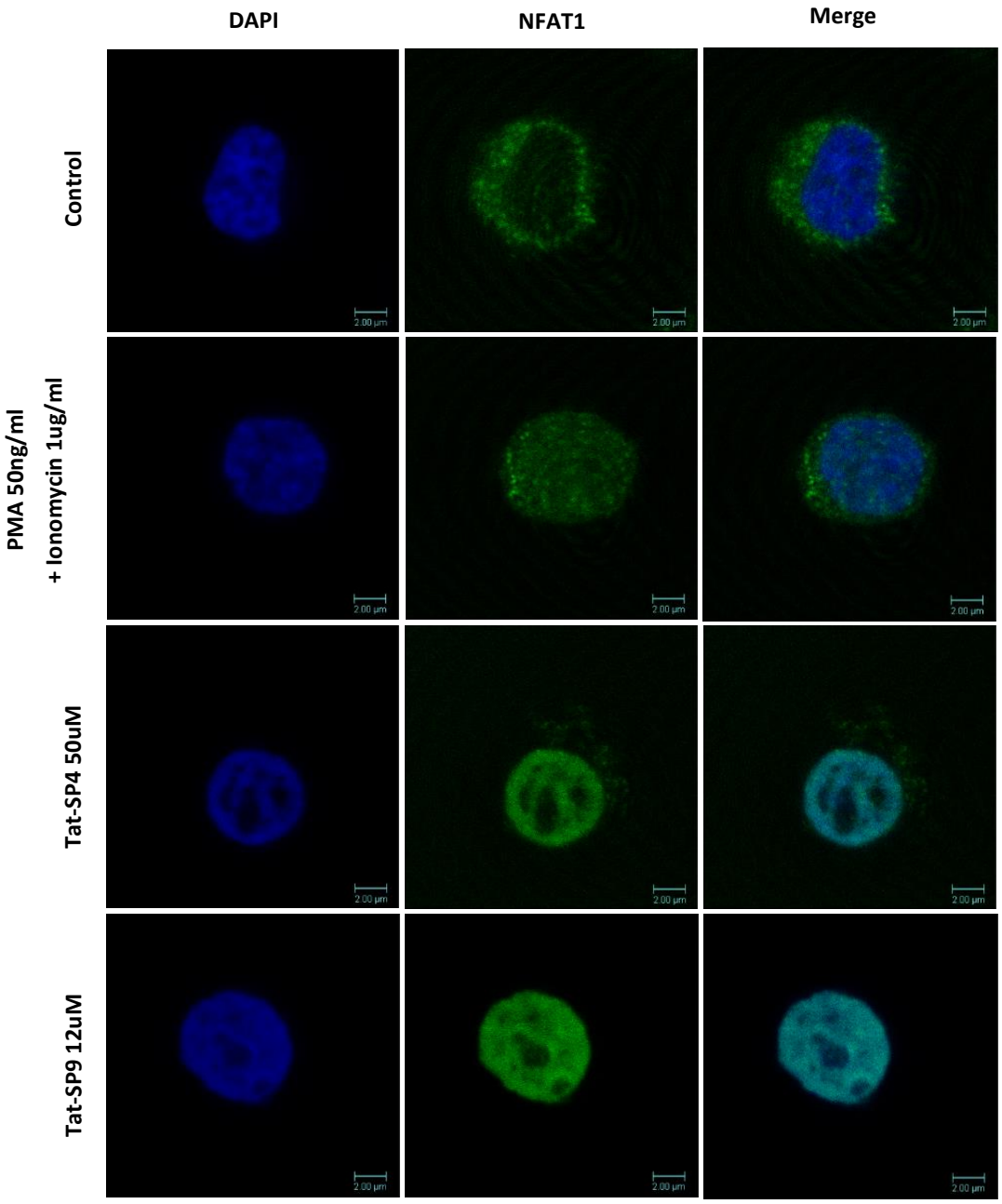

Figure 6.3 NFAT1 translocation induction by Tat-SPs in T cell activation. Subcellular localization of NFAT1 in Jurkat E6.1 T cells following treatment with Tat-SPs or the stimulators PMA and ionomycin. NFAT1 was detected using immunofluorescence (green), and nuclei were counterstained with DAPI (blue). Representative fluorescence images were acquired using confocal microscopy. Scale bar: 2 μm.

In fact, the majority of Tat-SP-treated Jurkat e6.1 cells displayed partial nuclear translocation of NFAT1, a distinct subset exhibited complete nuclear localization, underscoring the potent T cell-activating capacity of Tat-SPs. This pattern contrasts sharply with untreated cells, where NFAT1 localization was almost exclusively cytoplasmic, consistent with the absence of activation signals. The partial translocation observed in the PMA and ionomycin group may be attributable to the duration of treatment or the dynamic nature of NFAT1 shuttling, as this combination mimics TCR signaling by activating protein kinase C (PKC) and increasing intracellular calcium.

To ensure the robustness of these findings, replicate experiments are necessary to confirm NFAT1 translocation in response to Tat-SPs and to exclude the possibility that complete nuclear entry results from cellular stress or protein aggregation. The observed heterogeneity in NFAT1 translocation among Tat-SP-treated cells warrants further investigation to elucidate the factors governing partial versus complete nuclear entry. Dose- and time-dependent studies are particularly important, given the rapid and dynamic shuttling of NFAT1 between the nucleus and cytoplasm in response to various stimuli. Additionally, the genetic complexity of Jurkat e6.1 cells, as a leukemic T cell line, may influence NFAT1 behavior; thus, validation in primary human T cells is recommended to confirm physiological relevance.

Mechanistically, the activation of NFAT1 by Tat-SPs may involve both enhanced

autophagic flux and calcium-dependent pathways, particularly calcineurin-mediated dephosphorylation, which is essential for NFAT1 nuclear translocation. These results provide a mechanistic basis for the observed IL-2 induction and position Tat-SPs as promising candidates for immunomodulatory strategies in anti-AML therapy. Further research is warranted to optimize their application and to elucidate the precise signaling dynamics underlying their effects on T cell activation.

6.4 Enhancement of macrophage phagocytic activity

Phagocytosis is a fundamental process by which antigen-presenting cells, such as macrophages and dendritic cells, eliminate pathogenic threats. This process shares several molecular pathways with autophagy, particularly through the involvement of LC3-related signaling. Additionally, phosphoinositide 3-kinase (PI3K) signaling, which recruits autophagic machinery and promotes phagosome maturation, may further enhance phagocytic activity.

In this study, we evaluated the impact of Tat-SPs on the phagocytic activity of RAW264.7 cells, a murine macrophage cell line. As described in Section 1.2, AML myeloid blasts express "eat me" signals, such as phosphatidylserine, calreticulin, and oxidized phospholipids, which facilitate their recognition by APCs via surface receptors. This recognition initiates phagocytosis, leading to the engulfment and degradation of blasts into tumor-derived peptides, thereby promoting adaptive immune activation

through major histocompatibility complex (MHC) presentation. In Figure 6.4A, Molm13 cells expressing GFP were utilized to visualize phagocytosis, with GFP fluorescence in RAW264.7 macrophages indicating successful engulfment.

A

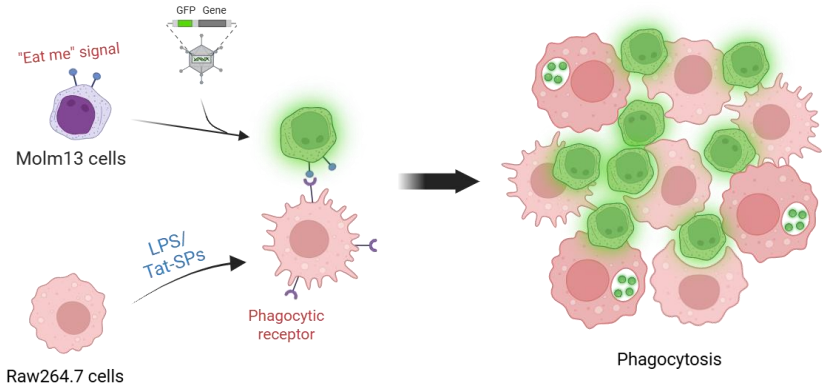

B

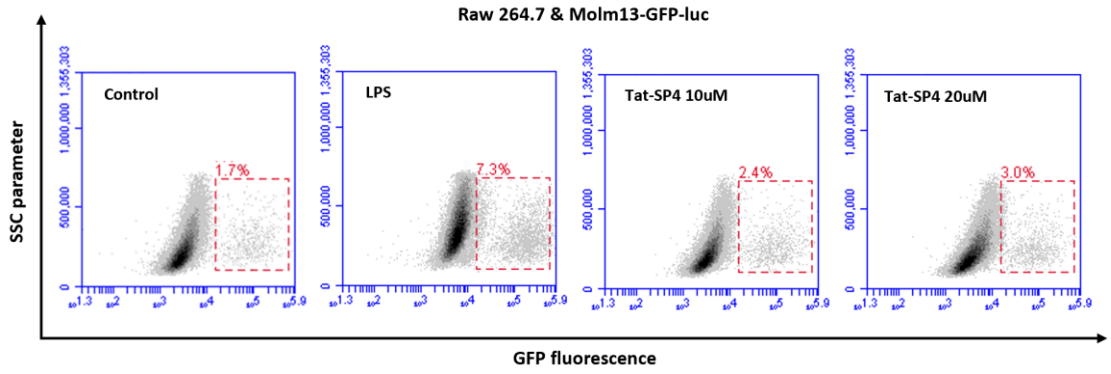

Figure 6.4 Phagocytosis enhancement of Tat-SPs. (A) The mechanistic diagram for phagocytosis assay (B) Flow cytometric analysis of phagocytosis in RAW264.7 cells following priming with LPS or Tat-SP4. The red dotted box indicates the gated GFP-positive population, representing RAW264.7 cells that have engulfed Molm13-GFP-Luc cells. The percentage of GFP-positive cells was calculated to quantify phagocytic

activity.

For these experiments, RAW264.7 macrophages were seeded and allowed to adhere overnight. Cells were then primed with either lipopolysaccharide (LPS) or Tat-SP4 for an additional overnight period before the introduction of Molm13-GFP-Luc cells. On the third day, Molm13-GFP-Luc cells were added at a ratio of one cancer cell to three macrophages for co-culture. Following overnight incubation, all cells were harvested and analyzed by flow cytometry to quantify phagocytosis.

As shown in Figure 6.4B, LPS-primed RAW264.7 cells exhibited a substantial increase in their capacity to engulf Molm13-GFP-Luc cancer cells, with the proportion of GFP-positive macrophages rising from 1.7% in untreated controls to 7.3% following LPS priming. Tat-SP4 treatment also enhanced phagocytosis, albeit to a lesser extent. Specifically, treatment with 10 μM Tat-SP4 increased the engulfed cancer cell population from 1.7% to 2.4%, while 20μM Tat-SP4 further elevated this proportion to 3.0%.

The pronounced effect observed with LPS is consistent with its established role as a potent macrophage activator, inducing pro-inflammatory signaling via Toll-like receptor 4 (TLR4) and upregulating phagocytic machinery. Although Tat-SP4 was less potent than LPS, its dose-dependent enhancement of phagocytosis underscores its capacity to modulate macrophage function, likely through autophagy-related

mechanisms such as AMPK activation or mammalian target of mTOR inhibition, both of which regulate autophagosome formation.

The comparatively modest effect of Tat-SP4 indicates that autophagy enhancement alone may not fully recapitulate the multifaceted activation triggered by LPS, yet it still contributes meaningfully to phagocytosis. This finding highlights the potential of Tat-SP4 as a targeted immunomodulatory agent, particularly in settings where excessive inflammation induced by LPS is undesirable. The ability of Tat-SP4 to enhance the phagocytosis of Molm13-GFP-Luc cells suggests that it may sensitize AML blasts to innate immune surveillance. By promoting the engulfment and subsequent processing of tumor antigens, Tat-SPs may facilitate antigen presentation via MHC complexes, thereby bridging innate and adaptive immunity. Future studies should validate these findings in vivo models to ensure translational relevance.

6.5 Summary

The immunomodulatory potential of Tat-SPs was evidenced by a dose-dependent increase in both IL-2 transcription and secretion, thereby confirming their capacity to activate T cells. This finding was further supported by the observation of nuclear translocation of the transcription factor NFAT1—a hallmark of T cell activation—in a subset of Tat-SP-treated cells, which is consistent with the observed upregulation of IL-2. Beyond their effects on adaptive immunity, Tat-SP4 treatment also enhanced the

phagocytic activity of RAW264.7 macrophages. Relative to untreated controls, Tat-SP4 induced a modest increase in phagocytosis at lower concentrations, with a more pronounced effect at higher concentrations. This enhancement may be attributed to the interplay between phagocytosis and autophagy, highlighting the potential of Beclin-1-targeting peptides as modulators of innate immune responses. The capacity of Tat-SPs to concurrently activate both innate and adaptive immune compartments underscores their promise as novel immunotherapeutic agents.

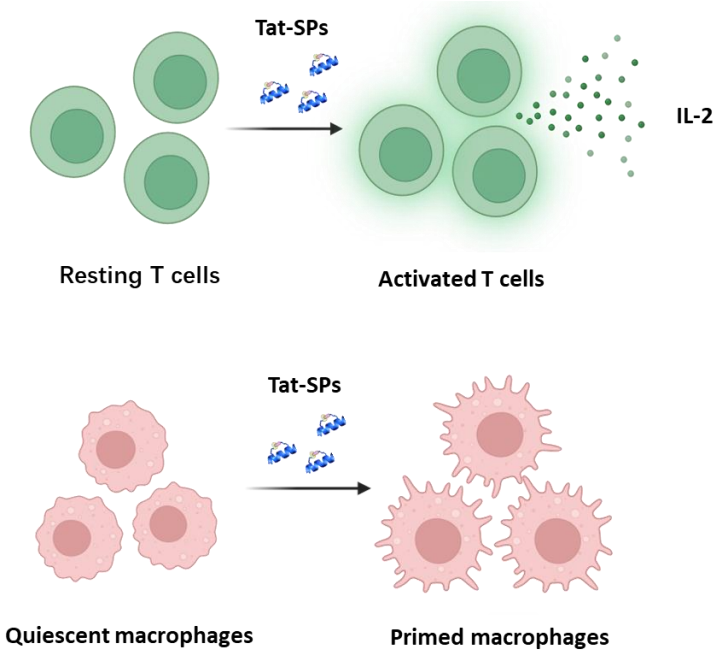

Figure 6.5 Tat-SPs mediate immune priming.

Despite these encouraging findings, the precise molecular mechanisms underlying Tat-SP-induced T cell activation and macrophage phagocytosis remain to be fully elucidated. In Jurkat e6.1 cells, Tat-SPs induced minimal autophagic activity, as evidenced by the lack of significant LC3-II protein accumulation. However, a reduction

in p62 levels was observed in the Tat-SP4-treated group, suggesting a potential increase in autophagic flux. This finding requires further validation to confirm its reproducibility and to clarify the role of autophagy in Tat-SP-mediated immune modulation.

Chapter 7 *In Vivo* therapeutic efficacy and pharmacokinetic profiling of Tat-SPs

7.1 Evaluation of Tat-SP4 anti-Leukemic activity in AML mouse models

The promising in vitro anti-proliferative effects of Tat-SPs prompted us to evaluate their therapeutic efficacy in vivo using AML mouse models. To this end, we established AML xenograft models by implanting Molm13 and Molm13-GFP-Luc cell lines into BALB/c nude mice via both subcutaneous and tail-vein injection routes.

7.1.1 Inhibition of AML tumor growth in murine models

For the subcutaneous xenograft model, one million Molm13 cells suspended in Matrigel were injected into the axillary region of each mouse to induce tumor formation. Treatment with Tat-SPs was initiated once tumors reached an approximate volume of 70 mm^3. In the control group, which received PBS, tumors exhibited rapid progression, reaching an average volume of nearly 1500 mm^3 by day 15 post-treatment, necessitating termination of the experiment in accordance with animal ethics guidelines.

Mice treated with Tat-SPs demonstrated significantly attenuated tumor growth. Both 40 mg/kg Tat-SP4 and 10 mg/kg Tat-SP9 produced comparable inhibitory effects, resulting in approximately 50% reduction in tumor volume relative to controls by the

end of the study, as shown in Figures 7.1A and B. Correspondingly, tumor mass was reduced in both Tat-SP4 and Tat-SP9 treatment groups, as evidenced by decreased tumor weights, although these reductions did not reach statistical significance, in Figure 7.1C. Importantly, no overt toxicity was observed in any treatment group; mice maintained normal behavior and stable body weight throughout the course of Tat-SP4 or Tat-SP9 administration, as presented in Figure 7.1D.

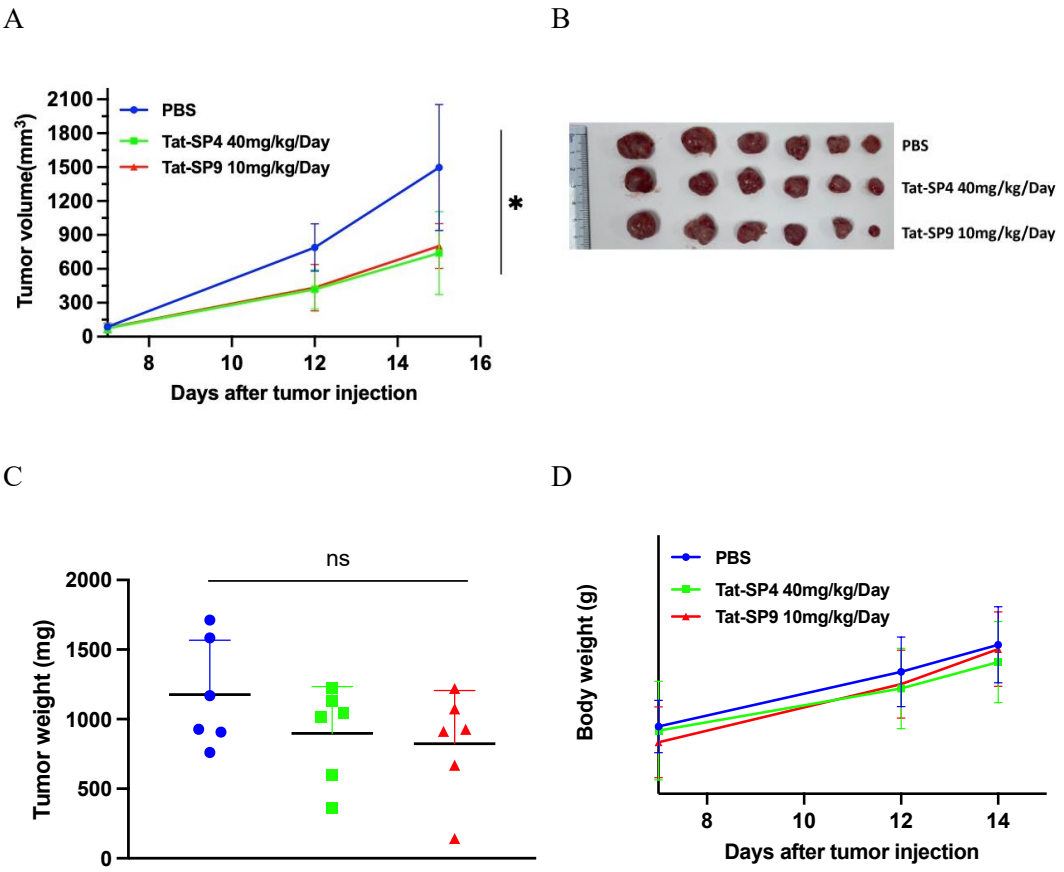

Figure 7.1 Inhibition of tumor growth by Tat-SPs in murine AML xenograft models. (A) Tumor volumes were measured on day 7, 12, and 15 post inoculation for all groups of mice. (B, C) At the conclusion of the experiment, tumor tissues were excised for weighing and photographic documentation. (D) Mouse body weights were

recorded on days 7, 12, and 15 post inoculation all groups of mice. For all groups, drug treatment was conducted once a day with intraperitoneal injection. Data represent mean ± SEM of replicates. Significance analyzed by Two-way ANOVA, $*P < 0.05$.

These results provide foundational evidence for the in vivo anti-AML efficacy of Tat-SPs, demonstrating their capacity to significantly inhibit leukemogenesis in a murine model. Consistent with in vitro findings, Tat-SP9 exhibited superior tumor-suppressive activity compared to Tat-SP4, achieving similar anti-tumor effects at a lower dose, that 10mg/kg for Tat-SP9 exhibit comparable efficacy to 40 mg/kg for Tat-SP4. This observation is in line with the rational design of the second-generation peptide, which features enhanced spatial proximity to Beclin-1, thereby improving its functional potency.

It should be noted, however, that considerable variability was observed in tumor measurements across all groups, as indicated by large error bars. This variability may reflect biological heterogeneity or inconsistencies in tumor measurement. To enhance the reliability of future studies, more frequent monitoring of tumor volumes and the use of a lower initial inoculum of Molm13 cells may help to establish a more controlled tumor microenvironment and better elucidate the dynamics of leukemogenesis.

Furthermore, while subcutaneous xenograft models are widely utilized for evaluating solid tumor growth, their applicability to AML — a hematological

malignancy characterized by diffuse infiltration of the bone marrow and systemic dissemination—may be limited. Such models may not fully recapitulate the complex pathophysiology of AML, which typically presents as a systemic rather than localized disease. Although Tat-SP monotherapy significantly inhibited AML tumor growth in this model, in vitro studies have suggested that combination therapy with chemotherapeutic or targeted agents may further enhance therapeutic efficacy. Future investigations should therefore explore and validate the potential of Tat-SPs in combination regimens using more physiologically relevant in vivo models of AML.

7.1.2 Decrease in leukemia burden following Tat-SP treatment

To more accurately recapitulate the systemic pathology of AML, an intravenous xenograft mouse model was established. The Molm13-GFP-Luc cell line, derived from parental Molm13 cells, was engineered to enable real-time tracking of leukemia progression in vivo via bioluminescence imaging. Molm13-GFP-Luc cells were resuspended in PBS and administered to BALB/c nude mice via tail vein injection. To facilitate engraftment, mice were preconditioned with 150 mg/kg cyclophosphamide for two consecutive days prior to leukemia cell inoculation. Three days post-implantation, mice were randomly assigned to four treatment groups: PBS (vehicle control), Venetoclax (150 mg/kg), Tat-SP4 (40 mg/kg), or a combination of Venetoclax and Tat-SP4. Leukemia burden was monitored longitudinally in each group using luciferase-based bioluminescence imaging.

As shown in Figure 7.2A, by day 15 post-xenograft, leukemia burden had progressed in all groups, with the most aggressive leukemogenesis observed in the control group. In these mice, average luminescence flux increased from 1.01×10^4 photons/sec/cm^2/sr at day 15 to 5.78×10^4 photons/sec/cm^2/sr at day 20, indicating rapid disease progression. In contrast, all treatment groups exhibited suppression of leukemia burden. Venetoclax monotherapy with 150mg/kg provided modest inhibition, reducing the average flux to 4.34×10^4 photons/sec/cm^2/sr .Tat-SP4 monotherapy with dosage of 40mg/kg resulted in substantial inhibition, with an average flux of 1.0×10^4 photons/sec/cm^2/sr. Notably, the combination of Venetoclax and Tat-SP4 further reduced tumor burden, achieving an average flux of 0.72×10^4 photons/sec/cm^2/sr.

A

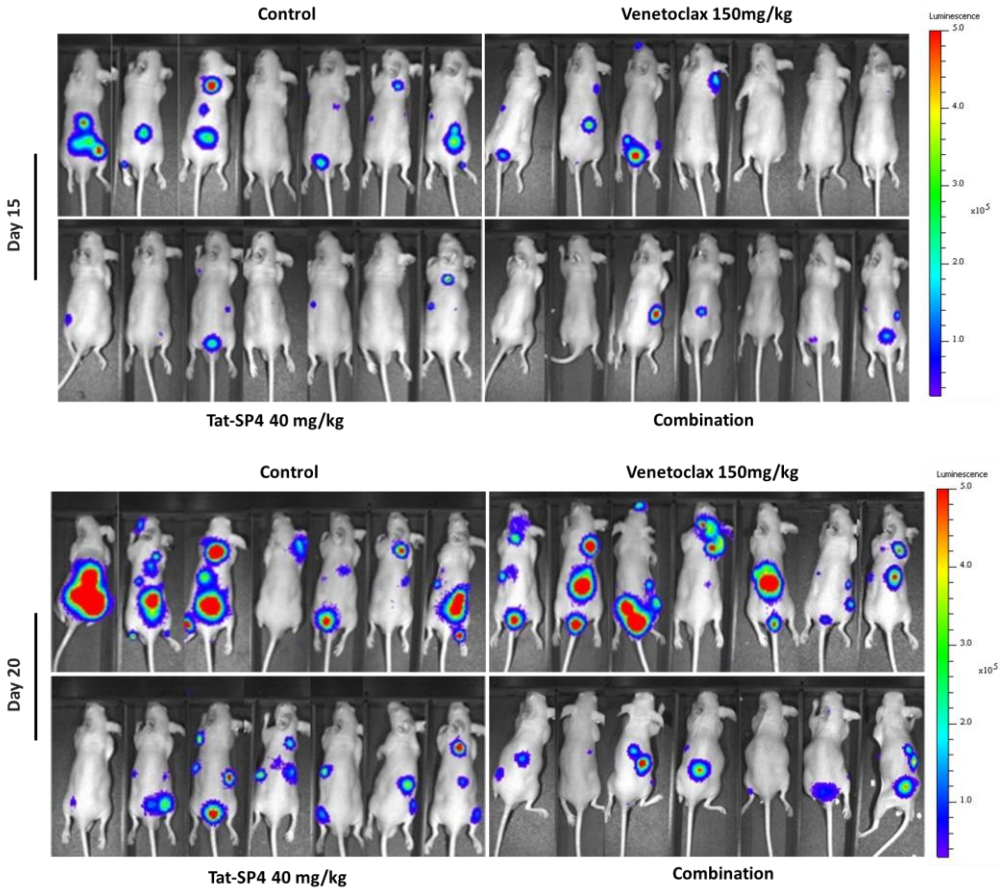

B

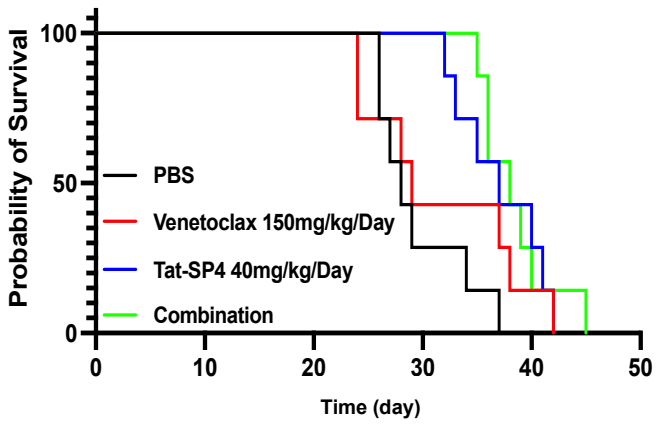

C

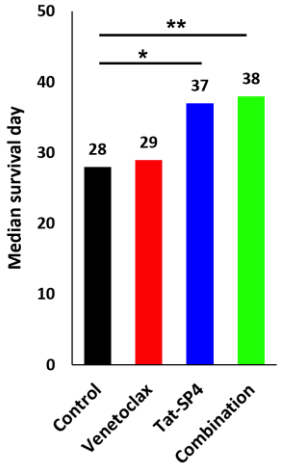

Figure 7.2 Inhibition of leukemia progression by Tat-SP4 and Venetoclax in AML bearing mice. (A) Representative bioluminescence imaging of leukemia burden in

AML-bearing mice at days 15 and 20 post-inoculation, as assessed by the IVIS imaging system. Luminescence flux, quantified as luciferase signal intensity (photons/sec/cm^2 /sr), is displayed using a color scale ranging from 3.00×10^4 to 5.00×10^5. (B) Kaplan-Meier overall survival curves for Molm13-GFP-Luc-bearing mice across different treatment groups. (C) Analysis of median survival days for each treatment group. Statistical significance was determined using the log-rank (Mantel-Cox) test for trend. $*P < 0.05$, $**P < 0.01$.

These results indicate that while Venetoclax alone confers mild anti-leukemic activity, Tat-SP4 at 40 mg/kg is highly effective in suppressing AML progression. Moreover, the combination of Tat-SP4 and Venetoclax provides enhanced therapeutic benefit, suggesting a potential for synergistic interaction and improved survival outcomes in AML mouse models.

Survival analysis further corroborated these findings, as presented in Figures 7.2B and C. All treatment groups demonstrated prolonged survival compared to the control group. However, early mortality was observed in the Venetoclax-only group, likely attributable to Venetoclax-induced toxicity. Median survival analysis revealed that Tat-SP4 monotherapy significantly extended survival, increasing the median survival from 28 days in the control group to 37 days. The combination therapy further improved outcomes, achieving a median survival of 38 days, shown in Figure 7.2C. These data demonstrate that Tat-SP4 alone confers significant survival benefit, and its combination

with Venetoclax can further enhance therapeutic efficacy.

To comprehensively evaluate the in vivo efficacy of Tat-SPs against AML, two distinct mouse models were employed. In the subcutaneous xenograft model, the human AML cell line Molm13, despite its hematological origin, formed solid tumors when injected subcutaneously into nude mice. Inoculation of one million Molm13 cells resulted in tumors reaching approximately 1500 mm^3 within 20 days, underscoring the high malignancy of this cell line. In this context, Tat-SPs demonstrated significant mono-therapeutic efficacy: treatment with 40 mg/kg Tat-SP4 or 10 mg/kg Tat-SP9 reduced tumor volume by nearly 50% and decreased tumor mass, highlighting their potent antiproliferative effects.

In the systemic AML model, Molm13-GFP-Luc cells were injected intravenously following cyclophosphamide preconditioning to suppress host immune responses and facilitate engraftment. This model enabled dynamic tracking of leukemogenesis via bioluminescence imaging, analogous to tumor volume measurements in the subcutaneous model. Tat-SP4 significantly inhibited leukemia progression and extended survival, supporting its potential as an effective antiproliferative therapy for AML. Furthermore, combination therapy with Venetoclax and Tat-SP4 yielded superior survival outcomes compared to either agent alone, suggesting a synergistic therapeutic effect. The molecular mechanisms underlying this synergy warrant further investigation.

It is noteworthy that previous attempts to model AML in severely immunocompromised mice, such as NOD-SCID or B-NDG (NOD-SCID with *Il2rg* gene deletion), failed to demonstrate the anti-AML efficacy of Tat-SPs. In contrast, the positive outcomes observed in nude mice—which retain partial immune function—suggest that immune responses may contribute to the therapeutic effects of Tat-SPs. This hypothesis is further supported by in vitro data demonstrating that Tat-SPs enhance T cell activation and macrophage phagocytosis. These findings advocate for future studies in immunocompetent mouse models, where more robust anti-AML effects may be observed, particularly in combination with immunotherapeutic agents such as anti-PD-1 or anti-PD-L1 antibodies.

7.2 Pharmacokinetic characterization of Tat-SP4

In-vivo pharmacokinetic studies of Tat-SPs were performed to elucidate their systemic behavior following administration. Healthy, non-tumor-bearing C57BL/6 mice received intraperitoneal injections of Tat-SP4 at a dose of 40mg/kg via intraperitoneal injection. Plasma samples were collected at multiple time points before and after administration of 0, 5, 15, 30, 60, 120, 240, and 480 minutes. To ensure accurate quantification and minimize interference from endogenous proteins and matrix components, plasma samples underwent urea denaturation and trichloroacetic acid (TCA) precipitation, followed by organic solvent extraction. The resulting extracts were freeze-dried and stored at −80°C prior to quantitative analysis by mass

spectrometry.

As shown in Figure 7.3, Tat-SP4 exhibited rapid systemic absorption following intraperitoneal administration, reaching peak plasma concentrations around 3.90 μM within 5 minutes, indicative of efficient uptake from the peritoneal cavity into the circulation. The subsequent decline to 2.94 μM at 15 minutes suggests a rapid distribution phase, during which Tat-SP4 is likely redistributed from plasma to peripheral tissues. From 15 minutes to 1 hour, the slower decrease in plasma concentration likely reflects the establishment of a distribution equilibrium between plasma and tissue compartments. After 1 hour, a more pronounced decline was observed, consistent with the initiation of metabolic clearance and/or renal excretion. Tat-SP4 remained detectable at 2.05 μM at 2 hours and 1.52 μM at 4 hours post-administration, indicating a moderate volume of distribution and sustained systemic exposure. By 8 hours, Tat-SP4 was no longer detectable in plasma, suggesting complete clearance or metabolic conversion within this timeframe.

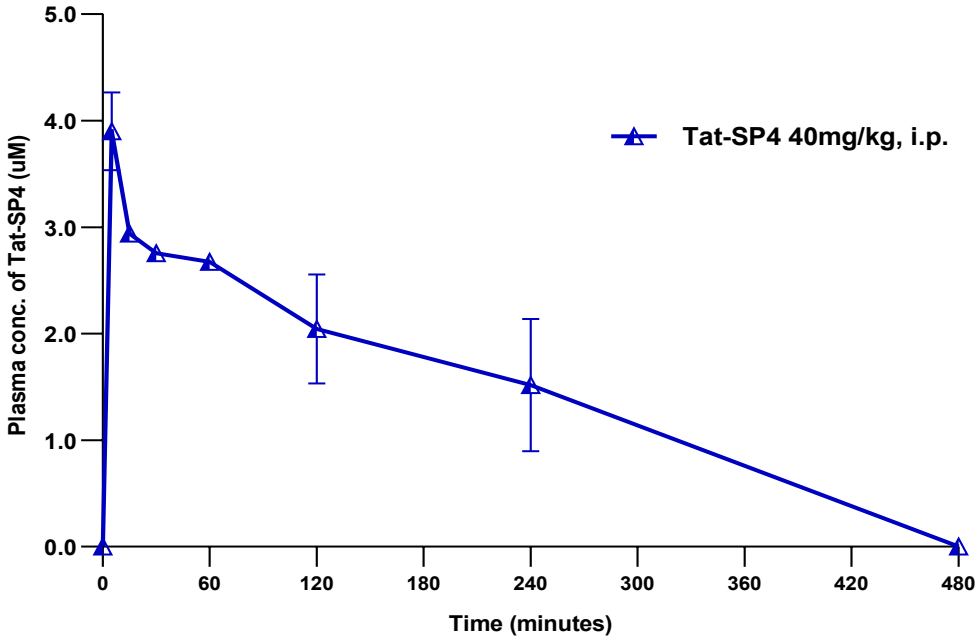

Figure 7.3 Quantitative Analysis of Tat-SP4 in Mouse Plasma Following 40mg/kg administration. Plasma samples were collected from mice at designated time points post-exposure to Tat-SP4 and analyzed using liquid chromatography-tandem mass spectrometry (LC-MS/MS). Data represent mean ± SEM of biological replicates.

These data characterize the pharmacokinetic profile of Tat-SP4 as exhibiting rapid absorption and distribution within the first 15 minutes post-administration. While intraperitoneal administration is generally associated with high bioavailability, the absence of comparative data from alternative administration routes precludes definitive quantification. Additionally, the lack of tissue concentration measurements limits the ability to elucidate specific metabolic or excretory pathways, underscoring the need for further studies to establish a comprehensive ADME profile for Tat-SP4 in vivo.

The pharmacokinetic parameters of Tat-SP4 at a 40mg/kg dose were determined using noncompartmental analysis (NCA) with WinNonlin software. NCA is a model-independent method widely employed in preclinical pharmacokinetic studies due to its computational efficiency and minimal assumptions regarding drug disposition. Unlike compartmental analysis, which requires predefined physiological models, NCA utilizes statistical moments of the concentration–time curve to directly estimate key pharmacokinetic parameters, including area under the curve (AUC), maximum plasma concentration (Cmax), time to maximum concentration (Tmax), elimination half-life ($T_{1/2}$), volume of distribution (Vz), and clearance (CL). This approach is particularly advantageous in early-stage drug development when the complexity of drug kinetics may not be fully elucidated. The pharmacokinetic parameters obtained from NCA are summarized in Table 7.1.

Table 7.1, Pharmacokinetic parameters of Tat-SP4 in mice.

Pharmacokinetic Parameters	40mg/kg
Tmax (min)	5.00 ± 0.00
Cmax (μg/ml)	13.6 ±2.84
AUCINF_obs (min·μg/ml)	14917 ±5935
AUCINF_D_obs (min·kg·μg/ml/mg)	372.9 ±148
Vz_F_obs (ml/kg)	3999 ±97.5
Cl_F_obs (ml/min/kg)	3.62 ±2.98
T half (min)	9.85 ±0.901

Note: Data are presented as mean ± SD and were analyzed using NCA with Phoenix WinNonlin version 8.0. Cmax values were entered in micrograms per milliliter (μg/mL), as required by the WinNonlin system, following conversion from the original raw data reported in micromolar (μM).

The fitted pharmacokinetic profiles demonstrated that both Tmax and Cmax were consistent with the observed concentration–time data. At a 40 mg/kg dose, Tmax was 5 minutes, confirming rapid systemic absorption following intraperitoneal administration. The elimination half-life ($T_{1/2}$) of Tat-SP4 was approximately 9.85 minutes, which is comparable to the short half-lives reported for many peptide therapeutics. The Cmax of Tat-SP4 was approximately 13.6 μg/mL (~3.90 μM), as observed in the concentration–time curve. The area under the curve (AUC), a key

indicator of overall drug exposure, was calculated to be approximately 14,917 min·μg/mL. This parameter can be utilized to estimate bioavailability when compared with AUC values obtained from alternative administration routes, such as intravenous injection.

The observed volume of distribution (Vz_F_obs) was 3,999 mL/kg, which is relatively large for a peptide. Given that extracellular fluid volume in mammals is approximately 20% of body weight (Hall, J.E., 2011), this suggests that Tat-SP4 distributes into tissues or potentially intracellular compartments, consistent with its cell-penetrating properties. However, such distribution may also increase the risk of off-target effects. The observed clearance (Cl_F_obs) was 3.62 mL/min/kg, which is moderate for a peptide and substantially lower than hepatic (~60 mL/min/kg) or renal (~43 mL/min/kg) blood flow in mice (Hall et al., 2012). This indicates that Tat-SP4 is not rapidly cleared from systemic circulation and is likely eliminated via enzymatic degradation rather than by rapid hepatic clearance.

Some discrepancies were noted between pharmacokinetic parameters estimated by the NCA model and those visually apparent from the concentration–time profiles. Specifically, the $T_{1/2}$ calculated for the 40mg/kg dose was shorter than suggested by the empirical data. This may be attributed to inter-individual variability, as free peptide was undetectable in one mouse at the 2-hour time point and in two mice at 4 hours. Such variability can introduce significant error into pharmacokinetic analyses and obscure

true drug disposition patterns. Additionally, the default NCA approach calculates half-life based on the terminal phase using the last few data points, which may not accurately reflect the overall elimination kinetics observed in the concentration–time curve.

To address these limitations, further optimization of the experimental protocol is warranted, including increasing the number of animals per group to reduce biological variability and exploring alternative analytical models for a more comprehensive assessment of Tat-SP4 pharmacokinetics. Despite these limitations, the current data provide valuable initial insights into the *in vivo* pharmacokinetic behavior of Tat-SP4.

7.3 Summary

The therapeutic efficacy of Tat-SP peptides was systematically evaluated in two distinct AML mouse models. In a subcutaneous tumor growth assay utilizing the Molm13 cell line, the robust formation of solid tumors highlighted the aggressive and metastatic nature of this AML model. Treatment with both 40 mg/kg Tat-SP4 and 10 mg/kg Tat-SP9 resulted in significant inhibition of tumor progression, as demonstrated by marked reductions in both tumor volume and weight relative to controls. These results provide compelling evidence for the anti-leukemic activity of both peptides in vivo.

Further assessment in a systemic AML model revealed that Tat-SP4 monotherapy

with dosage of 40 mg/kg significantly reduced leukemic burden and prolonged overall survival compared to vehicle-treated controls, thereby reinforcing its therapeutic potential. Notably, combination therapy with Venetoclax with 150 mg/kg further potentiated the anti-AML effects of Tat-SP4, suggesting synergistic or additive interactions and supporting the broader applicability of Tat-SP4 in combination regimens for AML treatment.

Given the immunodeficient status of nude mouse models, which may limit the assessment of immune-mediated effects, future studies will employ immunocompetent mouse models to validate these findings and better recapitulate the clinical scenario. In parallel, mechanistic investigations are warranted to elucidate the molecular pathways underlying the observed therapeutic effects, which will inform the rational design of optimized treatment strategies and facilitate the mitigation of potential toxicities, thereby advancing clinical translation.

Pharmacokinetic analysis of Tat-SP4 at a 40mg/kg dose demonstrated rapid systemic absorption, with Cmax of 3.9 μM achieved within 5 minutes post-injection. Tat-SP4 remained detectable in plasma at approximately 2 μM up to 2 hours after administration. The observed clearance (Cl_F_obs) was 3.62 mL/min/kg, and the volume of distribution (Vz_F_obs) was 3,999 mL/kg, suggesting extensive tissue distribution and moderate elimination. However, LC-MS/MS quantification revealed relatively low levels of free Tat-SP4 in plasma, highlighting challenges in accurately

characterizing its pharmacokinetic profile. While these preliminary concentration–time data provide valuable initial insights, further comprehensive studies are necessary to fully elucidate the absorption, distribution, metabolism, and elimination (ADME) properties of Tat-SP4.

To address these limitations, future studies should incorporate intravenous administration to establish a complete elimination profile and determine the absolute bioavailability of Tat-SP4. Additionally, strategies to optimize the pharmacological properties of Tat-SP peptides may include antibody conjugation to enhance target specificity and stability, such as PEGylation or encapsulation in liposomal formulations

.

Chapter 8 Discussion

Acute myeloid leukemia is the most aggressive form of leukemia, with a five-year survival rate of only 32%. Despite the introduction of several new FDA-approved therapies since 2017, the clinical management of AML remains challenging due to cytogenetic heterogeneity, frequent relapse, and the emergence of drug resistance. These persistent obstacles underscore the urgent need for more effective and innovative therapeutic strategies for AML. In this project, we developed a Beclin-1-targeting peptide that exhibited potent anti-proliferative activity and induced mitochondrial dysfunction in AML cell lines. The therapeutic efficacy of this peptide was further validated in vivo, as evidenced by reduced leukemia progression and improved survival in AML mouse models.

Beclin-1 is a scaffold protein within the PI3KC3 complex, interacting with partners such as UVRAG and Atg14L via its coiled-coil domain to form distinct PI3KC3 complexes essential for autophagy and endolysosomal degradation. Our previous structural analyses demonstrated that UVRAG-Beclin-1 heterodimerization outcompetes Atg14L binding through a combination of hydrophobic and electrostatic interactions. Building on these insights, we designed hydrocarbon-stapled peptides targeting the C-terminal coiled-coil domain of Beclin-1 to disrupt its homodimerization and enhance its interactions with UVRAG and Atg14L. Incorporation of a Tat sequence facilitated efficient cellular uptake, and the peptide's ability to promote autophagic flux

and EGFR degradation in cancer cells was previously validated (Wu et al., 2018).

Notably, the Tat-Beclin-1 peptide developed by Levine and colleagues enhances autophagy by binding to the negative regulator GAPR-1, thereby promoting LC3 lipidation (Liu et al., 2013). In contrast, our Tat-SP peptides potentiate Beclin-1's interactions with UVRAG and Atg14L by inhibiting its self-association, thus promoting autophagy-related processes. Both Tat-SP peptides and Tat-Beclin-1 induce autosis, a unique form of cell death characterized by necrotic features such as plasma membrane rupture, loss of cellular integrity, and release of intracellular contents. Although the precise mechanisms underlying autosis remain incompletely understood, this process can be inhibited by Digoxin, a Na^+/K^+-ATPase inhibitor. Both peptides exhibit cytotoxicity in cancer cells, which is reversible by Digoxin. Importantly, other forms of programmed cell death—including apoptosis, ferroptosis, necroptosis, and pyroptosis—were excluded as contributors to Tat-SP-induced cytotoxicity, as inhibitors of these pathways failed to rescue treated cells.

Autosis is thought to be triggered by excessive autophagic stress, and the autophagosome formation inhibitor 3-MA significantly attenuated Tat-SP-induced cell death. Together with the observation that Digoxin also prevents Tat-SP-induced cytotoxicity, these findings indicate that autophagy is essential for the cytotoxic effects of Tat-SPs. However, only minimal autophagic activity was detected, with modest LC3 lipidation and clear p62 degradation observed by Western blot. This may reflect

technical limitations, and future studies will optimize assay conditions, including the use of positive controls and varied experimental parameters, to draw more definitive conclusions.

A prominent feature of Tat-SPs is their profound disruption of mitochondrial function in AML cells. Mitochondria are central to cellular energy production and metabolic regulation, and their importance in AML is underscored by proteomic studies revealing upregulation of mitochondrial proteins and the fact that four of the eleven FDA-approved AML drugs in the past decade target mitochondrial pathways. In this study, both Tat-SP4 and Tat-SP9 induced marked mitochondrial dysfunction in AML blasts, as evidenced by loss of mitochondrial membrane potential, increased ROS production, activation of the MPTP, and suppression of both basal and maximal OXPHOS. These findings suggest that Tat-SPs act as potent cytotoxins against AML blasts, with mitochondrial-dependent stress—such as energy disruption and activation of cell death signaling—likely playing a key role in autotic cell death.

The precise mechanism by which Tat-SPs induce mitochondrial dysfunction remains to be fully elucidated. Their cationic nature may facilitate accumulation within the negatively charged mitochondrial matrix (membrane potential ~ -180 mV; Giorgi et al., 2018), potentially disrupting ion gradients, impairing the respiratory chain, and increasing ROS production, ultimately leading to MPTP activation. Notably, cell death induced by Tat-SPs could be mitigated by exogenous calcium supplementation,

suggesting that calcium may either impede Tat-SP cellular entry or modulate ion signaling and compensatory pathways.

Co-administration of Tat-SPs with intracellular calcium regulators provided further mechanistic insights. The cytosolic calcium chelator BAPTA partially reversed the protective effect of calcium, indicating that cytosolic calcium dynamics modulate Tat-SP toxicity. Thapsigargin, an inhibitor of the SERCA, elevates cytosolic and mitochondrial calcium levels and significantly reduced Tat-SP-induced cytotoxicity. Pretreatment with RU360, an inhibitor of the MCU, blocked mitochondrial calcium uptake and abrogated the protective effect of exogenous calcium. These results suggest that mitochondrial calcium uptake is pivotal in mediating Tat-SP cytotoxicity and may underlie the observed mitochondrial dysfunction in AML cells. Additionally, Digoxin, by inhibiting Na^+/K^+-ATPase and thereby increasing cytosolic calcium via the Na^+/Ca^{2+} exchanger (NCX), also mitigated Tat-SP toxicity, further highlighting the central role of calcium signaling in modulating cellular responses to Tat-SPs.

It is important to note that the pharmacological inhibitors used in these studies may have off-target effects in complex cellular environments. To address this, future studies should employ genetic approaches, such as CRISPR-mediated knockout of MCU, to definitively assess the role of mitochondrial calcium uptake in Tat-SP-induced cytotoxicity. Further exploration of the interplay between calcium signaling and autophagic cell death pathways, including the interaction between Beclin-1 and IP3R,

may provide additional mechanistic insights. Moreover, the potential contributions of lysosomes and the Golgi apparatus, which serve as auxiliary calcium stores, to Tat-SP-induced cytosolic calcium fluctuations warrant further investigation.

Tat-SPs, which incorporate a TAT sequence to facilitate cellular uptake, are believed to enter cells primarily via macropinocytosis. This non-selective endocytic process allows extracellular fluids, including ions, to enter cells and may influence intracellular calcium homeostasis. Calcium-dependent signaling pathways involved in macropinocytosis could also contribute to Tat-SP-induced cell death. Collectively, these findings suggest that calcium dysregulation integrates autophagy, ER stress, and mitochondrial dysfunction, forming a complex network that drives Tat-SP cytotoxicity in AML cells.

Tat-SPs also demonstrated notable immunomodulatory properties. In cancer cells, Tat-SP-induced autotic cell death was immunogenic, as evidenced by the release of extracellular ATP and HMGB1, which promote APCs maturation and activation of innate immunity, thereby facilitating AML blast clearance. Furthermore, Tat-SPs induced NFAT1 nuclear translocation and dose-dependent IL-2 production at both transcriptional and protein levels. Enhanced phagocytosis was observed in RAW264.7 macrophages following Tat-SP priming, further highlighting the immunostimulatory potential of Tat-SPs in anti-AML therapy.

While enhanced phagocytosis may result from crosstalk between autophagy and phagocytosis—given the shared involvement of PI3K complex members in autophagosome and phagosome formation—the mechanism of T cell activation appears more complex. Tat-SPs activated Jurkat e6.1 T cells independently of anti-CD3/CD28 co-stimulation, as co-application with these antibodies further augment activation only in some concentrations. This indicates that Tat-SPs may function as standalone immune activators, particularly in contexts of impaired TCR stimulation. NFAT1 translocation, mediated by calcineurin-dependent dephosphorylation and nuclear import in response to elevated cytosolic calcium, further supports the involvement of calcium-regulated, calcineurin-dependent pathways in Tat-SP-induced T cell activation. However, the magnitude of T cell activation in Jurkat e6.1 cells was modest compared to physiological responses in healthy T cells, where IL-2 production can increase by several orders of magnitude upon activation, as observed in PBMCs (Sundrud et al., 2004).

The immunostimulatory effects of Tat-SPs likely contribute to their efficacy in Balb/c nude mice, which retain innate immune function, but not in B-NDG or NOD/SCID models, which are profoundly immunodeficient. These findings suggest that Tat-SPs could synergize with immune checkpoint inhibitors, such as PD-1/PD-L1 antagonists, to enhance T cell-mediated anti-AML responses, underscoring the critical role of the immune system in mediating their therapeutic effects.

The therapeutic application of Tat-SPs was further explored in combination with FDA-approved first-line therapies. Both chemotherapeutic and targeted agents, such as AraC and Venetoclax, exhibited enhanced anti-proliferative effects when combined with Tat-SPs in vitro. The synergistic cytotoxicity, particularly with Venetoclax, was confirmed in AML mouse models. In AML xenografts using Molm13-GFP-luc cells, Tat-SP4 monotherapy significantly suppressed leukemia progression and extended survival, while combination therapy with Venetoclax produced superior anti-AML effects. In a subcutaneous Molm13 model, untreated mice exhibited rapid tumor growth, whereas Tat-SP treatment significantly reduced tumor size and mass, further substantiating their anti-AML efficacy.

Importantly, in *FLT3-ITD*-mutated AML models—a major mutation presents in the Molm13 cell line—Tat-SP4 demonstrated robust efficacy both as a monotherapy and in combination with Venetoclax, suggesting potential therapeutic benefit for the approximately one-third of AML patients harboring this mutation. To enhance translational relevance, future studies will utilize immunocompetent mouse models, such as those employing the murine AML cell line C1498 (Ruzicka et al., 2020; Chen et al., 2024), to determine whether intact immune responses further potentiate the anti-AML effects of Tat-SPs.

In the final phase of this study, the pharmacokinetics of Tat-SP4 were characterized following intraperitoneal administration at a dose of 40 mg/kg in mouse.

The plasma concentration–time profile revealed rapid absorption, followed by a biphasic distribution pattern. An initial rapid decline in plasma concentration was observed, decreasing from 3.9 μM to 2.94 μM within the first 15 minutes, indicative of a fast distribution phase. This was followed by a slower decline between 15 minutes and 1 hour post-administration, with plasma concentrations reaching 2.68 μM. The fitted volume of distribution (Vz_F_obs), as determined by WinNonlin, suggests extensive tissue distribution, consistent with the known cell-penetrating properties of Tat-SP4. This extensive distribution likely contributes to the relatively low observed clearance (Cl_F_obs), as a significant proportion of the peptide is rapidly sequestered in tissues rather than remaining in the systemic circulation.

It is noteworthy that the free peptide concentrations detected in plasma were lower than the effective concentrations observed in cell-based assays; while the Cmax of Tat-SP4 was approximately 3.9 μM, the IC_{50} for AML cell cytotoxicity was around 20 μM or higher. The relatively low systemic exposure may be due to binding or conjugation to plasma proteins, resulting in reduced levels of free Tat-SP4 in circulation. Although direct comparisons between in vivo and in vitro systems are inherently limited, future studies will focus on optimizing plasma sample preparation and LC-MS conditions to improve the detection of free peptide.

While a comprehensive ADME profile and absolute bioavailability for various administration routes remain to be established, these preliminary results highlight the

need for pharmacokinetic optimization to enhance the drug-like properties of Tat-SPs. Notably, the second-generation peptide Tat-SP9 exhibited superior anti-AML efficacy and T cell activation both in vitro and in vivo, achieving comparable effects at lower doses relative to Tat-SP4. This validates the success of stapling position optimization in improving therapeutic performance and underscores the potential of our Beclin-1 stapling strategy as a robust platform for peptide drug design. However, the pharmacokinetic profile of Tat-SP9 remains to be determined and may differ from that of Tat-SP4. Future strategies will explore peptide structure modifications, optimized formulations, and antibody conjugation to improve in vivo delivery and therapeutic efficacy.

In summary, Tat-SPs represent a promising new class of therapeutics for AML, integrating autosis induction, mitochondrial disruption, and immune activation into a multifaceted anti-leukemic strategy. Their preclinical efficacy, particularly in combination with Venetoclax, and their capacity to harness the immune system, offer hope for more effective and durable AML treatments. By overcoming pharmacokinetic challenges and elucidating underlying mechanisms, Tat-SPs have the potential to redefine AML therapy and improve patient outcomes. This study lays the groundwork for future translational research and clinical development, opening new avenues for the treatment of AML and related malignancies.

Reference

A. Rad and M. Häggström, CC-BY-SA 3.0 license. Simplified hematopoiesis. 2009. https://en.m.wikipedia.org/wiki/File:Hematopoiesis_simple.svg

International Agency for Research on Cancer. (2022). Global cancer observatory: Cancer today. World Health Organization. Retrieved from https://gco.iarc.fr/today.

Zhang, N., Wu, J., Wang, Q. *et al.* Global burden of hematologic malignancies and evolution patterns over the past 30 years. *Blood Cancer J.* **13**, 82 (2023). https://doi.org/10.1038/s41408-023-00853-3

National Cancer Institute. (2022). *Surveillance, Epidemiology, and End Results (SEER) Program*. SEER Cancer Statistics Review. Retrieved from https://seer.cancer.gov

Bispo, J.A.B., Pinheiro, P.S., Kobetz, E.K., 2020. Epidemiology and Etiology of Leukemia and Lymphoma. Cold Spring Harbor Perspectives in Medicine 10, a034819.. https://doi.org/10.1101/cshperspect.a034819

Padmakumar, D., Chandraprabha, V. R., Gopinath, P., Vimala Devi, A. R. T., Raj John Anitha, G., Sreelatha, M. M., Padmakumar, A., & Sreedharan, H. (2021). A concise review on the molecular genetics of acute myeloid leukemia. *Leukemia Research, 111*, 106727. https://doi.org/10.1016/j.leukres.2021.106727

Leukemia & Lymphoma Society. (2023). Acute myeloid leukemia in adults. https://www.lls.org

Wakui, M., Kuriyama, K., Miyazaki, Y., Hata, T., Taniwaki, M., Ohtake, S., Sakamaki, H., Miyawaki, S., Naoe, T., Ohno, R., & Tomonaga, M. (2008). Diagnosis of acute myeloid leukemia according to the WHO classification in the Japan Adult Leukemia Study Group AML-97 protocol. *International journal of hematology*, *87*(2), 144–151. https://doi.org/10.1007/s12185-008-0025-3

Papaemmanuil, E., Gerstung, M., & Bullinger, L. (2016). Genomic classification and prognosis in acute myeloid leukemia. New England Journal of Medicine, 374(23), 2209–2221. https://doi.org/10.1056/NEJMoa1516192

Khoury, J.D., Solary, E., Abla, O. *et al.* The 5th edition of the World Health Organization Classification of Haematolymphoid Tumours: Myeloid and Histiocytic/Dendritic Neoplasms. *Leukemia* **36**, 1703–1719 (2022). https://doi.org/10.1038/s41375-022-01613-1

Ranieri, R., Pianigiani, G., Sciabolacci, S. *et al.* Current status and future perspectives in targeted therapy of *NPM1*-mutated AML. *Leukemia* **36**, 2351–2367 (2022). https://doi.org/10.1038/s41375-022-01666-2

Falini, B., Brunetti, L., Sportoletti, P., & Martelli, M. P.. (2020). NPM1-mutated acute myeloid leukemia: from bench to bedside. *Blood Journal*, *136*(15), 1707–1721. https://doi.org/10.1182/blood.2019004226

Daver, N., Schlenk, R. F., Russell, N. H., & Levis, M. J.. (2019). Targeting FLT3 mutations in AML: review of current knowledge and evidence. *Leukemia*, *33*(2), 299–312. https://doi.org/10.1038/s41375-018-0357-9

Kayser, S., & Levis, M. J. (2023). The clinical impact of the molecular landscape of

acute myeloid leukemia. *Haematologica, 108*(2), 202–218. https://doi.org/10.3324/haematol.2022.280801

Shah, M., & Licht, J. (2011). DNMT3A mutations in acute myeloid leukemia. Nature Genetics, 43(4), 289–290. https://doi.org/10.1038/ng0411-289

Lauber, C., Correia, N., Trumpp, A., & et al. (2020). Survival differences and associated molecular signatures of DNMT3A-mutant acute myeloid leukemia patients. Scientific Reports, 10, 12761. https://doi.org/10.1038/s41598-020-69691-8

Issa, G. C., & Dinardo, C. D.. (2021). Acute myeloid leukemia with IDH1 and IDH2 mutations: 2021 treatment algorithm. *Blood Cancer Journal*, *11*(6). https://doi.org/10.1038/s41408-021-00497-1

Dinardo, C. D., Ravandi, F., Agresta, S., Konopleva, M., Takahashi, K., Kadia, T., Routbort, M., Patel, K. P., Mark Brandt, Pierce, S., Garcia-Manero, G., Cortes, J., & Kantarjian, H.. (2015). Characteristics, clinical outcome, and prognostic significance of IDH mutations in AML. *American Journal of Hematology*, *90*(8), 732–736. https://doi.org/10.1002/ajh.24072

Mill, C. P., Fiskus, W., DiNardo, C. D., Birdwell, C., Davis, J. A., Kadia, T. M., Takahashi, K., Short, N., Daver, N., Ohanian, M., Borthakur, G., Kornblau, S. M., Green, M. R., Qi, Y., Su, X., Khoury, J. D., & Bhalla, K. N. (2022). Effective therapy for AML with RUNX1 mutation by cotreatment with inhibitors of protein translation and BCL2. *Blood, 139*(6), 907–921. https://doi.org/10.1182/blood.2021013156

Simon, L., Spinella, J.-F., Yao, C.-Y., Lavallée, V.-P., Boivin, I., Boucher, G., Audemard, É., Bordeleau, M.-E., Lemieux, S., Hébert, J., & Sauvageau, G. (2020). High frequency of germline RUNX1 mutations in patients with RUNX1-mutated AML. *Blood, 135*(21), 1882–1886. https://doi.org/10.1182/blood.2019003357

Fasan, A., Haferlach, C., Alpermann, T., & et al. (2014). The role of different genetic subtypes of CEBPA-mutated AML. *Leukemia, 28*(4), 794–803. https://doi.org/10.1038/leu.2013.273

Konstandin, N. P., Pastore, F., Herold, T., Dufour, A., Rothenberg-Thurley, M., Hinrichsen, T., Ksienzyk, B., Tschuri, S., Schneider, S., Hoster, E., Berdel, W. E., Woermann, B. J., Sauerland, M. C., Braess, J., Bohlander, S. K., Klein, H.-G., Hiddemann, W., Metzeler, K. H., & Spiekermann, K. (2018). Genetic heterogeneity of cytogenetically normal AML with mutations of CEBPA. Blood Advances, 2(20), 2724–2731. https://doi.org/10.1182/bloodadvances.2018016840

Taube, F., Georgi, J. A., Kramer, M., Stasik, S., Middeke, J. M., Röllig, C., Krug, U., Krämer, A., Scholl, S., Hochhaus, A., Brümmendorf, T. H., Naumann, R., Petzold, A., Mulet-Lazaro, R., Valk, P. J. M., Steffen, B., Einsele, H., Schaich, M., Burchert, A., … Thiede, C. (2022). CEBPA mutations in 4708 patients with acute myeloid leukemia: differential impact of bZIP and TAD mutations on outcome. *Blood Journal*, *139*(1), 87–103. https://doi.org/10.1182/blood.2020009680

Grob, T., Al Hinai, A. S. A., Sanders, M. A., Kavelaars, F. G., Rijken, M., Gradowska, P. L., Biemond, B. J., Breems, D. A., Maertens, J., Van Marwijk Kooy, M., Pabst, T., De Weerdt, O., Ossenkoppele, G. J., Van De Loosdrecht, A. A., Huls, G. A., Cornelissen, J. J., Beverloo, H. B., Löwenberg, B., Jongen-Lavrencic, M., & Valk, P. J. M.. (2022). Molecular characterization of mutant TP53 acute myeloid leukemia and high-risk

myelodysplastic syndrome. *Blood Journal*, *139*(15), 2347–2354. https://doi.org/10.1182/blood.2021014472

Yu, J., Li, Y., Zhang, D., Wan, D., & Jiang, Z.. (2020). Clinical implications of recurrent gene mutations in acute myeloid leukemia. *Experimental Hematology & Oncology*, *9*(1). https://doi.org/10.1186/s40164-020-00161-7

Rowe, J. M.. (2022). The "7+3" regimen in acute myeloid leukemia. *Haematologica*, *107*(1), 3–3. https://doi.org/10.3324/haematol.2021.280161

Bakhtiar, S., Salzmann-Manrique, E., Hutter, M., & others. (2019). AlloHSCT in paediatric ALL and AML in complete remission: Improvement over time impacted by accreditation? *Bone Marrow Transplantation,* *54*(5), 737–745. https://doi.org/10.1038/s41409-018-0341-z

Ochs, M. A., Marini, B. L., Perissinotti, A. J., Foucar, C. E., Pettit, K., Burke, P., Bixby, D. L., & Benitez, L. L.. (2022). Oncology stewardship in acute myeloid leukemia. *Annals of Hematology*, *101*(8), 1627–1644. https://doi.org/10.1007/s00277-022-04872-1

Ochs, M. A., Marini, B. L., Perissinotti, A. J., Foucar, C. E., Pettit, K., Burke, P., Bixby, D. L., & Benitez, L. L. (2022). Oncology stewardship in acute myeloid leukemia. *Annals of Hematology*, *101*(8), 1627–1644. https://doi.org/10.1007/s00277-022-04872-1

Daver, N., Schlenk, R. F., Russell, N. H., & Levis, M. J.. (2019). Targeting FLT3 mutations in AML: review of current knowledge and evidence. *Leukemia*, *33*(2), 299–312. https://doi.org/10.1038/s41375-018-0357-9

Antar, A. I., Otrock, Z. K., Jabbour, E., & others. (2020). FLT3 inhibitors in acute myeloid leukemia: Ten frequently asked questions. *Leukemia,* *34*(3), 682–696. https://doi.org/10.1038/s41375-019-0694-3

Mcmurry, H., Fletcher, L., & Traer, E.. (2021). IDH Inhibitors in AML—Promise and Pitfalls. *Current Hematologic Malignancy Reports*, *16*(2), 207–217. https://doi.org/10.1007/s11899-021-00619-3

Issa, G. C., & Dinardo, C. D.. (2021). Acute myeloid leukemia with IDH1 and IDH2 mutations: 2021 treatment algorithm. *Blood Cancer Journal*, *11*(6). https://doi.org/10.1038/s41408-021-00497-1

Fruchtman, H., Avigan, Z. M., Waksal, J. A., Brennan, N., & Mascarenhas, J. O.. (2024). Management of isocitrate dehydrogenase 1/2 mutated acute myeloid leukemia. *Leukemia*, *38*(5), 927–935. https://doi.org/10.1038/s41375-024-02246-2

Konopleva, M., Pollyea, D., Potluri, J., Chyla, B., Hogdal, L., Busman, T., McKeegan, E., Salem, A., Zhu, M., Ricker, J., Blum, W., DiNardo, C., Kadia, T., Dunbar, M., Kirby, R., Falotico, N., Leverson, J., Humerickhouse, R., Mabry, M., & Letai, A. (2016). Efficacy and biological correlates of response in a phase II study of Venetoclax monotherapy in patients with acute myelogenous leukemia. *Cancer Discovery,* *6*(6), 1106–1117. https://doi.org/10.1158/2159-8290.CD-16-0313

Konopleva, M., & Letai, A.. (2018). BCL-2 inhibition in AML: an unexpected bonus?. *Blood Journal*, *132*(10), 1007–1012. https://doi.org/10.1182/blood-2018-03-828269

Nwosu, G. O., Ross, D. M., Powell, J. A., & others. (2024). Venetoclax therapy and

emerging resistance mechanisms in acute myeloid leukaemia. *Cell Death & Disease, 15*(413). https://doi.org/10.1038/s41419-024-06810-7

Molica, M., Perrone, S., Mazzone, C., Niscola, P., Cesini, L., Abruzzese, E., & De Fabritiis, P.. (2021). CD33 Expression and Gentuzumab Ozogamicin in Acute Myeloid Leukemia: Two Sides of the Same Coin. *Cancers*, *13*(13), 3214. https://doi.org/10.3390/cancers13133214

Liu, J., Tong, J., & Yang, H.. (2022). Targeting CD33 for acute myeloid leukemia therapy. *BMC Cancer*, *22*(1). https://doi.org/10.1186/s12885-021-09116-5

Swaminathan, M., & Cortes, J. E. (2023). Update on the role of gemtuzumab-ozogamicin in the treatment of acute myeloid leukemia. Therapeutic Advances in Hematology, 14. https://doi.org/10.1177/20406207231154708

Jamieson, C., Martinelli, G., Papayannidis, C., & Cortes, J. E. (2020). Hedgehog pathway inhibitors: A new therapeutic class for the treatment of acute myeloid leukemia. *Blood Cancer Discovery, 1*(2), 134–145. https://doi.org/10.1158/2643-3230.BCD-20-0007

Tettamanti, S., Pievani, A., Biondi, A., & Introna, M. (2022). Catch me if you can: How AML and its niche escape immunotherapy. *Leukemia, 36*(1), 13–22. https://doi.org/10.1038/s41375-021-01350-x

Levine, B.. (2007). Autophagy and cancer. *Nature*, *446*(7137), 745–747. https://doi.org/10.1038/446745a

Levine, B., & Kroemer, G. (2008). Autophagy in the pathogenesis of disease. *Cell*, *132*(1), 27–42. https://doi.org/10.1016/j.cell.2007.12.018

Levine, B., & Kroemer, G. (2019). Biological Functions of Autophagy Genes: A Disease Perspective. *Cell*, *176*(1-2), 11–42. https://doi.org/10.1016/j.cell.2018.09.048

Kuma, A., Hatano, M., Matsui, M., Yamamoto, A., Nakaya, H., Yoshimori, T., Ohsumi, Y., Tokuhisa, T., & Mizushima, N. (2004). The role of autophagy during the early neonatal starvation period. *Nature*, *432*(7020), 1032–1036. https://doi.org/10.1038/nature03029

Park, H., Kang, J. -H., & Lee, S. (2020). Autophagy in Neurodegenerative Diseases: A Hunter for Aggregates. *International Journal of Molecular Sciences*, *21*(9), 3369. https://doi.org/10.3390/ijms21093369

Qian, H., Chao, X., Williams, J., Fulte, S., Li, T., Yang, L., & Ding, W.-X. (2021). Autophagy in liver diseases: A review. *Molecular Aspects of Medicine, 82,* 100973. https://doi.org/10.1016/j.mam.2021.100973

Wu, X., Liu, Z., Yu, X.-Y., Xu, S., & Luo, J. (2020). Autophagy and cardiac diseases: Therapeutic potential of natural products. *Medicinal Research Reviews.* https://doi.org/10.1002/med.21733

Choi, K. (2012). Autophagy and cancer. *Experimental & Molecular Medicine, 44*(2), 109–120. https://doi.org/10.3858/emm.2012.44.2.033

Jung, S., Jeong, H., & Yu, S.-W.. (2020). Autophagy as a decisive process for cell death. *Experimental & Molecular Medicine*, *52*(6), 921–930. https://doi.org/10.1038/s12276-020-0455-4

Noguchi, M., Hirata, N., Tanaka, T., Suizu, F., Nakajima, H., & Chiorini, J. A.. (2020). Autophagy as a modulator of cell death machinery. *Cell Death & Disease*, *11*(7).

https://doi.org/10.1038/s41419-020-2724-5

Liu, Y., Shoji-Kawata, S., Sumpter, R. M., Wei, Y., Ginet, V., Zhang, L., Posner, B., Tran, K. A., Green, D. R., Xavier, R. J., Shaw, S. Y., Clarke, P. G. H., Puyal, J., & Levine, B.. (2013). Autosis is a Na + ,K + -ATPase–regulated form of cell death triggered by autophagy-inducing peptides, starvation, and hypoxia–ischemia.*Proceedings of the National Academy of Sciences*, *110*(51), 20364–20371. https://doi.org/10.1073/pnas.1319661110

Liu, Y., & Levine, B.. (2015). Autosis and autophagic cell death: the dark side of autophagy. *Cell Death & Differentiation*, *22*(3), 367–376. https://doi.org/10.1038/cdd.2014.143

Akimoto, M., Iizuka, M., Kanematsu, R., Yoshida, M., & Takenaga, K.. (2015). Anticancer Effect of Ginger Extract against Pancreatic Cancer Cells Mainly through Reactive Oxygen Species-Mediated Autotic Cell Death. PLOS ONE, 10(5), e0126605. https://doi.org/10.1371/journal.pone.0126605

Kondo, Y., Kanzawa, T., Sawaya, R., & Kondo, S. (2005). The role of autophagy in cancer development and response to therapy. *Nature reviews. Cancer*, *5*(9), 726–734. https://doi.org/10.1038/nrc1692

Hernandez, G. A., & Perera, R. M.. (2022). Autophagy in cancer cell remodeling and quality control. *Molecular Cell*, *82*(8), 1514–1527. https://doi.org/10.1016/j.molcel.2022.03.023

Lalaoui, N., Johnstone, R., & Ekert, P. G.. (2016). Autophagy and AML—food for thought. *Cell Death & Differentiation*, *23*(1), 5–6. https://doi.org/10.1038/cdd.2015.136

Chen, Y., Chen, J., Zou, Z., Xu, L., & Li, J.. (2024). Crosstalk between autophagy and metabolism: implications for cell survival in acute myeloid leukemia. *Cell Death Discovery*, *10*(1). https://doi.org/10.1038/s41420-024-01823-9

Du, W., Xu, A., Huang, Y., Cao, J., Zhu, H., Yang, B., Shao, X., He, Q., & Ying, M. (2021). The role of autophagy in targeted therapy for acute myeloid leukemia. *Autophagy, 17*(10), 2665–2679. https://doi.org/10.1080/15548627.2020.1822628

Seo, W., Silwal, P., Song, I.-C., & Jo, E.-K.. (2022). The dual role of autophagy in acute myeloid leukemia. *Journal of Hematology & Oncology*, *15*(1). https://doi.org/10.1186/s13045-022-01262-y

Kocaturk, N. M., Akkoc, Y., Kig, C., Bayraktar, O., Gozuacik, D., & Kutlu, O. (2019). Autophagy as a molecular target for cancer treatment. *European Journal of Pharmaceutical Sciences, 134*, 116–137. https://doi.org/10.1016/j.ejps.2019.04.011

Galluzzi, L., Bravo-San Pedro, J. M., Levine, B., Green, D. R., & Kroemer, G.. (2017). Pharmacological modulation of autophagy: therapeutic potential and persisting obstacles. *Nature Reviews Drug Discovery*, *16*(7), 487–511. https://doi.org/10.1038/nrd.2017.22

Mulcahy Levy, J. M., & Thorburn, A.. (2020). Autophagy in cancer: moving from understanding mechanism to improving therapy responses in patients. *Cell Death & Differentiation*, *27*(3), 843–857. https://doi.org/10.1038/s41418-019-0474-7

Mauthe, M., Orhon, I., Rocchi, C., Zhou, X., Luhr, M., Hijlkema, K. J., Coppes, R. P., Engedal, N., Mari, M., & Reggiori, F. (2018). Chloroquine inhibits autophagic flux

by decreasing autophagosome-lysosome fusion. *Autophagy*, *14*(8), 1435–1455. https://doi.org/10.1080/15548627.2018.1474314

Blagosklonny M. V. (2023). Cancer prevention with rapamycin. *Oncotarget*, *14*, 342–350. https://doi.org/10.18632/oncotarget.28410

Yun, C. W., Jeon, J., Go, G., Lee, J. H., & Lee, S. H. (2021). The Dual Role of Autophagy in Cancer Development and a Therapeutic Strategy for Cancer by Targeting Autophagy. *International Journal of Molecular Sciences*, *22*(1), 179. https://doi.org/10.3390/ijms22010179

Magné, J., & Green, D. R. (2022). LC3-associated endocytosis and the functions of Rubicon and ATG16L1. Science advances, 8(43), eabo5600. https://doi.org/10.1126/sciadv.abo5600

Jiang, G. M., Tan, Y., Wang, H., Peng, L., Chen, H. T., Meng, X. J., Li, L. L., Liu, Y., Li, W. F., & Shan, H. (2019). The relationship between autophagy and the immune system and its applications for tumor immunotherapy. Molecular cancer, 18(1), 17. https://doi.org/10.1186/s12943-019-0944-z

Xia, F., Deng, C., Jiang, Y., Qu, Y., Deng, J., Cai, Z., Ding, Y., Guo, Z., & Wang, J. (2018). IL4 (interleukin 4) induces autophagy in B cells leading to exacerbated asthma. Autophagy, 14(3), 450–464. https://doi.org/10.1080/15548627.2017.1421884

Botbol, Y., Guerrero-Ros, I., & Macian, F. (2016). Key roles of autophagy in regulating T-cell function. European journal of immunology, 46(6), 1326–1334. https://doi.org/10.1002/eji.201545955

Michaud, M., Martins, I., Sukkurwala, A. Q., Adjemian, S., Ma, Y., Pellegatti, P., Shen, S., Kepp, O., Scoazec, M., Mignot, G., Rello-Varona, S., Tailler, M., Menger, L., Vacchelli, E., Galluzzi, L., Ghiringhelli, F., di Virgilio, F., Zitvogel, L., & Kroemer, G. (2011). Autophagy-dependent anticancer immune responses induced by chemotherapeutic agents in mice. Science (New York, N.Y.), 334(6062), 1573–1577. https://doi.org/10.1126/science.1208347

Pietrocola, F., Pol, J., Vacchelli, E., Rao, S., Enot, D. P., Baracco, E. E., Levesque, S., Castoldi, F., Jacquelot, N., Yamazaki, T., Senovilla, L., Marino, G., Aranda, F., Durand, S., Sica, V., Chery, A., Lachkar, S., Sigl, V., Bloy, N., Buque, A., Kroemer, G. (2016). Caloric Restriction Mimetics Enhance Anticancer Immunosurveillance. Cancer cell, 30(1), 147–160. https://doi.org/10.1016/j.ccell.2016.05.016

Peng, S., Gao, J., Stojkov, D., Yousefi, S., & Simon, H. U. (2023). Established and emerging roles for mitochondria in neutrophils. *Immunological reviews*, *314*(1), 413–426. https://doi.org/10.1111/imr.13158

Zorova, L. D., Popkov, V. A., Plotnikov, E. Y., Silachev, D. N., Pevzner, I. B., Jankauskas, S. S., Babenko, V. A., Zorov, S. D., Balakireva, A. V., Juhaszova, M., Sollott, S. J., & Zorov, D. B. (2018). Mitochondrial membrane potential. *Analytical biochemistry*, *552*, 50–59. https://doi.org/10.1016/j.ab.2017.07.009

Bertram, R., Pedersen, M. G., Luciani, D. S., & Sherman, A. (2006). A simplified model for mitochondrial ATP production. *Journal of Theoretical Biology, 243*(4), 575–586. https://doi.org/10.1016/j.jtbi.2006.07.019

Martínez-Reyes, I., & Chandel, N. S.. (2020). Mitochondrial TCA cycle metabolites control physiology and disease. *Nature Communications*, *11*(1).

https://doi.org/10.1038/s41467-019-13668-3

Zorov, D. B., Juhaszova, M., & Sollott, S. J. (2014). Mitochondrial reactive oxygen species (ROS) and ROS-induced ROS release. *Physiological reviews*, *94*(3), 909–950. https://doi.org/10.1152/physrev.00026.2013

Palma, F. R., Gantner, B. N., Sakiyama, M. J., Kayzuka, C., Shukla, S., Lacchini, R., Cunniff, B., & Bonini, M. G. (2024). ROS production by mitochondria: function or dysfunction?. *Oncogene*, *43*(5), 295–303. https://doi.org/10.1038/s41388-023-02907-z

Flores-Romero, H., Dadsena, S., & García-Sáez, A. J.. (2023). Mitochondrial pores at the crossroad between cell death and inflammatory signaling. *Molecular Cell*, *83*(6), 843–856. https://doi.org/10.1016/j.molcel.2023.02.021

Bonora, M., Giorgi, C., & Pinton, P. (2022). Molecular mechanisms and consequences of mitochondrial permeability transition. *Nature reviews. Molecular cell biology*, *23*(4), 266–285. https://doi.org/10.1038/s41580-021-00433-y

Baines, C. P., Kaiser, R. A., Sheiko, T., Craigen, W. J., & Molkentin, J. D. (2007). Voltage-dependent anion channels are dispensable for mitochondrial-dependent cell death. *Nature cell biology*, *9*(5), 550–555. https://doi.org/10.1038/ncb1575

Kokoszka, J. E., Waymire, K. G., Levy, S. E., Sligh, J. E., Cai, J., Jones, D. P., MacGregor, G. R., & Wallace, D. C. (2004). The ADP/ATP translocator is not essential for the mitochondrial permeability transition pore. *Nature*, *427*(6973), 461–465. https://doi.org/10.1038/nature02229

Rizzuto, R., De Stefani, D., Raffaello, A., & Mammucari, C. (2012). Mitochondria as sensors and regulators of calcium signalling. *Nature reviews. Molecular cell biology*, *13*(9), 566–578. https://doi.org/10.1038/nrm3412

Giorgi, C., Marchi, S., & Pinton, P. (2018). The machineries, regulation and cellular functions of mitochondrial calcium. *Nature reviews. Molecular cell biology*, *19*(11), 713–730. https://doi.org/10.1038/s41580-018-0052-8

Adebayo, M., Singh, S., Singh, A. P., & Dasgupta, S. (2021). Mitochondrial fusion and fission: The fine-tune balance for cellular homeostasis. *FASEB journal : official publication of the Federation of American Societies for Experimental Biology*, *35*(6), e21620. https://doi.org/10.1096/fj.202100067R

Peng, M., Huang, Y., Zhang, L., Zhao, X., & Hou, Y. (2022). Targeting Mitochondrial Oxidative Phosphorylation Eradicates Acute Myeloid Leukemic Stem Cells. *Frontiers in oncology*, *12*, 899502. https://doi.org/10.3389/fonc.2022.899502

Egan, G., & Schimmer, A. D. (2023). Contribution of metabolic abnormalities to acute myeloid leukemia pathogenesis. *Trends in cell biology*, *33*(6), 455–462. https://doi.org/10.1016/j.tcb.2022.11.004

Jayavelu, A. K., Wolf, S., Buettner, F., Alexe, G., Häupl, B., Comoglio, F., Schneider, C., Doebele, C., Fuhrmann, D. C., Wagner, S., Donato, E., Andresen, C., Wilke, A. C., Zindel, A., Jahn, D., Splettstoesser, B., Plessmann, U., Münch, S., Abou-El-Ardat, K., … Oellerich, T.. (2022). The proteogenomic subtypes of acute myeloid leukemia. *Cancer Cell*, *40*(3), 301–317.e12. https://doi.org/10.1016/j.ccell.2022.02.006

Porporato, P. E., Filigheddu, N., Pedro, J. M. B., Kroemer, G., & Galluzzi, L. (2018). Mitochondrial metabolism and cancer. *Cell research*, *28*(3), 265–280.

https://doi.org/10.1038/cr.2017.155

Thomas, G. E., Egan, G., García-Prat, L., Botham, A., Voisin, V., Patel, P. S., Hoff, F. W., Chin, J., Nachmias, B., Kaufmann, K. B., Khan, D. H., Hurren, R., Wang, X., Gronda, M., Maclean, N., O'Brien, C., Singh, R. P., Jones, C. L., Harding, S. M., … Schimmer, A. D.. (2022). The metabolic enzyme hexokinase 2 localizes to the nucleus in AML and normal haematopoietic stem and progenitor cells to maintain stemness. *Nature Cell Biology*, *24*(6), 872–884. https://doi.org/10.1038/s41556-022-00925-9

Panina, S. B., Baran, N., Brasil Da Costa, F. H., Konopleva, M., & Kirienko, N. V.. (2019). A mechanism for increased sensitivity of acute myeloid leukemia to mitotoxic drugs. *Cell Death & Disease*, *10*(8). https://doi.org/10.1038/s41419-019-1851-3

Griessinger, E., Moschoi, R., Biondani, G., & Peyron, J. F. (2017). Mitochondrial Transfer in the Leukemia Microenvironment. *Trends in cancer*, *3*(12), 828–839. https://doi.org/10.1016/j.trecan.2017.10.003

Panina, S. B., Pei, J., & Kirienko, N. V. (2021). Mitochondrial metabolism as a target for acute myeloid leukemia treatment. *Cancer & metabolism*, *9*(1), 17. https://doi.org/10.1186/s40170-021-00253-w

Firmanty, P., Chomczyk, M., Dash, S., Konopleva, M., & Baran, N.. (2024). Feasibility and Safety of Targeting Mitochondria Function and Metabolism in Acute Myeloid Leukemia. *Current Pharmacology Reports*, *10*(6), 388–404. https://doi.org/10.1007/s40495-024-00378-8

Funderburk, S. F., Wang, Q. J., & Yue, Z. (2010). The Beclin 1-VPS34 complex--at the crossroads of autophagy and beyond. *Trends in cell biology*, *20*(6), 355–362. https://doi.org/10.1016/j.tcb.2010.03.002

Lu, J., He, L., Behrends, C., Araki, M., Araki, K., Jun Wang, Q., Catanzaro, J. M., Friedman, S. L., Zong, W. X., Fiel, M. I., Li, M., & Yue, Z. (2014). NRBF2 regulates autophagy and prevents liver injury by modulating Atg14L-linked phosphatidylinositol-3 kinase III activity. *Nature communications*, *5*, 3920. https://doi.org/10.1038/ncomms4920

Levine, B., Liu, R., Dong, X., & Zhong, Q.. (2015). Beclin orthologs: integrative hubs of cell signaling, membrane trafficking, and physiology. *Trends in Cell Biology*, *25*(9), 533–544. https://doi.org/10.1016/j.tcb.2015.05.004

Wu, S., He, Y., Qiu, X., Yang, W., Liu, W., Li, X., Li, Y., Shen, H. M., Wang, R., Yue, Z., & Zhao, Y. (2018). Targeting the potent Beclin 1-UVRAG coiled-coil interaction with designed peptides enhances autophagy and endolysosomal trafficking. *Proceedings of the National Academy of Sciences of the United States of America*, *115*(25), E5669–E5678. https://doi.org/10.1073/pnas.1721173115

Lee, A. C.-L., Harris, J. L., Khanna, K. K., & Hong, J.-H.. (2019). A Comprehensive Review on Current Advances in Peptide Drug Development and Design. *International Journal of Molecular Sciences*, *20*(10), 2383. https://doi.org/10.3390/ijms20102383

Wang, L., Wang, N., Zhang, W., Cheng, X., Yan, Z., Shao, G., Wang, X., Wang, R., & Fu, C.. (2022). Therapeutic peptides: current applications and future directions. *Signal Transduction and Targeted Therapy*, *7*(1). https://doi.org/10.1038/s41392-022-00904-4

Kim, Y. W., Grossmann, T. N., & Verdine, G. L. (2011). Synthesis of all-hydrocarbon stapled α-helical peptides by ring-closing olefin metathesis. *Nature protocols*, *6*(6), 761–771. https://doi.org/10.1038/nprot.2011.324

Walensky, L. D., & Bird, G. H. (2014). Hydrocarbon-stapled peptides: principles, practice, and progress. *Journal of medicinal chemistry*, *57*(15), 6275–6288. https://doi.org/10.1021/jm4011675

Gump, J. M., & Dowdy, S. F. (2007). TAT transduction: the molecular mechanism and therapeutic prospects. *Trends in molecular medicine*, *13*(10), 443–448. https://doi.org/10.1016/j.molmed.2007.08.002

Zorko, M., & Langel, Ü. (2022). Cell-Penetrating Peptides. *Methods in molecular biology (Clifton, N.J.)*, *2383*, 3–32. https://doi.org/10.1007/978-1-0716-1752-6_1

Koren, E., & Torchilin, V. P. (2012). Cell-penetrating peptides: breaking through to the other side. *Trends in molecular medicine*, *18*(7), 385–393. https://doi.org/10.1016/j.molmed.2012.04.012

Gori, A., Lodigiani, G., Colombarolli, S. G., Bergamaschi, G., & Vitali, A. (2023). Cell Penetrating Peptides: Classification, Mechanisms, Methods of Study, and Applications. *ChemMedChem*, *18*(17),e202300236.https://doi.org/10.1002/cmdc.202300236

Yang, Q., Qiu, X., Zhang, X., Yu, Y., Li, N., Wei, X., Feng, G., Li, Y., Zhao, Y., & Wang, R. (2021). Optimization of Beclin 1-Targeting Stapled Peptides by Staple Scanning Leads to Enhanced Antiproliferative Potency in Cancer Cells. *Journal of medicinal chemistry*, *64*(18), 13475–13486. https://doi.org/10.1021/acs.jmedchem.1c00870

Ye, F., Zhang, W., Fan, C., Dong, J., Peng, M., Deng, W., Zhang, H., & Yang, L. (2023). Antileukemic effect of Venetoclax and hypomethylating agents via caspase-3/GSDME-mediated pyroptosis. Journal of translational medicine, 21(1), 606. https://doi.org/10.1186/s12967-023-04481-0

Giorgi, C., Danese, A., Missiroli, S., Patergnani, S., & Pinton, P. (2018). Calcium Dynamics as a Machine for Decoding Signals. Trends in cell biology, 28(4), 258–273. https://doi.org/10.1016/j.tcb.2018.01.002

Arimoto, K. I., Miyauchi, S., Liu, M., & Zhang, D. E. (2024). Emerging role of immunogenic cell death in cancer immunotherapy. Frontiers in immunology, 15, 1390263. https://doi.org/10.3389/fimmu.2024.1390263

Wherry, E. J., & Kurachi, M. (2015). Molecular and cellular insights into T cell exhaustion. Nature reviews. Immunology, 15(8), 486–499. https://doi.org/10.1038/nri3862

Ruzicka, M., Koenig, L. M., Formisano, S., Boehmer, D. F. R., Vick, B., Heuer, E. M., Meinl, H., Kocheise, L., Zeitlhöfler, M., Ahlfeld, J., Kobold, S., Endres, S., Subklewe, M., Duewell, P., Schnurr, M., Jeremias, I., Lichtenegger, F. S., & Rothenfusser, S. (2020). RIG-I-based immunotherapy enhances survival in preclinical AML models and sensitizes AML cells to checkpoint blockade. Leukemia, 34(4), 1017–1026. https://doi.org/10.1038/s41375-019-0639-x

Chen, D. W., Fan, J. M., Schrey, J. M., Mitchell, D. V., Jung, S. K., Hurwitz, S. N., Perez, E. B., Muraro, M. J., Carroll, M., Taylor, D. M., & Kurre, P. (2024).

Inflammatory recruitment of healthy hematopoietic stem and progenitor cells in the acute myeloid leukemia niche. *Leukemia*, *38*(4), 741–750. https://doi.org/10.1038/s41375-024-02136-7

Sundrud, M. S., Torres, V. J., Unutmaz, D., & Cover, T. L. (2004). Inhibition of primary human T cell proliferation by Helicobacter pylori vacuolating toxin (VacA) is independent of VacA effects on IL-2 secretion. Proceedings of the National Academy of Sciences of the United States of America, 101(20), 7727–7732. https://doi.org/10.1073/pnas.0401528101

Hall, J. E. (2011). The cell and general physiology. In Guyton and Hall textbook of medical physiology (12th ed., pp. 286–287). Saunders/Elsevier.

Hall, C., Lueshen, E., Mošat', A., & Linninger, A. A. (2012). Interspecies scaling in pharmacokinetics: a novel whole-body physiologically based modeling framework to discover drug biodistribution mechanisms in vivo. Journal of pharmaceutical sciences, 101(3), 1221–1241. https://doi.org/10.1002/jps.22811